

PROGRADE ANOMALOUS ORBITS IN TRIAXIAL GRAVITATIONAL  
POTENTIALS THAT ROTATE ABOUT THE LONG AXIS: VLA NEUTRAL  
HYDROGEN OBSERVATIONS AND MODELING OF THE INCLINED  
RINGS AROUND THE GALAXIES NGC 2685 AND NGC 660

BY

MARY ELAINE MAHON

A DISSERTATION PRESENTED TO THE GRADUATE SCHOOL  
OF THE UNIVERSITY OF FLORIDA IN PARTIAL FULFILLMENT  
OF THE REQUIREMENTS FOR THE DEGREE OF  
DOCTOR OF PHILOSOPHY

UNIVERSITY OF FLORIDA

1992

To my father, Arthur Forrest Camp, Jr. and my husband, John K. Mahon, III

## ACKNOWLEDGMENTS

I am deeply indebted to my mentor, George Contopoulos, who introduced me to the subject of galactic dynamics. He is, and has always been, generous with his time, open to questions, and insightful in his guidance. I would also like to express my gratitude to Henry Kandrup for providing me with intellectual stimulation, as well as academic, financial, and emotional support over this past year. My sincere appreciation is also extended to Steve Gottesman, who introduced me to the wonders of radio astronomy and who supported me for a number of years as a research assistant. My deepest thanks go to Jim Hunter who came through for me when I needed it most.

A very special thanks is owed to Pat Palmer, Jacqueline van Gorkom, Dave Westpfahl for generously giving of their time to assist, instruct, and encourage a fledgling radio astronomer.

This dissertation would never have been possible had it not been for the efforts of Charlie Taylor, who worked tirelessly to produce an optimal computing environment in the Astronomy Department. He patiently taught me everything I needed to know to make the best of it. I also am indebted to him for coming in on his own time during the last weekend before first submission deadline, to bring up the system, so that this dissertation could be submitted on time.

I cannot begin to express the thanks I owe to my parents, Mary and Forrest Camp, who have been a continuous source of love and encouragement throughout my life, especially my dad, who always seemed to know just when to touch base with me.

Above all, my deepest gratitude is to my husband, John, who has been there from the moment I first realized I wanted to be an astronomer through these final days as a graduate student. He has never wavered. For this I do, and shall always love him.

## TABLE OF CONTENTS

ACKNOWLEDGMENTS . . . . .	iii
LIST OF TABLES . . . . .	vii
LIST OF FIGURES . . . . .	viii
ABSTRACT . . . . .	xxii
CHAPTERS	
1 INTRODUCTION . . . . .	1
2 ORBITS IN ROTATING TRIAXIAL POTENTIALS . . . . .	14
Review of Previous Work on Orbits in Triaxial Potentials . . . . .	14
Stationary Triaxial Potentials . . . . .	14
Orbits in Rotating Triaxial Potentials . . . . .	15
Rotation about the short axis of the potential . . . . .	15
Rotation about the long axis of the potential . . . . .	18
Calculation of Orbits and their Stability . . . . .	20
Orbits about the Long, Rotation Axis of the Potential . . . . .	25
A Mildly Triaxial, Logarithmic Potential . . . . .	26
The bifurcation sequence as a function of $\Omega$ . . . . .	26
Properties of Orbits in the Families $E_p$ , $E_{p-a}$ , and SAO . . . . .	36
A Nearly Prolate, Triaxial Logarithmic Potential . . . . .	45
Discussion . . . . .	47
3 HI OBSERVATIONS WITH THE VLA RADIO TELESCOPE . . . . .	50
Review of Aperture Synthesis with the VLA . . . . .	50
Mapping of VLA Data . . . . .	55
NGC 2685 and its Dwarf Companion, MCG+10-13-030 . . . . .	58
Literature Review on the Galaxy NGC 2685 . . . . .	58
VLA HI Observations . . . . .	63
The observing runs for NGC 2685 . . . . .	63

Calibration and editing of the visibilities . . . . .	65
Distribution of HI in NGC 2685 and MCG+10-13-030 . . . . .	66
NGC 660 and its Dwarf Companion, UGC 1195 . . . . .	104
Review of Published Observations of NGC 660 . . . . .	104
VLA HI Observations . . . . .	108
The observing runs for NGC 660 . . . . .	108
Calibration and editing of the visibilities . . . . .	110
Distribution of HI in NGC 660 and UGC 1195 . . . . .	111
<b>4 MODELS . . . . .</b>	<b>133</b>
Construction of Model Density and Velocity Fields . . . . .	133
Projection of the Model onto the Plane of the Sky . . . . .	137
Weighting the Orbits with the Integrated-Intensity of HI . . . . .	139
Moments of the Model Radiation Field . . . . .	141
Models of NGC 660 and NGC 2685 . . . . .	143
General Considerations . . . . .	143
Models of NGC 2685 . . . . .	145
Models of NGC 660 . . . . .	155
<b>5 CONCLUSION . . . . .</b>	<b>167</b>
<b>BIBLIOGRAPHY . . . . .</b>	<b>174</b>
<b>BIOGRAPHICAL SKETCH . . . . .</b>	<b>181</b>

## LIST OF TABLES

Table 3.1:	Optical characteristics of the galaxy NGC 2685. . . . .	62
Table 3.2:	VLA observing parameters for NGC 2685. . . . .	64
Table 3.3:	HI map parameters for NGC 2685. . . . .	67
Table 3.4:	Noise statistics on HI channel maps of NGC 2685. . . . .	68
Table 3.5:	Continuum sources in the NGC 2685 maps. . . . .	69
Table 3.6:	Dwarf galaxies near NGC 2685. . . . .	90
Table 3.7:	HI characteristics of NGC 2685. . . . .	100
Table 3.8:	HI characteristics of MCG+10–13–030. . . . .	101
Table 3.9:	Optical characteristics of NGC 660 and UGC 1195. . . . .	107
Table 3.10:	VLA observing parameters for NGC 660. . . . .	109
Table 3.11:	UV clip parameters. . . . .	111
Table 3.12:	VLA, HI map parameters for NGC 660. . . . .	112
Table 3.13:	Noise statistics on VLA, HI channel maps of NGC 660. . . . .	113
Table 3.14:	Continuum sources in the VLA maps of NGC 660. . . . .	116
Table 3.15:	HI characteristics of NGC 660. . . . .	131
Table 3.16:	HI characteristics of UGC 1195 . . . . .	132
Table 4.1:	Coefficients and errors for the polynomial weighting function $w(f(H'))$ shown in Figure 4.9, where $H' = H/H_{min}$ . . . . .	154
Table 4.2:	Coefficients and errors for the polynomial weighting function $w(f(H'))$ of Figure 4.13, where $H' = H/H_{min}$ . . . . .	160

## LIST OF FIGURES

Figure 2.4: Stability curves for orbits in a potential with shape parameters  $(q_a, q_b, q_c) = (0.95, 0.92, 1.00)$  and  $\Omega = 13.3 \text{ km s}^{-1} \text{ kpc}^{-1}$ . The SAOs bifurcate from the z-axis family at its transition from S→U at (I). As  $H$  increases, the SAOs go from S→C. These orbits terminate at (II) where the stability parameters of  $E_p\text{-}a$  and  $E_p\text{-}c$  collide on the  $b = -2$  axis. SAO-b bifurcates as D at the transition of the  $E_p\text{-}c$  family from D→U (IV). Following its bifurcation, SAO-b goes from D→C→S before terminating at the transition of the z-axis family from U→S (VI). The  $b_2$  stability parameters for the  $E_p\text{-}a$  and  $E_p\text{-}c$  families are joined on the  $b = -2$  axis at (V). . . . . 32

Figure 2.5: Stability curves for orbits in a potential with shape parameters  $(q_a, q_b, q_c) = (0.95, 0.92, 1.00)$  and  $\Omega = 13.6 \text{ km s}^{-1} \text{ kpc}^{-1}$ . The SAOs bifurcate from the z-axis family at its transition from S→U at (I). As  $H$  increases, the SAOs go from S→C→D before terminating at the transition of the  $E_p\text{-}c$  family from U→D at (III). SAO-b bifurcates as D at the transition of  $E_p\text{-}c$  from D→U (IV). From (IV), the SAO-b family goes from D→C→S before terminating at the transition of the z-axis family from U→S (VI). The  $b_2$  curves for the  $E_p\text{-}a$  and  $E_p\text{-}c$  families are joined on the  $b = -2$  axis at (II) and (V). . . . . 33

Figure 2.6: Stability curves for orbits in a potential with shape parameters  $(q_a, q_b, q_c) = (0.95, 0.92, 1.00)$  and  $\Omega = 13.79 \text{ km s}^{-1} \text{ kpc}^{-1}$ . At  $\Omega = \Omega_{c2} \simeq 13.79 \text{ km s}^{-1} \text{ kpc}^{-1}$  a collision of bifurcations occurs on the  $b = -2$  axis at the point where the  $b_1$  stability curve for the  $E_p\text{-}c$  family becomes tangent to the axis. At this point, the SAO and SAO-b families can be seen as bifurcating to the left and right, respectively. Above this value of  $\Omega$ , the SAO and SAO-b families join as one family of orbits. 34

Figure 2.7: Stability curves for orbits in a potential with  $(q_a, q_b, q_c) = (0.95, 0.92, 1.00)$  and  $\Omega = 14.0 \text{ km s}^{-1} \text{ kpc}^{-1}$ . SAO and SAO-b now form one family. From (I), as  $H$  increases, the SAOs go from S→C and these orbits, which were tilting down towards the equatorial plane for increasing  $H$ , tilt back up, away from the equatorial plane before going from C→S. SAO-b terminates at the transition of the z-axis family from U→S (VI). The  $b_2$  curves for  $E_p\text{-}a$  and  $E_p\text{-}c$  join on the  $b = -2$  axis at (II) and (V). . . . . 35

Figure 2.8: Stability curves, as a function of  $\Omega$ , for the  $E_p$ ,  $E_p-a$ , and SAO families, in a potential with  $(q_a, q_b, q_c) = (0.95, 0.92, 1.00)$  and  $H = 30,000$ . The  $b_2$  curve for the  $E_p-a$  family crosses the  $b = -2$  axis at (III-a) and (III). The  $E_p-a$  family terminates for higher  $\Omega$  at (V). Note that, for this value of  $H$ , the family  $E_p$  goes from U $\rightarrow$ S near  $\Omega = 11.3 \text{ km s}^{-1} \text{ kpc}^{-1}$ . . . . . 37

Figure 2.9: Stability curves for SAO and  $E_p-a$  families in a potential with  $(q_a, q_b, q_c) = (0.95, 0.92, 1.00)$  and  $\Omega = 2.6$ . SAO bifurcates from  $E_p$  at (I). For increasing  $H$ , SAO goes from S $\rightarrow$ C $\rightarrow$ S, terminating in the equatorial plane at (III).  $E_p-a$  goes from S $\rightarrow$ U at (III-a) and from U $\rightarrow$ S at (III), continuing for higher values of  $H$  as S. . . . . . 39

Figure 2.10: Stability curves giving  $b_{1,2}$  versus  $x_0$  for the SAO and  $E_p-a$  families in a potential with  $(q_a, q_b, q_c) = (0.95, 0.92, 1.00)$  and  $\Omega = 2.6$ , showing where the orbits cross the intermediate axis (x-axis) of the potential. SAO bifurcates as S on the left at (I) and terminates at (III) upon the transition of  $E_p-a$  from U $\rightarrow$ S.  $E_p-a$  is U between the points marked (III-a) and (III).  $E_p-a$  terminates at (V) for  $H = 80,702$ . . . . . . 41

Figure 2.11: Stability diagram for a potential with  $(q_a, q_b, q_c) = (0.95, 0.92, 1.00)$  and  $\Omega = 11.0$ . Following their bifurcation from the z-axis family at (I), the SAOs go from S $\rightarrow$ C $\rightarrow$ S, terminating at (III) upon the transition of  $E_p-a$  from U $\rightarrow$ S.  $E_p-a$  exists as S over a limited range in  $H$  between (II) and (V). SAO-b arises by bifurcation as D and, to the right goes from D $\rightarrow$ C $\rightarrow$ S before terminating at the transition of the z-axis family from U $\rightarrow$ S at (VI). . . . . . 43

Figure 2.12: Stability curves giving  $b_{1,2}$  versus  $x_0$  for a potential with  $(q_a, q_b, q_c) = (0.95, 0.92, 1.00)$  and  $\Omega = 11.0$ . Following bifurcation from the z-axis family at (I) for low values of  $H$ , the SAOs go from S $\rightarrow$ C $\rightarrow$ S, terminating at (III) upon the transition of  $E_p-a$  from U $\rightarrow$ S.  $E_p-a$  exists as S over a limited range in  $x_0$  between (II) and (V). SAO-b arises as D by bifurcation at the transition of the family  $E_p-c$  from D $\rightarrow$ U (not shown). For increasing  $H$  and decreasing  $x_0$ , SAO-b goes from D $\rightarrow$ C $\rightarrow$ S before terminating on the z-axis at the transition of the z-axis family from U $\rightarrow$ S at (VI). Though not shown, the family  $E_p$  becomes stable at  $x_0 = 3.16 \text{ kpc}$  and continues to the right, for higher  $H$  and  $x_0$  as S. . . . . . 44



Figure 3.3: Uniformly weighted, clean channel maps showing the distribution of HI in NGC 2685. The mean line of sight, heliocentric velocity for each map is printed at the top. Contour levels are multiples of the approximate r.m.s noise of 0.56 mJy/Beam:  $\sigma \times (-5, -3, 3, 5, 7)$ . The spatial resolution of the maps is  $11''.46 \times 9''.99$  and the beam position angle is  $52^\circ.33$ . Channel separations are  $20.73 \text{ km s}^{-1}$ . The pointing center for the observations,  $(\alpha, \delta)_{1950} = (08^\text{h} 51^\text{m} 41^\text{s}.2, 58^\circ 55' 30'')$ , is marked with a large “+”, while positions of stars in the optical image are marked with the smaller “+” signs. Minor tick marks are at 15 arcsecond intervals and major tick marks are labeled every two arcminutes from pointing center. North is at the top and West is to the right. . . . . 79

Figure 3.3: -- continued . . . . . 80

Figure 3.3: -- continued . . . . . 81

Figure 3.3: -- continued . . . . . 82

Figure 3.4: High resolution axis-velocity profile along the major axis of the outer HI ring of NGC 2685 at P.A. =  $35^\circ$ , derived from the smoothed uniformly weighted map cube. The spatial resolution is  $14''.00 \times 14''.00$  and the velocity resolution is  $24.876 \text{ km s}^{-1}$ . Channel separations are  $20.73 \text{ km s}^{-1}$ . Contour levels are multiples of the r.m.s. map noise of 0.56 mJy/Beam:  $\sigma \times [2, 3, 4, 6, 8, 10]$ . Moving from left to right on the x-axis of the plot corresponds to moving from NE to SW along the projected major axis of the outer HI ring. . . . . 83

Figure 3.5: High sensitivity velocity profile along the major axis of the outer HI ring of NGC 2685 at P.A. =  $35^\circ$ , derived from the naturally weighted map cube. The spatial resolution is  $34''.34 \times 33''.64$  and the velocity resolution is  $24.876 \text{ km s}^{-1}$ . Channel separations are  $20.73 \text{ km s}^{-1}$ . Contour levels are multiples of the r.m.s. map noise of 0.34 mJy/Beam:  $\sigma \times [2, 4, 6, 10, 20, 30, 40, 50]$ . Moving from left to right on the x-axis of the plot corresponds to moving from NE to SW along the projected major axis of the outer HI ring. . . . . 84

- Figure 3.6: High resolution velocity profile along the major axis of the inner, “polar” ring of NGC 2685 at P.A. =  $110^\circ$ , derived from the smoothed uniformly weighted map cube. The spatial resolution is  $14''.00 \times 14''.00$  and the velocity resolution is  $24.876 \text{ km s}^{-1}$ . Channel separations are  $20.73 \text{ km s}^{-1}$ . Contour levels are multiples of the r.m.s. map noise of  $0.56 \text{ mJy/Beam}$ :  $\sigma \times [2, 3, 4, 6, 8, 10]$ . Moving from left to right on the x-axis of the plot corresponds to moving from SE to NW along the projected major axis of the inner HI ring. . . . . 85

Figure 3.7: High sensitivity velocity profile along the major axis of the inner, “polar” ring of NGC 2685 at P.A. =  $110^\circ$ , derived from the naturally weighted map cube. The spatial resolution is  $34''.34 \times 33''.64$  and the velocity resolution is  $24.876 \text{ km s}^{-1}$ . Channel separations are  $20.73 \text{ km s}^{-1}$ . Contour levels are multiples of the r.m.s. noise of  $0.34 \text{ mJy/Beam}$ :  $\sigma \times [2, 4, 6, 10, 20, 30, 40, 50]$ . Moving from left to right on the x-axis of the plot corresponds to moving from SE to NW along the projected major axis of the inner, polar ring of NGC 2685. . . . . 86

Figure 3.8: Naturally weighted, clean HI channel maps of MCG +10–13–030. The mean line of sight, heliocentric velocity is printed at the top of each map. Contour levels are multiples of the approximate r.m.s noise of  $0.32 \text{ mJy/Beam}$ :  $\sigma \times [-5, -2.5, 2.5, 5, 10, 20, 30, 40, 50, 60]$ . These maps have a spatial resolution of  $34''.34 \times 33''.64$ , a beam position angle of  $82^\circ.94$ , and channel separations of  $20.73 \text{ km s}^{-1}$ . Distance labels on x and y axes are in arcminutes W and N of NGC 2685, respectively. Minor tick marks are at 30 arcsecond intervals and major tick marks correspond to the distance in arcminutes from pointing center. North is at the top and West is to the right in these maps. . . . . 88

Figure 3.9: HI emission detected NE of NGC 2685. Contour intervals are in multiples of the r.m.s. noise of  $0.32 \text{ mJy/Beam}$ :  $\sigma \times (-5, -4, -3, 3, 4, 5, 6)$ , with negative contours as broken lines. The spatial resolution is  $34''.34 \times 33''.64$  with a beam position angle of  $82^\circ.94$ , and channel separations of  $20.73 \text{ km s}^{-1}$ . Distance labels on the x and y axes are in arcminutes from NGC 2685, measured positive to the N and negative to the E. Minor tick marks are at 30 arcsecond intervals. North is to the top and West to the left. . . . . 91

Figure 3.10: Global HI profile for NGC 2685 computed from masked and primary beam corrected, naturally weighted channel maps. . . . . 92

Figure 3.11: Global HI profile for MCG+10–13–030. The solid line gives the profile derived following the correction for primary beam attenuation. The dashed line gives the profile derived from the original, naturally weighted map cube. . . . . 93

Figure 3.12: Integrated-intensity of HI for NGC 2685 derived from maps made with natural weighting of the visibilities. The contours are shown over an optical (blue) image of the galaxy obtained from a Palomar Sky Survey print. Contour intervals are in fractions of the map maximum of  $1.53 \times 10^3 \text{ Jy/Beam} \times \text{m/s} \times [0.03, 0.05, 0.1, 0.2, 0.3, 0.4, 0.5, 0.6, 0.7, 0.8, 0.9, 1.0]$ . The map maximum corresponds to an HI column density of  $1.47 \times 10^{21} \text{ atoms cm}^{-2}$ . North is at the top and East to the left. Stars in the field are marked with small +'s. The spatial resolution, as given by the HPBW of the synthesized beam, is  $34''.34 \times 33''.64$  with a beam position angle of  $82^\circ.95$ . . . . . 95

Figure 3.13: Intensity-weighted mean velocity field of NGC 2685 derived from maps made with natural weighting of the visibilities. The contours are shown over an optical (blue) image of the galaxy obtained from a Palomar Sky Survey print. Contour intervals are in  $\text{km s}^{-1}$ , for values at the center of each channel. The observations are centered on  $870 \text{ km s}^{-1}$ . Stars in the field are marked with small +'s. The spatial resolution of the map is  $34''.34 \times 33''.64$  with a beam position angle of  $82^\circ.95$ , and the velocity resolution of the observations is  $24.876 \text{ km s}^{-1}$ . . . . . 96

Figure 3.14: Integrated-intensity of HI for NGC 2685 derived from maps made with uniform weighting of the visibilities. The contours are shown over an optical (blue) image of the galaxy obtained from a Palomar Sky Survey print. Contour intervals are in fractions of the map maximum of  $288 \text{ Jy/Beam} \times \text{m/s} \times [0.2, 0.4, 0.6, 0.8, 1.0]$ . The map maximum corresponds to a column density of  $2.8 \times 10^{21} \text{ atoms cm}^{-2}$ . North is at the top and East is to the left. Stars in the field are marked with small +'s. The spatial resolution, as given by the HPBW of the synthesized beam, is  $11''.46 \times 9''.99$  with a beam position angle of  $52^\circ.33$ . . . . . 97

Figure 3.15: Velocity profile of NGC 2685 taken along a position angle of zero degrees. This profile was derived from the smoothed uniformly weighted map cube. The spatial resolution is  $14''.00 \times 14''.00$  and the velocity resolution is  $24.876 \text{ km s}^{-1}$ . Channel separations are  $20.73 \text{ km s}^{-1}$ . Contour levels are multiples of the r.m.s. map noise of  $0.56 \text{ mJy/Beam}$ :  $\sigma \times [2, 3, 4, 6, 8, 10]$ . Moving from left to right on the x-axis of the plot corresponds moving from S to N through the center of the galaxy. . . . . 99

Figure 3.16: Integrated-intensity of HI for MCG+10-13-030 derived from maps made with natural weighting of the visibilities. Contour intervals are in fractions of the map maximum of  $851.2 \text{ Jy/Beam} \times \text{m/s} \times [0.03, 0.05, 0.1, 0.2, 0.3, 0.4, 0.5, 0.6, 0.7, 0.8, 0.9, 1.0]$ . The map maximum corresponds to an HI column density of  $8.18 \times 10^{20} \text{ atoms cm}^{-2}$ . The North is at the top and East to the left. The spatial resolution is given by the HPBW of the synthesized beam,  $34''.34 \times 33''.64$ . Axes are labeled in terms of arcminutes from the center of NGC 2685. . . . . 102

Figure 3.17: Intensity-weighted mean velocity field of HI for MCG+10-13-030 derived from maps made with natural weighting of the visibilities. North is at the top and East to the left. Contour intervals are in units of  $\text{km s}^{-1}$ . The spatial resolution is given by the HPBW of the synthesized beam,  $34''.34 \times 33''.64$ . The velocity resolution of the observations is  $24.878 \text{ km s}^{-1}$ , and the channel separation is  $20.73 \text{ km s}^{-1}$ . Axes are labeled in terms of arcminutes from the center NGC 2685. . . . . 103

Figure 3.18: The galaxy NGC 660. The image was obtained from an exposure using a plate with a III-aJ emulsion. North is at the top and East is to the left of North. Reproduced with permission from the Royal Observatory in Edinburgh, Scotland. . . . . 105

Figure 3.19: Continuum Emission at 20 cm from NGC 660 derived from maps made with uniform weighting of the visibilities. Contour levels are multiples of the r.m.s. noise level of the map,  $0.45 \text{ mJy/Beam}$ ; i. e.,  $\sigma \times [2, 5, 10, 20, 40, 60, 100, 200, 400]$ . The map maximum is  $185.72 \text{ mJy/Beam}$ . The spatial resolution of the maps is  $14''.43 \times 12''.25$ , with a beam position angle of  $-72''.59$ . The “f” signs mark star positions for comparison with optical maps. Distances are in term of arcminutes from the pointing center of the observations. North is at the top of the map and East is to the left. . . . . 115

Figure 3.20: Continuum Emission at 20 cm from the double source in the SW part of the map of NGC 660. Contour levels are multiples of the r.m.s. noise level of the map, 0.45 mJy/Beam; i. e.,  $\sigma \times [2, 5, 10, 20, 40, 60, 100, 200, 400]$ . The peak of this source is 85.2 mJy/Beam. The spatial resolution of the maps is  $14''.43 \times 12''.25$ , with a beam position angle of  $-72^\circ.59$ . Distances are in terms of arcminutes from the pointing center. North is at the top of the map and East is to the left. . . . . 116

Figure 3.21: Uniformly weighted, clean channel maps showing the distribution of HI in NGC 660. The mean line of sight, heliocentric velocity for each map is printed at the top. Contour levels are multiples of the approximate r.m.s noise of 0.81 mJy/Beam:  $\sigma \times [-25, -15, -10, -7, -5, -3, 3, 5, 7, 10, 15, 20, 25]$ . The spatial resolution of the maps is  $14''.43 \times 12''.25$  and the beam position angle is  $-72^\circ.59$ . The channel separation is  $20.73 \text{ km s}^{-1}$ , and the velocity resolution is  $24.876 \text{ km s}^{-1}$ . The pointing center for the observations,  $(\alpha, \delta)_{1950} = (01^\text{h} 40^\text{m} 20^\circ.8, 13^\circ 23' 30'')$ , corresponds to (0,0). Positions of stars in the optical image are marked with "+" signs. Minor tick marks are at 15 arcsecond intervals and major tick marks are labeled every two arcminutes from pointing center. North is at the top and West is to the right. . . . . 118

Figure 3.21: -- continued . . . . . 119

Figure 3.21: -- continued . . . . . 120

Figure 3.21: -- continued . . . . . 121

Figure 3.22: Global HI profile for NGC 660. . . . . 123

Abstract of Dissertation Presented to the Graduate School  
of the University of Florida in Partial Fulfillment of the  
Requirements for the Degree of Doctor of Philosophy.

PROGRADE ANOMALOUS ORBITS IN TRIAXIAL GRAVITATIONAL  
POTENTIALS THAT ROTATE ABOUT THE LONG AXIS: VLA  
NEUTRAL HYDROGEN OBSERVATIONS AND MODELING OF THE  
INCLINED RINGS AROUND THE GALAXIES NGC 2685 AND NGC 660

By

Mary Elaine Mahon

May, 1992

Chairman: Dr. Stephen T. Gottesman

Major Department: Astronomy

This dissertation presents the results of a systematic study of the inclined family of prograde anomalous orbits in rotating, triaxial gravitational potentials. In particular, for the case where the long axis of the potential is the rotation axis, the bifurcation sequence of orbits containing the prograde anomalous family is explored as a function of the rotation speed of the potential. Neutral hydrogen observations of the galaxies NGC 2685 and NGC 660 obtained with the Very Large Array Radio Telescope (VLA) are also presented. Maps derived from these observations show that both galaxies contain two kinematically distinct systems of gas, one in a nearly polar orientation, and the other approximately in the plane of the central stellar disk. If the underlying gravitational potential of the galaxy is triaxial and rotating, such configurations can be stable. It is shown that a model constructed from an ensemble of orbits, which contains the stable anomalous and prograde elliptical families, yields velocity and surface density maps similar to those derived from the VLA neutral hydrogen observations of NGC 2685 and NGC 660. The real interest of such a treatment is that, unlike the case for

rotation about the short axis of the potential, it allows for the stars and gas in the disk of the central galaxy to rotate in the same sense. These models indicate that for both NGC 2685 and NGC 660, the underlying gravitational potential is mildly triaxial and slowly rotating. An understanding of the shape of gravitational potential for these peculiar galaxies ultimately may lead to a better understanding of the three-dimensional distribution of matter in normal elliptical and spiral galaxies.

## CHAPTER 1

### INTRODUCTION

One of the central problems in contemporary astronomy concerns the distribution of matter in galaxies. The presence of nonluminous matter in our galaxy, the Milky Way, was first suggested by Oort (1932), following an analysis of the numbers and velocities of stars near the sun. Oort concluded that the luminous matter could only account for 30–50% of the gravitating matter implied by the observed stellar velocities. Over 50 years later, an analysis of the distribution and velocities of F dwarf and K giant stars by Bahcall (1984b,c) seemed to support this assertion, giving a ratio of dark to luminous matter between 0.5 and 1.5. However, a more recent analysis by Gilmore (1989), using Bahcall's (1984a) algorithm and samples from three different populations of F stars, indicates that the available F-star data cannot provide conclusive evidence either for or against the presence of nonluminous matter near the sun. Furthermore, an analysis of older F stars and K giants by Kuijken and Gilmore (1989) provides no evidence of unidentified matter near the sun. Thus, the question of dark matter in the solar neighborhood remains open. However, beyond the solar neighborhood, there is strong dynamical evidence for nonluminous matter in the Milky Way. This evidence is in the form of the Galactic rotation curve.

The rotation curve for our galaxy derived from stars (Avedisova, 1985) and from combined optical and radio data on HII regions (Brand, 1986) is relatively flat out to at least 15 kpc, indicating that the dynamical mass increases monotonically with R. The total mass indicated by the observed rotational velocities at such large distances cannot

be accounted for in the form of identified luminous matter. Thus, beyond the sun, the mass to luminosity ratio for the Galaxy appears to be an increasing function of R. Due to the absence of suitable tracers in the disk, it is not possible to measure the rotation curve for our galaxy far beyond 15 kpc; thus, either the dynamics of Population II tracers such as halo stars and globular clusters or the dynamics of satellite galaxies must be used to probe the dark matter distribution at large distances where the galactic rotation curve cannot be measured directly.

Some studies of halo star, cluster, and satellite velocities seem to suggest an extended massive dark halo about the galaxy for which  $R \gtrsim 90$  kpc and  $M \sim 5 \times 10^{11} M_{\odot}$  (Peterson, 1985 and Olszewski, Peterson, and Aaronson, 1986). Other studies, such as that of Little and Tremaine (1987), indicate a less extensive massive halo for which  $R \lesssim 50$  kpc and  $M \sim 2.4 \times 10^{11} M_{\odot}$ . Though these estimates of the total mass of our galaxy and the extent of its halo disagree by roughly a factor of two, even the more conservative estimate of Little and Tremaine (1987) supports the existence of a massive Galactic halo containing significant amounts of nonluminous matter.

Ten years before Hubble showed that spiral nebulae were galaxies, rotation in external galaxies was detected through measurements of Doppler shifted lines in galactic spectra (Slipher, 1914). Early optical measurements of velocities in spiral galaxies were primarily restricted to the inner parts of the stellar disks. Rotation curves derived from these measurements typically show a steep, linear rise in circular velocity, followed by a turnover region beyond which the curves level off and remain level for a short distance to the last measured point. Models of rotation curves for disks with exponential surface density distributions fit these data well in the inner parts; however, at large distances, where the disk potential resembles that of a point mass, rotation speeds given by exponential disk models are expected to fall off in a Keplerian fashion as

$1/\sqrt{R}$ . It was not until the 1970s, when there was a dramatic improvement in the sensitivity of optical and radio measurements, that it became completely clear that very few galaxies exhibit falling rotation curves. That such non-Keplerian rotation curves were a widespread phenomenon was first suggested by Freeman (1970), who concluded that other spiral galaxies with flat rotation curves, such as NGC 300 and M33, might possess massive dark halos extending well beyond the optical disk.

The construction of large aperture-synthesis radio telescopes, such as the Very Large Array in New Mexico, have made it possible to map the full two-dimensional distribution and velocity field of neutral hydrogen for many galaxies. These observations typically extend out to 2–3 times the optical radius of the system. Although sensitivity considerations generally limit the velocity resolution to 20–40 km s<sup>-1</sup>, in some cases of nearby gas-rich systems, a velocity resolution of up to 5 km s<sup>-1</sup> can be obtained. HI observations of more than 70 spirals reveal flat or rising rotation curves for most of the galaxies (Rogstad and Shostak, 1972; Faber and Gallagher, 1979; Rubin, Ford, and Thonnard, 1980, 1982; Rubin, Burstein, Ford, and Thonnard, 1985; and Begeman, 1987). However, a number of falling rotation curves have been observed recently (van Gorkom, 1992). Even so, studies of the distribution of dark matter in samples of normal spiral and elliptical galaxies by Ostriker, Peebles, and Yahil (1974) and Einasto, Kaasik, and Saar (1974) indicate a linear increase in  $M(R)$  out to at least 100 kpc and  $10^{12} M_{\odot}$ .

Two-component models consisting of a luminous stellar disk (Carignan and Freeman, 1985 and van Albada and Sancisi, 1986) and a dark halo represented by a truncated isothermal sphere or other similar form (van Albada, Bahcall, Begeman, and Sancisi, 1985) have been quite successful in reproducing the rotation curves derived from spectral line observations. The dark matter implied by the observed velocities in the disks is usually assumed to lie in a spherical component; however, since the derived rotation

curves are limited to the plane of galactic disks, they cannot be used to test this assumption. Furthermore, massive halos are not always required to produce flat rotation curves in disks. Some of the rotation curves, especially the optical ones, can also be fit by a model of a truncated disk with constant M/L (Kalnajs, 1983). The effects of disk truncation have been considered in detail by Hunter, Ball and Gottesman (1984), and several examples have been observed.

Theoretically, heavy halos can be invoked to stabilize thin cold disks against bar mode instabilities, but this argument is not compelling since there are a number of other ways to damp bar modes in a disk. For instance, a cold disk can be stabilized by addition of a hot halo of only about one disk mass inside the disk radius, with most of the mass of the halo accounted for by the visible spheroid (Athanassoula and Sellwood, 1986). Alternatively, a suitably heated disk can be stabilized by the addition of a halo of comparable mass (Hunter and Moore, 1992); however, these numerical experiments give considerably larger velocity dispersions than what observations indicate. Independent support for a halo/disk mass of unity inside a disk radius is given by work on the multiplicity of spiral arms as a function of the halo to disk mass ratio (Athanassoula, 1986).

There are only a few observational probes of the dark matter distribution and these include: i) HI disks that widen (flare) at large radii; ii) warped disks (usually in the HI and sometimes in the stellar component); and iii) polar ring galaxies. Flared HI disks have been interpreted to imply that the dark matter is distributed in either a spheroidal halo or in a disk several kiloparsecs thick (Lewis, 1987), while arguments put forth to explain warped disks include: i) massive spherical halos to stabilize warps against differential precession (Tubbs and Sanders, 1979); ii) discrete bending modes in isolated self-gravitating disks (Lynden-Bell, 1965 and Hunter and Toomre, 1969), as well as in

disks that are smoothly truncated over a narrow region (Sparke and Casertano, 1988); and iii) discrete bending modes in disks subject to the gravitational potential of an inclined, flattened dark halo (Petrou, 1980; Dekel and Shlosman, 1983; and Sparke and Casertano, 1988).

Polar ring galaxies exhibit rings of stars, dust, and gas orbiting in planes nearly perpendicular to the plane of the central, stellar disk. They thus provide a unique opportunity to probe the three dimensional shape of the gravitational potential far from the center of the galactic disk. Information on the shape of the halo can be derived by fitting models simultaneously to observed velocities in the disks and polar rings of these galaxies.

A polar ring system consists of a central disk galaxy and a luminous ring of gas, dust, and stars highly inclined to the disk of the galaxy. In most cases, these rings do not assume a strictly polar orientation. Rings inclined 15–20° from a polar orientation are quite common, while rings inclined more than 30–70° from the pole are quite rare (Whitmore, 1984 and Whitmore, Lucas, McElroy, Steiman-Cameron, Sackett, and Olling, 1990). Polar rings tend to be larger than the disk of the central galaxy and usually extend several times further in radius. The rings are not always planar, but the bending usually does not appear to be severe (Wakamatsu and Arp, 1983 and Schweizer, Whitmore, and Rubin, 1983). Some polar rings have been observed to contain  $\gtrsim 1 - 3 \times 10^9 M_\odot$  of HI gas (Schweizer et al., 1983; Shane, 1980; van Gorkom, Schechter, and Kristian, 1987; and Gottesman and Mahon, 1990). The central galaxies of most polar ring systems are observed to have low central stellar velocity dispersions and substantial rotational velocities, consistent with the interpretation that the central stellar component is actually an SO disk (Whitmore et al., 1990). Furthermore, most of these central galaxies appear to be unexceptional in terms of their colors (Gagen-Torn,

Popov, and Yakovleva, 1983 and Mould, Balick, Bothun, and Aaronson, 1982) and HI content (Schechter, Sancisi, van Woerden, and Lynds, 1984).

Polar ring galaxies are often found in binary systems or in small, loose apparent groups, but not in clusters (Athanassoula and Bosma, 1985). It has been suggested that this may be an environmental effect; i. e., polar rings accreted in a higher density cluster environment would be subject to tidal disruption on the order of once every  $10^9$  years (Sparke, 1991).

Polar ring galaxies do not seem to be very common objects. Only about 0.5% of all nearby SO galaxies appear to have polar rings; however, this percentage may be increased to about 5% if one tries to correct for selection effects (Whitmore et al., 1990). Whitmore et al. (1990) divide the galaxies in the "Polar Ring Catalogue" into four categories: (a) kinematically determined polar rings (six objects), for which spectroscopic evidence exists for two nearly orthogonal angular momentum vectors of similar amplitude; (b) good candidates (27 objects), for which the projected major axes of the two components are nearly orthogonal and the ring is luminous, nearly planar, and centered on the galaxy; (c) possible candidates (73 objects); and (d) systems possibly related to Polar-Ring galaxies (42 objects) which are divided into eight classes. These classes are dust-lane ellipticals; systems with box, peanut, and X-shaped bulges; "Mayall-type" objects; smoke-ring galaxies; superpositions; "theta" galaxies; "Hoag-type" galaxies; and kinematically related objects.

So far only six systems have been observed in enough detail to establish their status as SO galaxies with polar rings: NGC 2685 (Schechter and Gunn, 1978 and Shane, 1980), A 0136-0801 (Schweizer, Whitmore, and Rubin, V. C., 1983), NGC 4650A and ESO 415-G26 (Whitmore, McElroy, and Schweizer, 1987a), and UGC 7576 and UGC 9796 (II ZW73) (Schechter et al., 1984). These systems have been classified as category

(a) systems by Whitmore et al. (1990). One of the polar ring candidates, AM 2020–504, was found to exhibit characteristics of both a disk galaxy and an elliptical galaxy; i.e., the inner region shows rapid rotation like a disk galaxy, while the luminosity profile of the central galaxy follows the  $R^{1/4}$  law with a slowly rotating outer region, like an elliptical galaxy (Whitmore, McElroy, and Schweizer, 1987b). So far, AM 2020–504 and twenty six other galaxies have been found that satisfy the criteria for category (b) (Whitmore et al., 1990).

The existence of a ring rotating at roughly right angles to the disk of the central galaxy is difficult to understand in terms of a collapse of a single protogalactic gas cloud. Therefore, it has been argued that polar rings result from a secondary accretion event such as capture of a gas rich dwarf via dynamical friction, or mass transfer during a close encounter with a companion galaxy (Whitmore et al., 1987a). Schweizer et al. (1983) suggest that the stellar material captured during such an encounter would disperse into the halo around the main disk, while the gaseous material would suffer viscous dissipation and quickly settle into a new disk with an angular momentum vector roughly perpendicular to the original orbital plane. Tohline and Durisen (1982) estimate the settling time scale in an axisymmetric galaxy to be  $10^8 - 10^9$  years. Star formation would be expected to occur in the ring following the capture.

A theoretical understanding of how polar ring galaxies form and how frequently they form is important in that it may lead us to a better understanding of normal galaxies. In general, studies of polar ring galaxies focus on two principal issues: i) the shape of the gravitational potential and ii) the age and stability of polar ring systems. If the gravitational potential of a polar ring galaxy was exactly spherical at every radius, there would be no differential precession and a polar ring configuration at any angle would be stable. However, the fact that polar rings are usually found

to deviate somewhat from a strictly polar orientation seems to indicate that the mass distribution is non-spherical (Schweizer et al., 1983). Comparison of equatorial to polar rotation curves for the polar ring systems A0136-0801 (Schweizer et al., 1983), NGC 4650A, and ESO 415-G26 (Whitmore et al., 1987a) led these authors to conclude that the dominating mass within 0.6 R<sub>25</sub> has a nearly spherical distribution. However, Sackett and Sparke (1990) found that models of NGC 4650A, for which the dark halo is substantially flattened, give results compatible with the data for this galaxy. Thus, polar rings might be quasi-stable oblate, prolate, or triaxial configurations with settling times determined by differential precession (Steiman-Cameron and Durisen, 1982), or they might be stable equilibrium configurations in tumbling triaxial potentials (Heisler, Merritt and Schwarzschild, 1982; Magnenat, 1982; and van Albada, Kotanyi, and Schwarzschild, 1982). For this dissertation, we will assume that polar rings are quasi-stable configurations in rotating triaxial potentials.

Estimates for ages of polar rings can be obtained from arguments based on either photometry and spectroscopy of the rings, or from theoretical and numerical studies of the time required for captured material to assume a steady-state configuration. Spectroscopic and photometric estimates are based on the level of symmetry of the rings; the smoothness of the rings; indications of star formation activity in the recent past, such as strong Balmer absorption near the center of the SO, the presence of optical emission lines, or whether the rings are blue in color; and if any evidence remains from the interaction such as shell structures in outer regions or tidal debris (Whitmore et al., 1987a).

Theoretical and numerical age estimates hinge on an understanding of the possible equilibrium configurations for different potentials and geometries. There are three major approaches to this problem: i) the preferred plane method, in which the location

of stable preferred orbital planes for gas in near spherical potentials is found via perturbation analysis and numerical modeling of the effects of dissipative differential precession on captured gas rings (see Steiman-Cameron and Durisen 1982, 1984, 1988 and references therein); ii) the method of finding stable equilibria for self-gravitating polar rings in flattened halo potentials (Sparke, 1986 and Sackett and Sparke, 1990); and iii) analysis of stable, non-intersecting periodic orbits in a given potential (Heiligman and Schwarzschild, 1979; Heisler et al., 1982; Magnenat, 1982; Merritt and de Zeeuw, 1983; de Zeeuw and Merritt, 1983; and Martinet and Pfenniger, 1987). This dissertation is concerned with the last approach.

The evolution of a thin disk with arbitrary initial orientation, subject to both precessional and dissipative forces in the gravitational potential of a nonspherical galaxy has been studied in detail by Steiman-Cameron and Durisen (1988, 1990), Tubbs (1980), Tohline, Simonson, and Caldwell (1982), Habe and Ikeuchi (1985, 1988), and Christodoulou (1990). Newly accreted material is expected to spread into an annular disk on a timescale of a few orbital periods, after which, according to these models, the three-dimensional structure of the newly formed disk evolves on longer precessional and dissipative time scales (Steiman-Cameron, Kormendy, and Durisen, 1992). In this picture, differential precession causes a smooth continuous twist to develop, while dissipation within the twisted disk leads to the transport of angular momentum, thereby causing changes in the orientation of the disk and inflow of material towards the center (Steiman-Cameron et al., 1992). Through the combined effects of dissipation and differential precession, the disk eventually settles towards a preferred plane which, by definition, satisfies the following conditions: i) an orbit in that plane will not undergo nodal precession about any axis and ii) orbits slightly inclined to it will precess about the pole of the preferred plane (Dobrovolskis, 1980). These studies emphasize a picture

of a continuous, warped disk whereby viscosity acts to restore the planarity of the disk, which can only be achieved in one of the stable planes. However, if such a disk is sufficiently massive, self-gravity can complicate this process (Hunter and Toomre, 1969; Sparke, 1984; and Sparke and Casertano, 1988).

The mutual attraction of particles in a polar ring may act to stabilize a ring against differential precession, thus forcing the ring to precess as a unit (Sparke, 1986). A self-gravitating polar ring may precess uniformly as a solid body about an axisymmetric galaxy if the ring is of sufficient mass, and if its tilt varies suitably with radius; thus, for example, a massive polar ring can remain stable to differential precession if it warps toward the pole on the outside, as it does in the case of NGC 4650 (Sackett and Sparke, 1990). Moreover, a polar ring around an axisymmetric galaxy can be long-lived if the ring is massive enough (on the order of several billion solar masses) for self-gravity to be important (Sparke, 1986, 1991).

In the forgoing discussion, polar rings have been considered in the context of stationary, axisymmetric potentials in which the evolution of the ring towards a stable configuration is governed by the combined effects of differential precession, self-gravity, and dissipation. That polar rings might be stabilized by a tumbling prolate or triaxial potential was proposed by van Albada, Kotanyi and Schwarzschild (1982) and by Tohline and Durisen (1982). Therefore, studies concerning the existence and stability of periodic orbits in both stationary and rotating triaxial potentials are central to this problem. The earliest, extensive investigations for the latter case were carried out for sequences of closed orbits in the equatorial plane (Contopoulos and Papayannopoulos, 1980), while closed orbits out of the equatorial plane were studied by Binney (1978, 1981), Heiligman and Schwarzschild (1979), Heisler et al. (1982), Magnenat (1982), Contopoulos and Magnenat (1985), and Contopoulos (1986a, 1986b). These authors used direct numerical

orbit integrations, supplemented by linear stability analyses, to locate periodic orbits and test their stability in various geometries, while Binney (1978, 1981), through an analytic perturbation analysis, considered the stability of periodic orbits in the principal planes of a tumbling, slightly triaxial potential. These studies indicate that important information could be obtained about the shape and tumble speed of the gravitational potential of a polar ring galaxy if one can model the ring as an ensemble of stable, non-crossing periodic orbits in a rotating triaxial potential.

The principal aim of this research is twofold. First, the properties of stable orbits in a rotating triaxial gravitational potential, in particular, the family of stable anomalous orbits, will be explored numerically as a function of the shape and tumble speed of the gravitational potential. Second, we seek to constrain the shape and rotation of the potential for two different polar ring systems, NGC 660 and NGC 2685, by modeling the observed HI velocity field for each galaxy from ensembles of stable periodic orbits in potentials with specific geometries and rotation.

At the beginning of Chapter 2 there is a review of the literature on orbits in rotating triaxial potentials and a description of the computational methods employed for this numerical study of orbits in rotating triaxial gravitational potentials. The remainder of Chapter 2 is devoted to a detailed discussion of the results from this study regarding the form of the bifurcation sequence containing the stable family of prograde anomalous orbits, as a function of shape and tumble rate of the triaxial potential. In addition, various properties of the orbits in this sequence are discussed in the context of orbit models that assume that gas clouds in the inclined rings around the galaxies NGC 2685 and NGC 660 are following trajectories defined by an ensemble of stable, non-crossing orbits from the inclined prograde anomalous family, as well as from families of elliptical orbits in the equatorial plane of the potential, which is assumed to be triaxial.

In the first part of Chapter 3, there is a review of the theory and techniques of aperture synthesis as related to observations made with the Very Large Array radio telescope (VLA). First, observations of the galaxy NGC 2685 are considered and then those for the galaxy NGC 660. For each galaxy there is a review of the published observations; a description of the VLA observing run, including a discussion of the instrumental parameters, the calibration and editing of the observed visibilities, and the mapping; and finally, a detailed discussion of the spatial and velocity distribution of neutral hydrogen in each galaxy as derived from these observations. Dwarf companions to each of these galaxies were also detected in HI, MCG 10-13-030 and UGC 1195. A description of the neutral hydrogen characteristics of these satellite systems is provided in the respective sections on NGC 2685 and NGC 660.

Chapter 4 is concerned with orbit models of the HI gas observed in the rings of NGC 2685 and NGC 660. The methods used to construct such models for comparison with observations are described. Results from these models are presented in the form of integrated-intensity and intensity-weighted velocity maps, and a discussion of the implications of such models regarding the distribution of matter in these galaxies is provided.

Finally, Chapter 5 summarizes the principal numerical results obtained from a numerical analysis of orbits in rotating triaxial potentials, as well as the observational results regarding the distribution of HI in the polar ring galaxies NGC 2685 and NGC 660. Both the numerical and observational research described herein can stand alone; i.e., they are independent areas of research. However, for this dissertation, a serious attempt has been made to unite these areas, through development of a method for modeling VLA HI observations in terms of orbits in rotating triaxial potentials. The results from these models, given that the basic underlying assumptions are valid, may

give us insight into the overall distribution of matter in the peculiar galaxies NGC 2685 and NGC 660. It is hoped that such an understanding may, in the future, help us to understand the distribution of matter around more common systems such as elliptical galaxies and spiral galaxies.

## CHAPTER 2

### ORBITS IN ROTATING TRIAXIAL POTENTIALS

#### Review of Previous Work on Orbits in Triaxial Potentials

##### Stationary Triaxial Potentials

There are six major families of simple periodic orbits in a nonrotating triaxial potential: three radial orbit families, one along each of the principal axes; and three families of closed elliptical orbits, one in each of the principal planes of the potential. In stationary potentials, both retrograde orbits circling the short axis of the potential, and prograde orbits circling the long axis of the potential, are stable; however, orbits that circle the intermediate axis, whether prograde or retrograde, are unstable (Heiligman and Schwarzschild, 1979; Binney, 1981; and Magnenat, 1982). The generality of this result was confirmed analytically by Binney (1981), while numerical confirmation was obtained by Magnenat (1982) who performed orbit calculations in a series of triaxial logarithmic potentials ranging in shape from strongly prolate to oblate. In addition, Magnenat (1982) investigated the stability of the elliptical orbits in a stationary potential as a function of the shape of the potential. He found that for values of the shape parameters corresponding to a very prolate logarithmic potential, the elliptical orbits arise by bifurcation from the short axis family of radial orbits. Thus, in stationary potentials with shapes less prolate than this, or even oblate, the stability of the elliptical orbits in the principal planes depends on which of the principal axes of the potential are

aligned with the orbit's rotation axis, as well as on the sense of the orbit's rotation. The two families of stable elliptical orbits parent two major families of general, non-periodic orbits which are trapped around the stable periodic orbits: the short axis tube orbits and the long axis tube orbits. A third major family of general orbits, the box orbits, arises from the long axis family of radial orbits (Goodman and Schwarzschild, 1981).

### Orbits in Rotating Triaxial Potentials

#### Rotation about the short axis of the potential

In a triaxial potential that is slowly rotating about its short axis (the z-axis), there are four main families of orbits: the inclined family of stable, retrograde anomalous orbits, which circle the short axis of the potential; the inclined family of unstable, retrograde anomalous orbits, which circle the intermediate axis of the potential; the family of retrograde elliptical orbits, which circle the short, rotation axis of the potential; and the z-axis family of radial orbits. These orbits were first computed numerically by Merritt in 1979, whose unpublished calculations are cited by van Albada, Kotanyi, and Schwarzschild (1982). Later, the anomalous orbits were derived by Tohline and Durisen (1981) using an approximate, but general, analytical method. In the absence of figure rotation, the inclined family of retrograde anomalous orbits corresponds directly to the family of closed, retrograde elliptical orbits circling the short axis of the potential. The Coriolis force introduced by the rotation of the potential about the short axis acts to tip the orbits away from the plane containing the short and intermediate axes of the potential. The tilt of the orbit away from the plane increases with orbital energy, until

the sequence of anomalous orbits terminates in the equatorial plane (Heisler, Merritt and Schwarzschild, 1982).

A connection between the family of normal retrograde orbits in the equatorial plane of a triaxial potential rotating on its short axis, and the anomalous orbits was first suggested by Binney (1981). The retrograde family manifests an instability against vertical perturbations over a certain energy range, now referred to as the Binney instability strip. Binney (1981) suggested that a relation existed between this instability and the termination of the anomalous orbits. This relation between the instability strip for the retrograde family of orbits and the stable anomalous orbits was thoroughly studied by Heisler et al. (1982).

Heisler et al. (1982) numerically demonstrated the interconnection between the four major families of periodic orbits in a triaxial gravitational potential rotating about its short axis, and the retrograde family of orbits in the equatorial plane. This work revealed that the retrograde anomalous orbits only exist over a limited range of energy. At low values of the energy the stable and unstable families of retrograde anomalous orbits arise by bifurcation from the z-axis family of radial orbits at its transition from linearly stable to simply unstable ( $S \rightarrow U$ ) and simply unstable to double unstable ( $U \rightarrow D$ ), respectively. For increasing values of the energy, both the unstable and stable retrograde anomalous orbits tilt away from the plane containing the rotation axis of the potential until they join the retrograde family of orbits on the equatorial plane, at the inner and outer edges of the Binney instability strip, respectively. Martinet and Pfenniger (1987) later showed that namely, for potentials rotating faster than a certain critical speed, this bifurcation sequence undergoes a qualitative change.

For potentials tumbling at speeds higher than a critical value,  $\Omega_{\text{crit}}$ , the z-axis family of orbits undergoes a transition from stability to complex instability (Martinet and

Pfenniger, 1987). Complex instability of periodic orbits appears both in time-dependent 2-D systems, and in time-independent, conservative systems of three dimensions and higher. Complex instability in the context of dynamical models has been studied extensively by a number of authors, including Contopoulos and Barbanis (1985), Heggie (1985), Pfenniger (1985), Contopoulos (1986b), Martinet and Pfenniger (1987), Martinet and de Zeeuw (1988), and Patsis and Zachilas (1990). This transition to complex instability (C) prevents the bifurcation of the retrograde anomalous orbits from the z-axis family of radial orbits. Instead, the stable branch of the retrograde anomalous orbits bifurcates from normal family of retrograde orbits in the equatorial plane, at its transition from S→U at the inner edge of the Binney instability strip (Martinet and Pfenniger, 1987 and Martinet and de Zeeuw, 1988). From here, the stable anomalous orbits (SAOs) tilt up from the equatorial plane. The inclination of the orbits to the equatorial plane increases, with increasing orbital energy, to a maximum inclination above the plane, beyond which it decreases, until the retrograde stable anomalous orbits terminate in the equatorial plane. The termination of the retrograde SAOs in the equatorial plane occurs at the outer edge of the Binney instability strip, where the normal family of retrograde orbits undergoes a transition from U→S (Martinet and Pfenniger, 1987). Anomalous orbits in potentials that rotate about the short axis have been studied rather extensively (see van Albada, Kotanyi, and Schwarzschild, 1982; Heisler et al., 1982; Magnenat, 1982; Martinet and Pfenniger, 1987; and Martinet and de Zeeuw, 1988); however, comparatively very little effort has been directed towards anomalous orbits in potentials rotating about their long axes (van Albada, Kotanyi, and Schwarzschild, 1982 and Magnenat, 1982).

---

Rotation about the long axis of the potential

In a triaxial potential that is rotating about its long axis, the stable anomalous orbits are prograde in the rotating frame of the potential (van Albada, Kotanyi, and Schwarzschild, 1979 and Magnenat, 1982). Magnenat (1982) studied the stability of these orbits for two cases of triaxial potentials rotating about the long axis as a function of the figure rotation speed ( $\Omega$ ). For increasing values of  $\Omega$ , orbits in the stable branch of the prograde anomalous family tilt away from the plane containing the intermediate and long axes ( $i$ - $l$  plane), while orbits in the unstable branch tilt away from the plane containing the long and short axes ( $s$ - $l$  plane) of the potential. In a triaxial, but considerably prolate potential, for  $\Omega$  increasing from zero, orbits in the unstable branch of the prograde anomalous family tilt away from the  $s$ - $l$  plane, eventually terminating in the equatorial plane, at the value of  $\Omega$  for which the prograde elliptical family of orbits in the equatorial plane undergoes a transition from S→U (Magnenat, 1982). Likewise, stable orbits in the prograde anomalous family, SAO, tilt away from the  $i$ - $l$  plane; however, Magnenat (1982) noted that the orbits in this family undergo a transition from stability to complex instability (S→C) for increasing values of  $\Omega$ . Magnenat (1982) also noted that the complex unstable orbits do not join the elliptical family in the equatorial plane for the case he studied. Instead, these orbits reach a minimum inclination to the equatorial plane before tilting back up, away from the equatorial plane for increasing values of the Hamiltonian ( $H$ ). In this chapter, we investigate this behavior and show that, for a certain values of  $\Omega$ , collisions of bifurcations occur. Above the value of  $\Omega$  for which a collision of bifurcations occurs, qualitative changes occur in the bifurcation sequence involving the SAOs.

From Magnenat's (1982) study of anomalous orbits in potentials rotating about their long axes, two main conclusions can be derived. First, in potentials rotating about either the long or the short axis, there are two branches of stable anomalous orbits and two branches of unstable anomalous orbits. Initial conditions for each branch of a family are identical except that the sign of the velocity in the direction of the rotation axis is reversed; therefore, the orbits from each branch tilt in opposite directions. However, the component of angular momentum in the direction of the potential's rotation axis is the same for orbits of the same energy in both branches; therefore, both branches of the stable, prograde family of anomalous orbits are prograde in the rotating reference frame of a potential tumbling about its long axis. The second conclusion regards the onset of complex instability in the stable, prograde family of anomalous orbits. Magnenat (1982) found complex instability to characterize the anomalous orbits in only one case, for the stable branch of prograde anomalous orbits in a potential rotating about its long axis. From a rough analysis of the behavior of the phase space trajectories of orbits slightly displaced from one of these complex unstable anomalous orbits, Magnenat (1982) concluded that the phase space volume occupied by a nearby orbit can be very large. In this chapter, we plot the region of complex instability in two different potentials as a function of the value of the Hamiltonian ( $H$ ) and  $\Omega$  and show that even though the complex instability strip is very narrow for low values of  $\Omega$ , it becomes significantly wider for larger values of  $\Omega$ , near the value of  $\Omega$  for which a collision of bifurcations occurs.

That stable anomalous orbits might be responsible for the motions of gas and the warped dust lanes of some elliptical galaxies was first suggested by van Albada, Kotanyi and Schwarzschild (1982). Employing the unpublished orbit calculations of David Merritt, these authors studied SAOs in triaxial potentials for which the rotation axis

could be either the short or long axis of the potential. They attempted to describe the stationary states of motion of gas in dust lane elliptical galaxies in terms of these orbits in a slowly rotating prolate potential, and concluded from this study that the motions of gas and the warped dust lanes in some of these galaxies are consistent with the motions and orientations implied by stable anomalous orbits in rotating triaxial potentials. In the same vein, this dissertation presents the results from a systematic study of stable anomalous orbits in rotating triaxial potentials, as well as quantitative modeling of the observed gas in the inclined rings of the polar ring galaxies NGC 2685 and NGC 660 in terms of these orbits.

In particular, the models described herein are constructed from the following families of stable orbits which are found in triaxial gravitational potentials that rotate about the long axis of the potential: the inclined family of prograde anomalous orbits and the prograde family of elliptical orbits in the equatorial plane. Since such models allow for the stars and gas in the galaxy to rotate in the same sense, they are equally good whether one assumes that polar ring galaxies were formed primordially or via some later merger/accretion event.

### Calculation of Orbits and their Stability

The triaxial gravitational potential employed in this study is logarithmic and of the form

$$\Phi = \frac{v_c^2}{2} \ln \left[ 1 + \frac{x^2}{q_a^2} + \frac{y^2}{q_b^2} + \frac{z^2}{q_c^2} \right], \quad (2.1)$$

where  $x$ ,  $y$ , and  $z$  are given in units of core radii,  $v_c$  is the limiting circular velocity at infinity, and  $q_a$ ,  $q_b$ , and  $q_c$  are parameters that specify the shape of the gravitational potential.

With increasing distance from the center of the galaxy, a circular rotation curve derived from Equation (2.1) with  $q_a = q_b$  exhibits a linear rise in circular velocity up to the core radius, at which point the rotation curve turns over and becomes nearly flat as the circular velocity asymptotically approaches  $v_c$  at infinity. The core radius and  $v_c$  can be treated as free parameters; however, approximate constraints on their values can be established if rotation curve data from spectral line observations are available. Later, these values can be modified to improve agreement between the model and observations of a particular galaxy.

If  $\Omega$  is the rotation speed of the potential,  $(x, y, z)$  are the Cartesian coordinates in the corotating reference frame,  $(p_x, p_y, p_z)$  are the canonically conjugate momenta, and the  $z$ -axis is the rotation axis of the potential, then the Hamiltonian governing the motion for a unit mass test particle is given by

$$H = \frac{1}{2}(p_x^2 + p_y^2 + p_z^2) + \Phi(x, y, z) - \Omega(xp_y - yp_x). \quad (2.2)$$

Denoting time derivatives by dots, the corresponding equations of motion are given by

$$\begin{aligned} \dot{x} &= \frac{\partial H}{\partial p_x} = p_x + \Omega y, \\ \dot{y} &= \frac{\partial H}{\partial p_y} = p_y - \Omega x, \\ \dot{z} &= \frac{\partial H}{\partial p_z} = p_z, \\ \dot{p}_x &= -\frac{\partial H}{\partial x} = -\frac{\partial \Phi}{\partial x} + \Omega p_y, \\ \dot{p}_y &= -\frac{\partial H}{\partial y} = -\frac{\partial \Phi}{\partial y} - \Omega p_x, \\ \dot{p}_z &= -\frac{\partial H}{\partial z} = -\frac{\partial \Phi}{\partial z}, \end{aligned} \quad (2.3)$$

where

$$\left[ \frac{\partial \Phi}{\partial x}, \frac{\partial \Phi}{\partial y}, \frac{\partial \Phi}{\partial z} \right] = \frac{v_c^2}{\left( 1 + \frac{x^2}{q_a^2} + \frac{y^2}{q_b^2} + \frac{z^2}{q_c^2} \right)} \left[ \frac{x^2}{q_a^2}, \frac{y^2}{q_b^2}, \frac{z^2}{q_c^2} \right]. \quad (2.4)$$

Therefore, the components of acceleration for an orbiting particle in the rotating reference frame are given by

$$\begin{aligned}\ddot{x} &= -\frac{\partial \Phi}{\partial x} + 2\Omega \dot{y} + \Omega^2 x \\ \ddot{y} &= -\frac{\partial \Phi}{\partial y} - 2\Omega \dot{x} + \Omega^2 y \\ \ddot{z} &= -\frac{\partial \Phi}{\partial z}.\end{aligned}\quad (2.5)$$

For the numerical orbit calculations, one unit of time corresponds to  $1.5 \times 10^8$  years, and one unit of distance corresponds to one core radius. However, for purposes of discussion, distances are given in units of kpc, velocities in  $\text{km s}^{-1}$ , the numerical value of the Hamiltonian ( $H$ ) in  $\text{km}^2 \text{ s}^{-2}$ , and the rotation speed of the potential ( $\Omega$ ) in  $\text{km s}^{-1} \text{ kpc}^{-1}$ . For the models discussed herein, unless otherwise indicated, one core radius equals one kiloparsec and  $v_c = 160 \text{ km s}^{-1}$ . These values are chosen to be roughly consistent with deprojected rotation curve data for both NGC 660 (Benvenuti, Capaccioli, and D'Odorico, 1976 and Gottesman and Mahon, 1990) and NGC 2685 (Schechter and Gunn, 1978; Shane, 1980; and Whitmore, Lucas, McElroy, Steiman-Cameron, Sackett, and Olling, 1990).

Of particular interest are the closed periodic orbits in a rotating triaxial potential. Each orbit is integrated for fixed time steps using a fourth order Runge-Kuta routine as described by Press et al. (1986, Chapter 15). To find the initial conditions and stability parameters for a periodic orbit, we employ the method of Magnenat (1982) and Contopoulos and Magnenat (1985), which is described below. Given initial conditions for an orbit on the  $y = 0$  plane with  $\dot{y} = \dot{y}(H) > 0$ , where  $H$  is given by Equation (2.2), and

$$(x, z, \dot{x}, \dot{z}) = (x_0, z_0, \dot{x}_0, \dot{z}_0), \quad (2.6)$$

such an orbit will intersect the  $y = 0$  plane again, with  $\dot{y} > 0$  at the point

$$(x, z, \dot{x}, \dot{z}) = (x_1, z_1, \dot{x}_1, \dot{z}_1). \quad (2.7)$$

A small change in the set of initial conditions will cause a deviation in the final point. Therefore, if one calculates an orbit for four sets of initial conditions, each with small deviations ( $\delta$ ) from the initial set given by  $(\delta, 0, 0, 0)$ ,  $(0, \delta, 0, 0)$ ,  $(0, 0, \delta, 0)$ , and  $(0, 0, 0, \delta)$ , respectively, then one can consider a linear transformation whereby, the final point can be expressed as a function,  $G$ , of the initial conditions. If, for the  $j$ th orbit, we define

$$(a_{1j}, a_{2j}, a_{3j}, a_{4j}) \equiv \left( \frac{\partial G}{\partial x_{0j}}, \frac{\partial G}{\partial y_{0j}}, \frac{\partial G}{\partial \dot{x}_{0j}}, \frac{\partial G}{\partial \dot{y}_{0j}} \right), \quad (2.8)$$

then the deviation for the  $i$ th component of the final point is given by

$$\xi_i = \sum_{j=1}^4 a_{ij} \xi_{j0}, \quad (2.9)$$

where  $\xi_{j0} \equiv \delta$ ,  $j = 1, 2, 3, 4$ . For a periodic orbit  $\xi_i = \xi_{i0}$ . However, since we are ignoring higher order terms by assuming that the transformation is linear, the solution to the system of equations given by (2.9) for  $\xi_i = \xi_{i0}$  will not give the exact initial conditions for the periodic orbit. Therefore, the process described above is repeated iteratively until the deviation from the periodic orbit has been reduced to some small designated value. If the periodic orbit is not found after ten iterations, then another set of “improved” approximate initial conditions must be found by trial and error. In the same manner, we can also consider orbits that cross the  $z = 0$  plane.

Once the set of initial conditions for a periodic orbit has been found, the linearized equations are used to find the stability parameters for the orbit (Broucke, 1969; Hadjidemetriou, 1975; and Contopoulos and Magnenat, 1985). Following Broucke (1969),

Hadjidemetriou (1975), and Contopoulos and Magnenat (1985), we seek the solutions to the characteristic equation

$$\lambda^4 + \alpha\lambda^3 + \beta\lambda^2 + \alpha\lambda + 1 = 0, \quad (2.10)$$

where

$$\alpha = -(a_{11} + a_{22} + a_{33} + a_{44}) \quad (2.11)$$

and

$$\beta = \begin{vmatrix} a_{11} & a_{12} \\ a_{21} & a_{22} \end{vmatrix} + \begin{vmatrix} a_{11} & a_{13} \\ a_{31} & a_{33} \end{vmatrix} + \begin{vmatrix} a_{11} & a_{14} \\ a_{14} & a_{44} \end{vmatrix} + \begin{vmatrix} a_{22} & a_{24} \\ a_{42} & a_{44} \end{vmatrix} + \begin{vmatrix} a_{33} & a_{34} \\ a_{43} & a_{44} \end{vmatrix}. \quad (2.12)$$

The roots of the characteristic equation are given by

$$\lambda_{ij} = \frac{1}{2} \left[ -b_i \pm (b_i^2 - 4)^{\frac{1}{2}} \right], \quad (i = 1, 2; \quad j = 1, 2), \quad (2.13)$$

where

$$b_i \equiv \frac{1}{2} (\alpha \pm \sqrt{\Delta}) \quad (2.14)$$

and

$$\Delta = \alpha^2 - 4(\beta - 2). \quad (2.15)$$

For a periodic orbit to be linearly stable, all of the characteristic roots (eigenvalues) of equation (2.10) must be complex and lie on the unit circle in the complex plane. Thus, linear stability requires that  $|b_1| < 2$ ,  $|b_2| < 2$ , and  $\Delta > 0$ . An orbit is simply unstable (*U*) in one direction, either parallel or perpendicular to its instantaneous motion, whenever either  $|b_1|$  or  $|b_2| > 2$ . Whenever both  $|b_1| > 2$  and  $|b_2| > 2$ , an orbit is doubly unstable (*D*). Such an orbit is unstable in directions both parallel and perpendicular to its instantaneous motion. Complex instability (*C*) occurs whenever  $\Delta < 0$ . In this case the eigenvalues are complex and off the unit circle.

The allowable transitions in stability type for orbits in a particular family are as follows:  $S \leftrightarrow U$ ,  $S \leftrightarrow C$ ,  $U \leftrightarrow D$ , and  $D \leftrightarrow C$  (Brouke, 1969 and Contopoulos and Magnenat,

1985). Direct transitions from S to D or from U to C cannot occur except in the very special case where  $|b_1| = |b_2| = 2$  (Contopoulos and Magnenat, 1985).

If the stability parameters for an orbit are such that  $|b_1| = |b_2| = 2$ , then a collision of bifurcations occurs. This phenomenon, first noted by Contopoulos (1986a, 1986b), is characteristic of three-dimensional Hamiltonian systems and signals the onset of many qualitative changes in the system. Whenever  $b_1 = b_2$ ,  $\Delta = 0$ , and complex unstable orbits can be produced from either stable or double unstable orbits. The corresponding eigenvalues are either complex conjugate ( $b_i^2 - 4 < 0$ ), or real ( $b_i^2 - 4 > 0$ ). However, it does not necessarily follow that there will be a region nearby in parameter space where  $\Delta < 0$ . For small changes in one of the parameters, the pairs of eigenvalues may either leave the unit circle, producing complex instability, or separate on the unit circle and preserve stability (Contopoulos and Magnenat, 1985).

#### Orbits about the Long, Rotation Axis of the Potential

The aim of the research in this section is to define some general properties of stable closed orbits in the rotating frame of a triaxial potential tumbling about its long axis. In particular, we find the simplest periodic orbits and their bifurcations, as has been done for potentials tumbling about the short axis (Heisler, Merritt, and Schwarzschild, 1982; Magnenat, 1982; and Martinet and Pfenniger, 1987). The evolution of the families of orbits as a function of tumble speed will then be investigated for two potentials of different shape. Furthermore, the possible intersections between orbits in these families will be discussed in the context of permissible equilibrium configurations for gas clouds.

Finally, the behavior of these families of orbits as a function of the shape of the potential will be explored.

### A Mildly Triaxial, Logarithmic Potential

#### The bifurcation sequence as a function of $\Omega$

An existence diagram (Contopoulos and Magnenat, 1985) for a given family of orbits can be computed for a specific potential shape by changing  $\Omega$  for many fixed values of the Hamiltonian  $H$ , and marking any transitions in stability that the family undergoes. Thus we find in the parameter space  $(H, \Omega)$  the regions of the various stability types by drawing the transition curves between them. Existence diagrams produced for triaxial potentials rotating about their short axis (Martinet and Pfenniger, 1987), show that the region of simple instability for the z-axis orbits shrinks to a point on the  $H = 0$  axis. This point gives a “critical” value of  $\Omega$  ( $\Omega_{crit}$ ). If  $\Omega > \Omega_{crit}$ , as  $H$  increases from  $H = 0$ , the z-axis family of orbits undergoes a direct transition from stability (S) to complex instability (C) for a certain value of  $H$ , which depends on  $\Omega$ . For  $\Omega < \Omega_{crit}$ , as  $H$  increases from  $H = 0$ , the z-axis family undergoes a transition from S → U. At this transition the family of anomalous orbits bifurcates from the z-axis family. Since the z-axis family gives its stability to the anomalous family, it is considered to be the parent of the anomalous family for  $\Omega < \Omega_{crit}$ . For cases where  $\Omega > \Omega_{crit}$ , as  $H$  increases, the z-axis family goes directly from S → C. The onset of complex instability prevents the z-axis family from passing its stability to the anomalous family of orbits. Instead the anomalous family obtains its stability from the retrograde family of orbits in the plane at

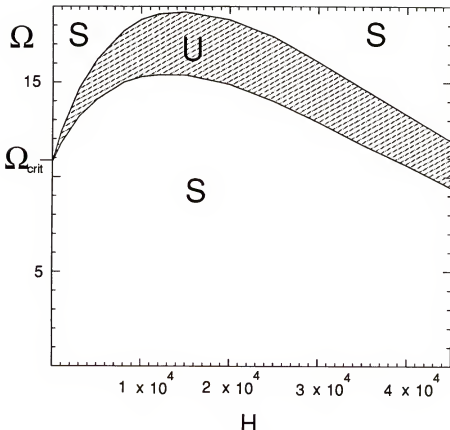


Figure 2.1: Existence diagram for the z-axis family of radial orbits in a potential with shape parameters  $(q_a, q_b, q_c) = (0.95, 0.92, 1.00)$ . The regions marked S and U are regions of stability and simple instability, respectively. For  $\Omega > \Omega_{crit}$  the prograde, SAOs bifurcate from the z-axis family at its transition from S→U.

the inner edge of the Binney instability strip where it undergoes a transition from S→U. For all values of  $\Omega$ , the anomalous family terminates at the outer edge of the Binney instability strip where the stable anomalous orbits, hereafter SAOs, pass their stability to the family of normal retrograde orbits in the equatorial plane.

This behavior is not found for the case of rotation on the long axis of the potential. Consider a nearly spherical, triaxial logarithmic potential with shape parameters  $(q_a, q_b, q_c) = (0.95, 0.92, 1.00)$ . An existence diagram in the  $(H, \Omega)$  plane computed for the z-axis family of orbits in this potential is shown in Figure 2.1. In Figure 2.1, the region of simple instability (U) shrinks to a point on the  $H = 0$  axis near  $\Omega = 10.8$ .

This value of  $\Omega$  will be referred to as  $\Omega_{crit}$ . However, for  $\Omega > \Omega_{crit}$ , as  $H$  increases from  $H = 0$ , the transition from S→C does not occur as it does in the case where the tumble axis is the short axis of the potential. Instead, for all values of  $\Omega$  studied, the transition for the z-axis family is from S→U→S as  $H$  is increased from  $H = 0$ , except for the point  $\Omega_{crit}$  where the unstable region touches the  $H = 0$  axis. Moreover, for  $\Omega < \Omega_{crit}$  these studies show that the anomalous orbits do not bifurcate from the z-axis family, but from a prograde elliptical family in the equatorial plane. Orbits in this family, referred to as  $E_p$ , are elongated in the direction of the intermediate x-axis of the potential. Above  $\Omega_{crit}$  it is the z-axis family that generates by bifurcation the anomalous orbits at its transition from S→U. The  $E_p$  family goes from S→U for low values of  $H$ , becoming stable again at very high values of  $H$ . The termination of the anomalous family at higher values of  $H$  is marked by a bifurcation of another prograde elliptical family in the equatorial plane (defined as the plane normal to the tumble axis of the potential). This family, which is elongated in the direction of the short axis of the potential, will be referred to as  $E_p-a$ .

The stability sequence described above is encapsulated in the existence diagram computed for the stable anomalous family, shown in Figure 2.2 for the potential with shape parameters  $(q_a, q_b, q_c) = (0.95, 0.92, 1.00)$ . In this diagram, below the point on the  $H = 0$  axis, referred to as  $\Omega_{crit}$ , where  $\Omega_{crit} = 10.8$ , the region from  $H = 0$  to the left border of the stable region for the SAOs is occupied by the family  $E_p$ . At this border the family of SAOs bifurcates from the  $E_p$  family, while the  $E_p$  family continues to the right (i. e., with larger energies) as unstable. Above  $\Omega_{crit}$ , the region between the  $H = 0$  axis and the border of the stable region for the SAOs is occupied by the z-axis family of radial orbits. This border marks the bifurcation of the SAO family, while the z-axis family continues to the right as unstable. The SAOs in this nearly

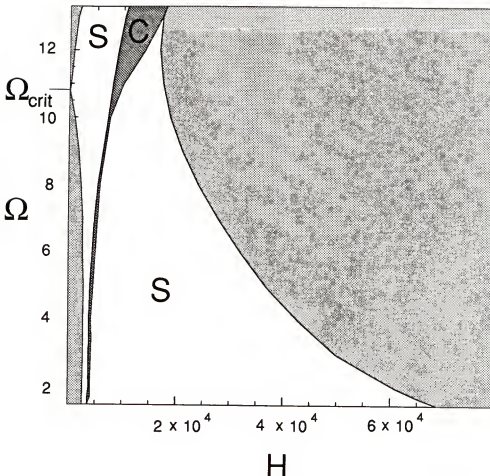


Figure 2.2: Existence diagram for the prograde, stable anomalous family of orbits in a potential with shape parameters  $(q_a, q_b, q_c) = (0.95, 0.92, 1.00)$ . The regions marked S and C are regions of stability and complex instability, respectively. As  $H$  increases from zero, for  $\Omega < \Omega_{crit}$  the prograde family of SAOs bifurcates from the  $E_p$  family of prograde elliptical orbits in the equatorial plane at its transition from S→U. For  $\Omega > \Omega_{crit}$ , the prograde family of SAOs bifurcates from the z-axis family of orbits at its transition from S→U. Near  $\Omega = 13.3$ , for increasing  $H$ , the SAOs no longer go from S→C→S before terminating at the bifurcation of the stable branch of the  $E_p$ -a family in the equatorial plane. Instead, there is a collision of bifurcations, where the stability parameters for the SAOs collide on the  $b = -2$  axis.

spherical, triaxial potential are characterized by a region of complex instability. Recall that complex instability starts whenever the stability parameters satisfy  $b_1 = b_2$ . At low tumble speeds, the complex instability strip is very narrow and occurs for very low values of the Hamiltonian  $H$ . For  $\Omega > \Omega_{crit}$  the complex instability strip becomes wider in  $H$ , and increases in width with increasing  $\Omega$ . At higher values of  $H$ , beyond

the complex instability strip, the SAO family terminates in the equatorial plane, at the transition of the  $E_p\text{-}a$  family from  $U \rightarrow S$ . Thus, the stippled region to the right of the stable region of the SAOs in Figure 2.2 is occupied by the stable family  $E_p\text{-}a$ .

Consider the stability curves for these orbits for  $\Omega = 12.0 > \Omega_{crit}$ , as shown in Figure 2.3. In this figure, as  $H$  increases from zero, the SAOs bifurcate from the  $z$ -axis family at (I). Following their bifurcation, the SAOs go from  $S \rightarrow C \rightarrow S$  before terminating in the equatorial plane at the transition of the  $E_p\text{-}a$  family from  $U \rightarrow S$ . Note the joining of the  $b_1$  stability parameters for the  $E_p\text{-}a$  and  $E_p\text{-}c$  families, on the  $b = -2$  axis, at (II) near  $H = 15,300$ . The  $b_2$  parameters join below this axis. The high  $H$  limit of the  $E_p\text{-}a$  and  $E_p\text{-}c$  families is demarcated by the joining of the  $b_2$  stability parameters for these families on the  $b = -2$  axis at (V). The SAO-b family is seen bifurcating as doubly unstable from the  $E_p\text{-}c$  family at (IV), near  $H = 32,400$ , then going from  $D \rightarrow C \rightarrow S$  before terminating at (VI) upon the transition of the  $z$ -axis family from  $U \rightarrow S$ .

Now consider the behavior of the stability parameters at the value of  $\Omega$  for which the collision of bifurcations occurs; i. e., for  $\Omega_{cl} = 13.3$ . At (II) in Figure 2.4, the  $b_1$  and  $b_2$  stability parameters for the  $E_p\text{-}a$ ,  $E_p\text{-}c$ , and SAO families collide on the  $b = -2$  axis and the family of SAOs terminates. The SAO-b family bifurcates from the  $E_p\text{-}c$  family at (IV), upon its transition from  $D \rightarrow U$ . As  $H$  increases from here, the SAO-b family goes from  $D \rightarrow C \rightarrow S$  before terminating at (VI), upon the transition of the  $z$ -axis family from  $U \rightarrow S$ . The  $E_p\text{-}a$  and  $E_p\text{-}c$  families are bounded on the left at (II) and on the right at (V) where their  $b_2$  stability curves join on the the  $b = -2$  axis.

The bifurcation sequence as described above is modified for values of  $\Omega_{c1} < \Omega < \Omega_{c2}$ , where  $\Omega_{c2}$  signals another collision of bifurcations. Within this range of  $\Omega$ , and for increasing values of  $H$ , the  $b_1$  curve for the  $E_p\text{-}c$  family crosses the  $b = -2$  axis at two points. This behavior is shown in Figure 2.5, for which  $\Omega = 13.6$ . Following their

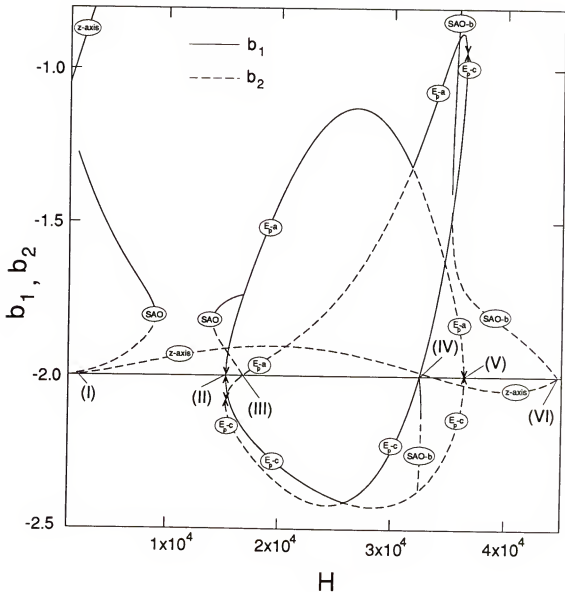


Figure 2.3: Stability curves for orbits in a potential with shape parameters  $(q_a, q_b, q_c) = (0.95, 0.92, 1.00)$  and  $\Omega = 12.0 \text{ km s}^{-1} \text{ kpc}^{-1}$ . The  $b = -2$  axis is plotted as a solid line. As  $H$  increases from zero, the SAOs bifurcate from the z-axis family at (I). For increasing  $H$ , the SAOs go from S-C-S, with the family terminating at the transition of the  $E_p$ -a family from U-S at (III). Note that the  $b_1$  parameters for the  $E_p$ -a and  $E_p$ -c families join on the  $b_1 = -2$  axis at (II), while the  $b_2$  parameters for these families join below this axis. The SAO-b family bifurcates as double unstable from the  $E_p$ -c family at (IV), and then goes from D-C-S before terminating at the transition of the z-axis family from U-S at (VI). The  $b_2$  curves for  $E_p$ -a and  $E_p$ -c are joined on the  $b_1 = -2$  axis at (V).

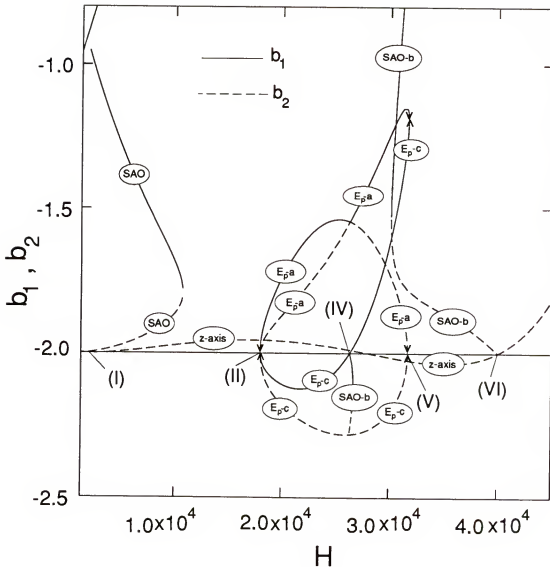


Figure 2.4: Stability curves for orbits in a potential with shape parameters  $(q_a, q_b, q_c) = (0.95, 0.92, 1.00)$  and  $\Omega = 13.3 \text{ km s}^{-1} \text{ kpc}^{-1}$ . The SAOs bifurcate from the z-axis family at its transition from S-U at (I). As  $H$  increases, the SAOs go from S-C. These orbits terminate at (II) where the stability parameters of  $E_p$ -a and  $E_p$ -c collide on the  $b = -2$  axis. SAO-b bifurcates as D at the transition of the  $E_p$ -c family from D-U (IV). Following its bifurcation, SAO-b goes from D-C-S before terminating at the transition of the z-axis family from U-S (VI). The  $b_2$  stability parameters for the  $E_p$ -a and  $E_p$ -c families are joined on the  $b = -2$  axis at (V).

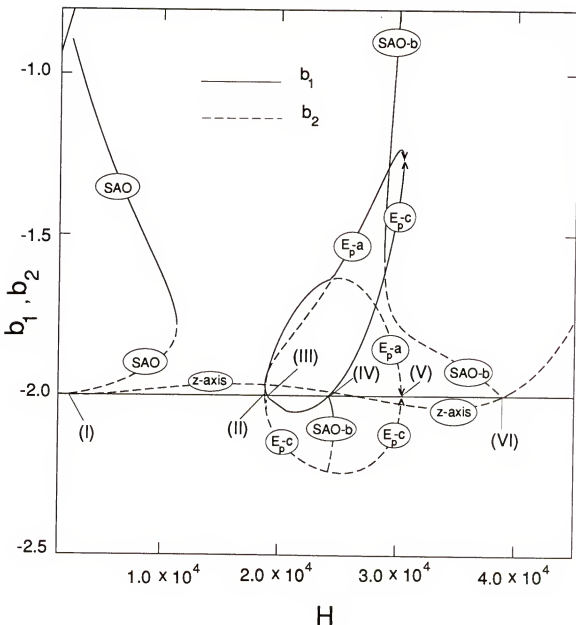


Figure 2.5: Stability curves for orbits in a potential with shape parameters  $(q_a, q_b, q_c) = (0.95, 0.92, 1.00)$  and  $\Omega = 13.6 \text{ km s}^{-1} \text{ kpc}^{-1}$ . The SAOs bifurcate from the  $z$ -axis family at its transition from  $S \rightarrow U$  at (I). As  $H$  increases, the SAOs go from  $S \rightarrow C \rightarrow D$  before terminating at the transition of the  $E_p-c$  family from  $U \rightarrow D$  at (III). SAO-b bifurcates as  $D$  at the transition of  $E_p-c$  from  $D \rightarrow U$  (IV). From (IV), the SAO-b family goes from  $D \rightarrow C \rightarrow S$  before terminating at the transition of the  $z$ -axis family from  $U \rightarrow S$  (VI). The  $b_2$  curves for the  $E_p-a$  and  $E_p-c$  families are joined on the  $b = -2$  axis at (II) and (V).

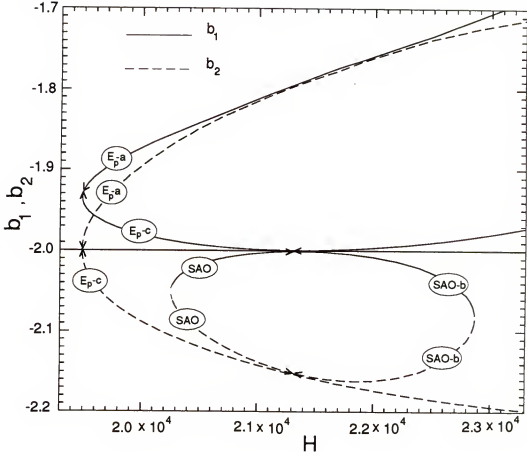


Figure 2.6: Stability curves for orbits in a potential with shape parameters  $(q_a, q_b, q_c) = (0.95, 0.92, 1.00)$  and  $\Omega = 13.79 \text{ km s}^{-1} \text{ kpc}^{-1}$ . At  $\Omega = \Omega_{c2} \simeq 13.79 \text{ km s}^{-1} \text{ kpc}^{-1}$  a collision of bifurcations occurs on the  $b = -2$  axis at the point where the  $b_1$  stability curve for the  $E_p\text{-c}$  family becomes tangent to the axis. At this point, the SAO and SAO-b families can be seen as bifurcating to the left and right, respectively. Above this value of  $\Omega$ , the SAO and SAO-b families join as one family of orbits.

bifurcation at (I) from the z-axis family, the SAOs go from S→C→D. This family terminates at (III), upon the transition of the  $E_p\text{-c}$  family from U→D, which corresponds to the first crossing of the  $b_1$  curve for the  $E_p\text{-c}$  family with the  $b = -2$  axis. For increasing  $H$ , the  $E_p\text{-c}$  family goes from D→U, at which point SAO-b family bifurcates at (IV), as doubly unstable. Following its bifurcation the SAO-b family goes from D→C→S before terminating at the transition of the z-axis family from U→S (VI). The

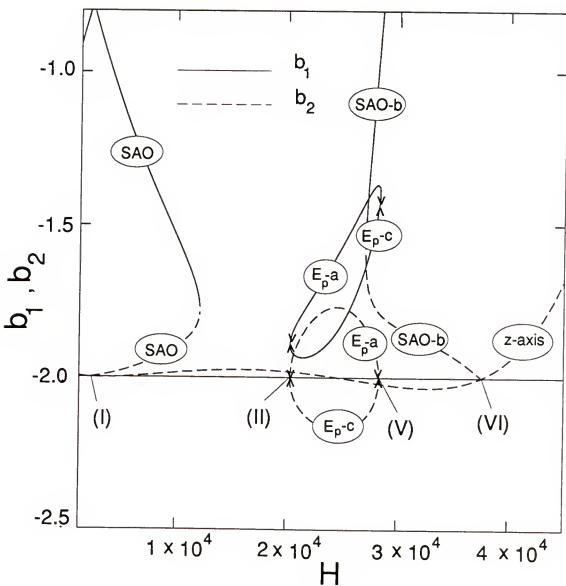


Figure 2.7: Stability curves for orbits in a potential with  $(q_a, q_b, q_c) = (0.95, 0.92, 1.00)$  and  $\Omega = 14.0 \text{ km s}^{-1} \text{ kpc}^{-1}$ . SAO and SAO-b now form one family. From (I), as  $H$  increases, the SAOs go from S-C and these orbits, which were tilting down towards the equatorial plane for increasing  $H$ , tilt back up, away from the equatorial plane before going from C-S. SAO-b terminates at the transition of the z-axis family from U-S (VI). The  $b_2$  curves for  $E_p$ -a and  $E_p$ -c join on the  $b = -2$  axis at (II) and (V).

$E_p$ -a and  $E_p$ -c families exist over the range of  $H$  between (II) and (V), where the  $b_2$  stability curves for the  $E_p$ -a and  $E_p$ -c families join on the  $b = -2$  axis.

As shown in Figure 2.6, for  $\Omega = 13.79 \simeq \Omega_{c2}$ , the  $b_1$  stability curve for the  $E_p$ -c becomes tangent to the  $b = -2$  axis. At the value of  $H$  where this occurs, the  $b_1$  parameters for the SAO and SAO-b families join on the  $b = -2$  axis, forming one orbit family for larger values of  $\Omega$ .

Now consider a value of  $\Omega$  above  $\Omega_{c2}$ . As shown in Figure 2.7, for  $\Omega = 14.0$ , orbits in SAO and SAO-b form one family, SAO. Following its bifurcation, at low  $H$ , from the z-axis family (I), the SAO family goes from S $\rightarrow$ C $\rightarrow$ S before terminating, at high  $H$ , on the z-axis family at its transition from U $\rightarrow$ S (VI). From their bifurcation at low  $H$  and for increasing  $H$ , orbits in the SAO family tilt away from the plane defined by the intermediate and long, tumble axis of the potential. The orbits no longer terminate in the equatorial plane. Instead, a minimum tilt above the equatorial plane is achieved, beyond which, for increasing  $H$ , the orbits tip back up, away from the equatorial plane, eventually terminating on the z-axis family. Thus, above  $\Omega_{c2}$ , the stable  $E_p$ -a family and unstable  $E_p$ -c family are no longer in the bifurcation sequence containing the SAOs.

#### Properties of Orbits in the Families $E_p$ , $E_p$ -a, and SAO

The stability behavior of the  $E_p$ , SAO, and  $E_p$ -a families, as a function of  $\Omega$ , is discussed in this section. In addition, possible intersections between orbits in these families are considered in the context of stable configurations that could be occupied by gas clouds.

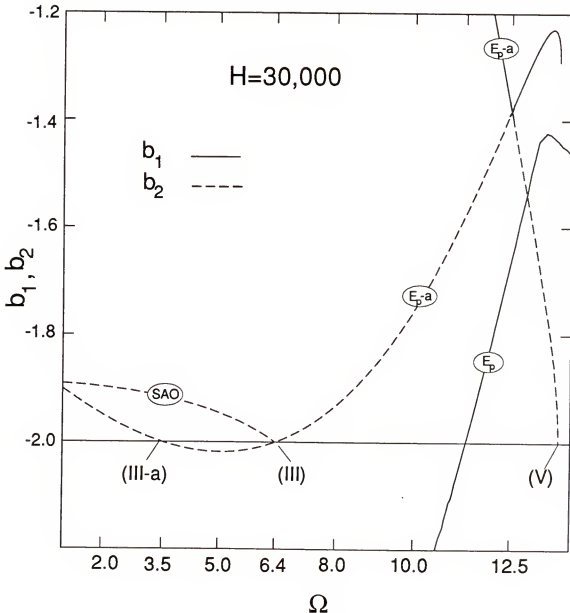


Figure 2.8: Stability curves, as a function of  $\Omega$ , for the  $E_p$ ,  $E_p$ -a, and SAO families, in a potential with  $(q_a, q_b, q_c) = (0.95, 0.92, 1.00)$  and  $H = 30,000$ . The  $b_2$  curve for the  $E_p$ -a family crosses the  $b = -2$  axis at (III-a) and (III). The  $E_p$ -a family terminates for higher  $\Omega$  at (V). Note that, for this value of  $H$ , the family  $E_p$  goes from U-S near  $\Omega = 11.3 \text{ km s}^{-1} \text{ kpc}^{-1}$ .

Consider Figure 2.8 in which the stability parameters for the families  $E_p$ ,  $E_p$ -a, and SAO are plotted against  $\Omega$  for  $H = 30,000$ . Even though the stability parameters collide near  $\Omega = 12.46$ ,  $E_p$ -a is not complex unstable for higher values of  $\Omega$ . For values of  $\Omega$  satisfying  $3.5 < \Omega < 6.5$ , Figure 2.8 shows that the  $E_p$ -a family is simply unstable.

At the transition of the  $E_p$ -a family from U $\rightarrow$ S at (III) near  $\Omega = 6.5$ , the SAO family terminates. Also indicated in this figure is the transition of the  $E_p$  family from U $\rightarrow$ S near  $\Omega = 11.3$ .

The coexistence of the  $E_p$ -a family and the SAOs at the same energy for low values of  $\Omega$  has important implications if one wants to consider gas clouds occupying stable orbits. Since, for a specific range of radii, orbits of similar energy would cross each other on the intermediate x-axis of the potential, collisions could play an important role in removing gas clouds from either the SAO or the  $E_p$ -a family. This point is considered in the following discussion centered on a model potential with  $\Omega = 2.6 < 3.5$ . For this case, the SAOs and  $E_p$ -a families are both stable at the same, low values of  $H$ .

Figure 2.9 gives the stability curves for a potential with  $(q_a, q_b, q_c) = (0.95, 0.92, 1.00)$  and  $\Omega = 2.6$ . Both the SAO and  $E_p$ -a family are stable for  $H < 39,000$ . Above this  $H$  the family of SAOs is the only stable family until its termination at (III) where the  $E_p$ -a family regains its stability. For  $39,000 < H < 54,000$  the  $E_p$ -a family is unstable, while for  $54,000 < H < 80,000$ ,  $E_p$ -a is stable. Now, consider Figure 2.10, which gives a plot of the stability curves  $x_0$  versus  $b_{1,2}$  for  $\Omega = 2.6$ . Here,  $x_0$  represents the crossing point of the orbits on the intermediate x-axis of the system, which corresponds to the direction of the minor axis of these orbits. Four intervals arise from the interplay between these families.

First, at low values of  $x_0$  up to 2.7 kpc, orbits from both SAO and  $E_p$ -a families are stable and intersect each other on the intermediate x-axis. In this interval, the orbits of the SAO family have inclinations less than  $33^\circ$  with respect to the plane containing the intermediate axis and long, tumble axis of the potential, i. e., the x-z plane.

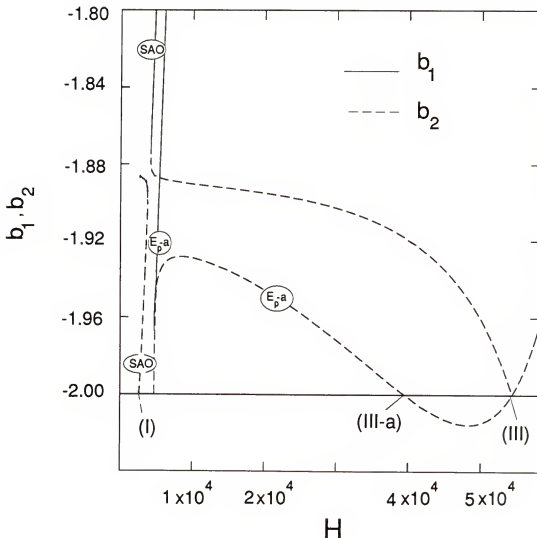


Figure 2.9: Stability curves for SAO and  $E_p$ -a families in a potential with  $(q_a, q_b, q_c) = (0.95, 0.92, 1.00)$  and  $\Omega = 2.6$ . SAO bifurcates from  $E_p$  at (I). For increasing  $H$ , SAO goes from S-C-S, terminating in the equatorial plane at (III).  $E_p$ -a goes from S-U at (III-a) and from U-S at (III), continuing for higher values of  $H$  as S.

One might expect that following the merger of a gaseous disk that has an initial angular momentum vector inclined to the pole of the primary galaxy, that gas far from a stable orbit would be subject to collisional dissipation of energy and angular momentum until it is able to assume a stable, collision-free configuration. In the inner regions of the model studied here, gas at a given energy can occupy one of two stable energy

states: one provided by the family of SAOs and the other by the  $E_p$ -a family of orbits. Therefore, the conditions leading up to the capture probably would determine which orbits would be occupied in the final equilibrium configuration.

In the second interval, for  $2.7 < x_0 < 5.0$  kpc (between (III-a) and (III) of Figure 2.10), only the anomalous orbits are stable. This annulus of SAOs covers a range of inclination with respect to the x-z plane between  $33^\circ$  and  $90^\circ$ . In the third interval,  $5.0 < x_0 < 6.4$  (between (III) and (V) of Figure 2.10), only orbits in the  $E_p$ -a family are stable. This third interval contains only those orbits in the  $E_p$ -a family that cannot be crossed by stable, higher  $H$  orbits in the same family.

Finally, in the fourth interval,  $6.4 < x_0 < 12.5$ , Figure 2.10 shows the qualitative change in the shape of the  $E_p$ -a family of orbits beyond  $x_0 = 12.56$  kpc. These orbits become very elongated in the direction of the short y-axis and very compressed in the intermediate x-axis direction for high values of  $H$ . Thus, orbits at these higher energies intersect orbits in the same family at lower energy.

Gas clouds occupying stable orbits in the  $E_p$ -a family could not persist in the fourth interval described above, if the gas was initially distributed over the entire range of  $H$  associated with this interval. It is quite likely that gas clouds in high energy orbits in the  $E_p$ -a family would collide with the lower energy orbits, lose energy and angular momentum and move inward to occupy stable orbits at lower energy and angular momentum. This scenario would ultimately lead to a depletion of clouds in the higher energy states and would increase occupation of the lower-energy states, especially in regions where the orbits do not intersect.

Now consider the same potential rotating with angular velocity  $\Omega$  near, but above  $\Omega_{\text{crit}}$  at  $\Omega = 11.0$ . Figure 2.11 shows that, as  $H$  increases from zero, the SAOs arise by bifurcation from the z-axis family at (I) when it goes from S-U near  $H \simeq 100$ .

From here, for increasing  $H$ , the SAOs go from S→C→S, where the region of complex instability is over the range  $7,950 < H < 10,150$ . Near  $H = 17,387$ , at (III) in Figure 2.11, the family of SAOs terminates at the transition of the stable  $E_p$ -a family from U→S.  $E_p$ -a continues to the right as stable. The family SAO-b arises by bifurcation as

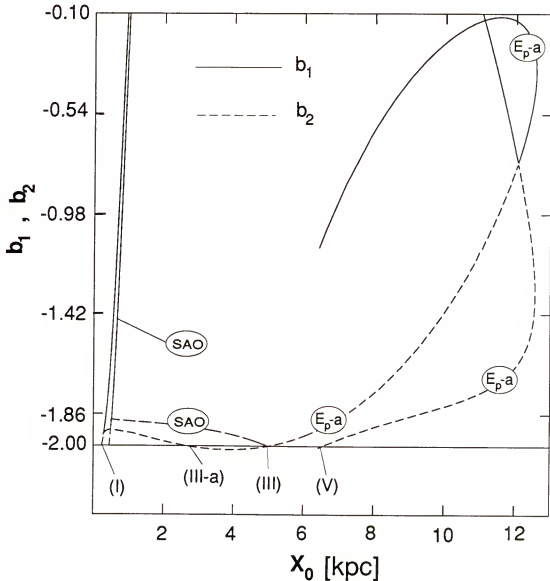


Figure 2.10: Stability curves giving  $b_{1,2}$  versus  $x_0$  for the SAO and  $E_p$ -a families in a potential with  $(q_a, q_b, q_c) = (0.95, 0.92, 1.00)$  and  $\Omega = 2.6$ , showing where the orbits cross the intermediate axis (x-axis) of the potential. SAO bifurcates as S on the left at (I) and terminates at (III) upon the transition of  $E_p$ -a from U→S.  $E_p$ -a is U between the points marked (III-a) and (III).  $E_p$ -a terminates at (V) for  $H = 80,702$ .

double unstable near  $H = 36,300$  and, for increasing  $H$ , goes from D→C→S before terminating at the transition of the z-axis family from U→S at (VI). Though not included in the diagram, the other elliptical family,  $E_p$ , goes from S→U near  $H = 1550$ , and from U→S near  $H = 31,550$ .

Now consider the interplay between the orbits in the families discussed above for  $\Omega = 11.0$ . The stability curves, over the same range in  $H$  as for Figure 2.11, are given in Figure 2.12, where  $b_1$  and  $b_2$  are plotted against  $x_0$ , the point where each orbit of a given value of  $H$  crosses the intermediate axis of the potential. There are six intervals in  $H$  that are of interest. The last five can be seen by examination of curves in Figures 2.11 and 2.12.

In the first interval, for  $H < 100$ , and deep in the core of the potential, stable branches of the z-axis and  $E_p$  families co-exist. At (I) in Figure 2.11 the z-axis family goes from S→U. The second interval, for values of  $H$  and  $x_0$  between (I) and (III) of Figures 2.11 and 2.12 is the range over which the SAOs are the only stable non-radial orbits. Figure 2.12 shows the narrow region of complex instability in the SAO family between  $0.57 < x_0 < 0.67$  kpc. Since the minor axes of orbits in this family lie in the intermediate x-axis direction, this complex unstable region corresponds to a gap in the minor axis values between the stable orbits in the family. The SAOs pass their stability to the  $E_p$ -a family once they join the equatorial plane, at which point the SAOs have reached a maximum radial extent, along the direction of the short axis of the potential, of approximately 1.25 kpc.

The third interval, defined by  $0.97 < x_0 < 2.09$  kpc (between (III) and (V) of Figure 2.12), contains the orbits of the stable family  $E_p$ -a that will not be crossed by higher energy orbits in the same family. It is important to note that the interval between (III) and (V) in Figure 2.12 excludes orbits in the  $E_p$ -a family with energies higher than

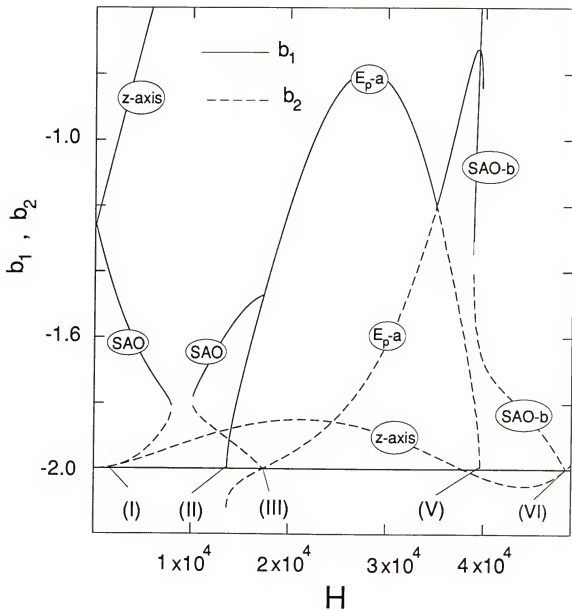


Figure 2.11: Stability diagram for a potential with  $(q_a, q_b, q_c) = (0.95, 0.92, 1.00)$  and  $\Omega = 11.0$ . Following their bifurcation from the z-axis family at (I), the SAOs go from S-C-S, terminating at (III) upon the transition of  $E_p-a$  from U-S.  $E_p-a$  exists as S over a limited range in  $H$  between (II) and (V). SAO-b arises by bifurcation as D and, to the right goes from D-C-S before terminating at the transition of the z-axis family from U-S at (VI).

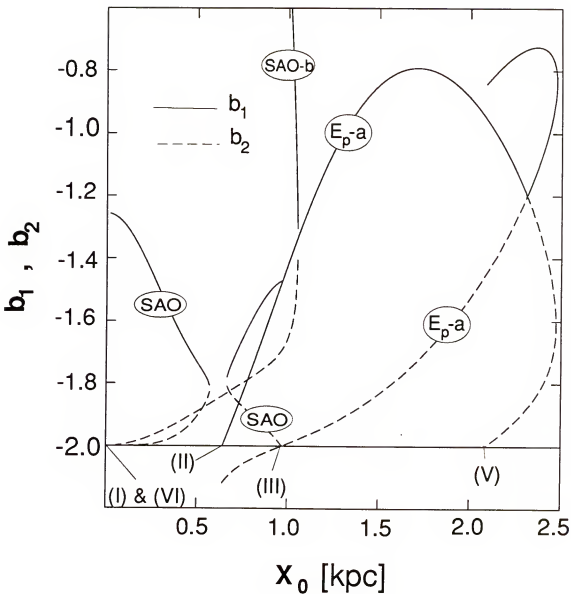


Figure 2.12: Stability curves giving  $b_{1,2}$  versus  $x_0$  for a potential with  $(q_a, q_b, q_c) = (0.95, 0.92, 1.00)$  and  $\Omega = 11.0$ . Following bifurcation from the z-axis family at (I) for low values of  $H$ , the SAOs go from S—C—S, terminating at (III) upon the transition of  $E_p$ -a from U—S.  $E_p$ -a exists as S over a limited range in  $x_0$  between (II) and (V). SAO-b arises as D by bifurcation at the transition of the family  $E_p$ -c from D—U (not shown). For increasing  $H$  and decreasing  $x_0$ , SAO-b goes from D—C—S before terminating on the z-axis at the transition of the z-axis family from U—S at (VI). Though not shown, the family  $E_p$  becomes stable at  $x_0 = 3.16$  kpc and continues to the right, for higher  $H$  and  $x_0$  as S.

$H = 37,750$ . Figure 2.12 shows how the stability curve giving  $b_{1,2}$  versus  $x_0$  for the  $E_p$ -a family changes direction beyond  $x_0 = 2.47$  kpc. Beyond this point, for  $H > 37,750$ , the semi-minor axes of orbits in the  $E_p$ -a family decrease with increasing  $H$ . The semi-minor axes of these orbits lie in the direction of the intermediate, x-axis of the potential.

In the fourth interval, for which  $2.09 < x_0 < 2.47$  kpc, higher energy orbits of the  $E_p$  family cross lower energy orbits of the same family. The  $E_p$ -a family terminates after reaching a maximum radial extent, in the direction of the short, y-axis of the potential, of about 4.1 kpc.

Though it is not shown in Figure 2.12, the fifth interval,  $2.47 < x_0 < 3.16$  kpc, defines the gap between the maximum extent of the  $E_p$ -a family and the reappearance of the stable  $E_p$  family, respectively. For increasing  $H$ ,  $E_p$  continues as stable up to at least  $x_0 = 6.27$  kpc.

Orbits of the  $E_p$  family are initially very elongated in the intermediate, x-axis direction and compressed in the short, y-axis direction; however, the degree of ellipticity of the orbits in the  $E_p$  decreases with increasing  $H$ . Over a certain energy range orbits in the  $E_p$  family will cross the orbits of the  $E_p$ -a family which have semi-major axes greater than 2.0 kpc.

#### A Nearly Prolate, Triaxial Logarithmic Potential

In order to check the generality of these results regarding the form of the bifurcation sequence as a function of  $\Omega$ , a more prolate potential was considered; i. e., one with shape parameters  $(q_a, q_b, q_c) = (0.90, 0.92, 1.00)$ . For this particular set of shape parameters, the intermediate axis of the potential corresponds to the y-axis. An existence diagram for the prograde family of stable anomalous orbits in this potential is given in Figure 2.13.

The results from this analysis are similar to those for  $(q_a, q_b, q_c) = (0.95, 0.92, 1.00)$ , as can be seen from comparison of Figures 2.2 and 2.13, except for one important point: In this case, the collision of bifurcations near  $\Omega = 15.2$  occurs at a lower value of  $\Omega$  than does  $\Omega_{crit}$ . Thus, there is clearly a connection between the shape of the potential and the value of  $\Omega$  for which such a collision of bifurcations occurs.

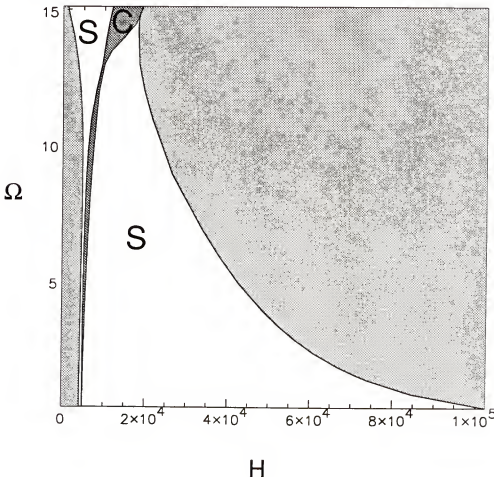


Figure 2.13: Existence diagram for the prograde family of stable anomalous orbits (SAOs) in a potential with shape parameters  $(q_a, q_b, q_c) = (0.90, 0.92, 1.00)$ . The regions marked S and C are regions of stability and complex instability, respectively. For low values of  $H$ , the left border of the stable region marks the bifurcation of the family of SAOs from the  $E_p$  family. The far right border of the stable region marks the termination of the SAO family when it joins the  $E_p$ -a family in the equatorial plane. Near  $\Omega=15.2$ , there is a collision of bifurcations for the SAO family, beyond which there is a qualitative change in the bifurcation sequence.

It is clear that for the more spherical potential,  $(q_a, q_b, q_c) = (0.95, 0.92, 1.00)$ , values for both  $\Omega_{crit}$  and  $\Omega_{c1}$  are lower than for this case. This seems to indicate that the closer a triaxial potential is to spherical, the smaller the range of  $\Omega$  over which the bifurcation sequence has the form  $E_p \rightarrow SAO \rightarrow E_p-a$ . As discussed earlier, collisions of bifurcations signal changes in the form of the bifurcation sequence containing the prograde family of inclined anomalous orbits. Therefore, if collisions of bifurcations, such as those seen in the two cases studied here, occur for lower values of  $\Omega$  the closer a triaxial potential is to spherical, then these results could have important dynamical implications for nearly spherical, triaxial systems that rotate slowly about the long axis of the potential.

### Discussion

Now consider how the planar orbits found in this study relate to the planar orbits found in studies of weak bars. First, the prograde orbits which are elongated along the intermediate axis of the potential ( $E_p$ ) appear to correspond to the central family of orbits,  $x_1$ , which is found in planar, non-axisymmetric bar potentials (Contopoulos and Grosbol, 1989). In addition, the stable and unstable families of prograde elliptical orbits, designated herein as  $E_p-a$  and  $E_p-c$ , appear to correspond to the families  $x_2$  and  $x_3$  of Contopoulos and Grosbol (1989) which exist for the case of a double inner Lindblad resonance. Stable orbits from the  $E_p-a$  family start out highly elongated to the short axis of the potential, become more circular as the energy is increased, and finally become more elongated before their termination, along with their unstable counterparts ( $E_p-c$ ), at higher energy.

For a nearly spherical potential one can invoke epicyclic theory to find the approximate locations of the classical resonances. The epicyclic approximation gives for the epicyclic frequency

$$\kappa^2 \equiv \left( \frac{d^2\Phi}{dR^2} + 3\Omega^2 \right)_{R_0}, \quad (2.16)$$

where  $\Omega$  is given by the usual equation for centrifugal equilibrium at  $R_0$ ,

$$\Omega_0^2 \equiv \Omega^2(R) = \frac{1}{R} \frac{d\Phi}{dR}, \quad (2.17)$$

and  $\Phi$  is given by Equation (2.1) (see Binney and Tremaine, 1977). Figure 2.14 gives a plot of the curves  $\Omega$ ,  $\Omega - \frac{\kappa}{2}$ ,  $\Omega + \frac{\kappa}{2}$ , and  $\Omega - \kappa$ , as computed in the potential of Equation (2.1). The inner Lindblad resonance (ILR), corresponds to the curve for  $\Omega - \frac{\kappa}{2}$ , the outer Lindblad resonance (OLR) corresponds to the curve for  $\Omega + \frac{\kappa}{2}$ , corotation corresponds to the curve labeled  $\Omega$ , and the 1:1 resonance corresponds to the curve  $\Omega - \kappa$ . Note the existence of two inner Lindblad resonances for low values of the tumble speed.

The principal results of this numerical study of inclined orbits in long axis rotators concern the form of the bifurcation sequence containing the prograde anomalous family of orbits as a function of the potential's rotation rate. Here, the stability of the following five orbit families has been considered as a function of the tumble speed of the potential for two different sets of shape parameters: i) the z-axis family of radial orbits, where the z-axis is the long, rotation axis of the potential; ii) the  $E_p$  family of elliptical orbits in the equatorial plane which are elongated in the direction of the intermediate axis of the potential; iii) the  $E_p$ -a family of orbits which are elongated along the direction of the short axis of the potential; iv) the inclined prograde family of anomalous orbits SAO; and v) a high energy branch of the inclined anomalous orbits, the family SAO-b. In nearly spherical, triaxial potentials that rotate slowly about the long axis, the main

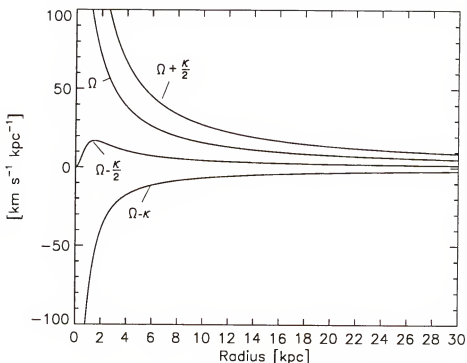


Figure 2.14: Locations of the classical resonances in a logarithmic potential.

families of interest are the families  $E_p$ , SAO, and  $E_p-a$ . Above certain critical values of the rotation rate, collisions of bifurcations occur, and the connections between the various families of orbits change; i. e., the bifurcation sequence undergoes qualitative changes. The value of  $\Omega$  at which these changes occur depends critically on the shape of the potential. From the study here, though limited to two specific cases, it appears that collisions of bifurcations occur for lower values of  $\Omega$  the closer a potential is to spherical. The results presented in this chapter may have important dynamical implications for long axis rotators, such as certain elliptical galaxies, as well as for some polar ring systems.

## CHAPTER 3

### HI OBSERVATIONS WITH THE VLA RADIO TELESCOPE

#### Review of Aperture Synthesis with the VLA

The Very Large Array (VLA) is a radio synthesis telescope constructed from 27 parabolic reflector dishes, each 25 meters in diameter. The dishes are arranged in a three armed configuration, with each arm separated by an angle of  $120^\circ$ , and with the North arm of the array oriented  $5^\circ$  East of North to avoid the occurrence of exact East-West baselines on the two southern arms (Thompson, 1989). The spacing between the antennas is given by a power law, whereby the distance of the nth antenna, on any one arm, from the center of the array is proportional to  $n^{1.716}$ , a design that allows for no two equal antenna spacings on any arm (Thompson, 1989).

Observations with a synthesis telescope like the VLA involve measurement of the spatial autocorrelation function ( $V$ ) of the electric field ( $E$ ). Following Clark (1989), a relation between  $V$  and the intensity of the radiation ( $I$ ) can be obtained if one assumes both that the radiation from astronomical sources is not spatially coherent, and that the source is very far away. Thus, if  $\nu$  is the frequency of the radiation received by the antennae;  $\vec{r}_1$  and  $\vec{r}_2$  the positions of the antennae in the array;  $\vec{s} = \vec{s}_0 + \vec{\sigma}$ , a unit vector giving the direction to a position on an extended source relative to the phase tracking center  $\vec{s}_0$ ; and  $d\Omega$  the incremental solid angle on the plane of the sky, then

$$\begin{aligned} V_\nu(\vec{r}_1, \vec{r}_2) &= \langle E_\nu(\vec{r}_1) E_\nu^*(\vec{r}_2) \rangle \\ &\approx \int I_\nu(\vec{s}) e^{-2\pi i \nu \cdot (\vec{r}_1 - \vec{r}_2)/c} d\Omega. \end{aligned} \quad (3.1)$$

Now consider two coordinate systems: one on the plane of the sky, as defined by the endpoints of the vectors  $\vec{s}$ , with components  $(l, m, 0)$ ; and the other defined in terms of the antenna separation (baseline) vectors  $(\vec{r}_j - \vec{r}_k) \equiv \vec{B}_{jk}$ , with components  $(u, v, w)$  which are measured in units of the observing wavelength. In terms of these two coordinate systems, Equation (3.1) takes the form

$$V_\nu(u, v) = e^{-2\pi i w} \int \int I(l, m) e^{-2\pi i (ul + vm)} dl dm. \quad (3.2)$$

If the factor in front of the integrals is absorbed into the left hand side of the equation, so that the right hand side of the equation will be independent of  $w$ , then one obtains the spatial autocorrelation function relative to the phase tracking center,

$$V_\nu(u, v, w) = V_\nu(u, v) e^{2\pi i w}. \quad (3.3)$$

The intensity of the radiation field can now be directly obtained from measurements of the spatial autocorrelation function since the expression for  $V(u, v, w)$  is a Fourier transform, an equation that can be directly inverted. Thus,

$$I_v(l, m) = \int \int V_\nu(u, v) e^{2\pi i (ul + vm)} du dv. \quad (3.4)$$

In practice, there are only a finite number of spacings, or points in the  $uv$  plane, that are sampled during a given observing run; thus,  $V$  is modified by the sampling function,  $S(u, v)$ , which represents the coverage of the  $uv$  plane. Given that  $S(u, v)$  is a delta function, the observed intensity, or “dirty image”, is given by

$$I_\nu^D(l, m) = \int \int V_\nu(u, v) S(u, v) e^{2\pi i (ul + vm)} du dv, \quad (3.5)$$

where the synthesized beam, or point spread function, is given by

$$B(l, m) = \int \int S(u, v) e^{2\pi i(ul+vm)} du dv. \quad (3.6)$$

It follows from the convolution theorem that  $I_\nu^D(l, m)$  is the convolution of the “true” intensity distribution with the synthesized beam, or

$$I_\nu^D = I_\nu * B. \quad (3.7)$$

Therefore, the “true” intensity distribution can be obtained by deconvolution.

The deconvolution algorithm for removing the effects of the sidelobes of the dirty beam from VLA observations, “CLEAN”, was devised by Högbom (1974) and modified by Clark (1980). This will be discussed further in Section 2. For more information on this and other deconvolution algorithms see Cornwell and Braun (1989).

In order to understand how the complex visibilities are measured and calibrated, one must first consider what happens to a signal coming from the correlator of a single interferometer pair. A monochromatic signal received by each element of this pair is proportional to  $\cos(\omega t)$  and  $\cos(\omega t + \tau)$ , where

$$\tau = \frac{\vec{B} \cdot \vec{s}_0}{c}. \quad (3.8)$$

Following detection and amplification these signals are run through a multiplier which gives

$$R(t) \propto \cos(2\omega t - \tau) + \cos(\omega \tau), \quad (3.9)$$

and then through a low pass filter which gives

$$R(t) \propto \cos(\omega \tau). \quad (3.10)$$

The VLA receivers are not monochromatic, however, but admit a range of frequencies over a particular bandwidth,  $\Delta\omega$ . Thus  $\tau$  corresponds to a different number of wavelengths for each frequency in the band. Integration over all of these frequencies in the multiplier results in a loss of coherence across the band, and therefore reduces the amplitude of the signal. In order to improve the coherence over the band and thereby maximize the correlator output, the VLA implements delay tracking. Delay tracking involves introduction of a time delay,  $\tau'$ , into the propagation path that almost cancels the delay at band center,  $\tau$ . In order to obtain satisfactory coherence over the frequency band, the following condition must hold:

$$|\tau - \tau'| \ll \frac{2\pi}{w}. \quad (3.11)$$

In practice, the received signals are reduced to an intermediate frequency before multiplication and delay tracking. This is accomplished by mixing each signal with the signal of a local oscillator (LO) of frequency  $\omega_{lo}$ , creating two sidebands, one of which is selected by appropriate filtering. The output from the correlator is thus given by

$$R(t) \propto \cos[\omega_{lo}\tau + \phi(t)], \quad (3.12)$$

where  $\phi(t)$  represents the difference in phase between signals received at the two mixers (Hjellming and Basart, 1982). The VLA employs LO's at each antenna controlled by a synchronized master LO. Delay tracking for the VLA is implemented for all antennas in the array relative to a single point in the array. Such an implementation requires that the positions of all the antennas are accurately known.

Delay tracking is only accurate for a signal arriving from direction  $\vec{s}_0$ ; therefore, a signal arriving from direction  $\vec{s}$  will produce, as output from the correlator,

$$R_{jk}(t) = A_j(t)A_k(t) \cos\left[\frac{\omega_{lo}\vec{B} \cdot (\vec{s} - \vec{s}_0)}{c} + \phi_j(t) + \phi_k(t)\right], \quad (3.13)$$

where the  $A$ 's are instrumental amplitudes, and the  $\phi$ 's are the instantaneous phases of each antenna with respect to the master LO (including the phase shift associated with the delay tracking). The correlator output, expressed in terms of the complex visibility function is given by

$$V_{jk} = A_{jk}(t) \exp \left\{ i \left( \frac{\omega_{lo} \vec{B} \cdot (\vec{s} - \vec{s}_0)}{c} \right) + i \phi_{jk} \right\}, \quad (3.14)$$

where

$$A_{jk}(t) = A_j(t)A_k(t) \quad (3.15)$$

and

$$\phi_{jk}(t) = \phi_j(t) - \phi_k(t). \quad (3.16)$$

In order to calibrate the instrumental amplitudes and phases a strong point source is desired as the calibrator. For the case of a point source, Equation (3.14) takes the simple form

$$V_{jk}(t) = A_{jk}(t) \exp \{ i \phi_{jk}(t) \}. \quad (3.17)$$

Now  $V_{jk}(t)$  can be written as the product of the complex gains ( $G_j(t)$  and  $G_k^*(t)$ ) and the true flux ( $S$ ) of the calibrator source; i. e.,

$$V_{jk}(t) = G_j(t)G_k^*(t)S = G_{jk}(t)S. \quad (3.18)$$

From Equations (3.17) and (3.18), the calibration equations for each of the  $N(N - 1)/2$  baselines are given by

$$G_{jk}(t) = \frac{A_{jk} \exp(i \phi_{jk}(t))}{S}. \quad (3.19)$$

The amplitudes and phases are determined from linear least square solutions from which the residuals of  $A_j(t)$  and  $\phi_j(t)$  are called the closure errors in amplitude and phase for

the  $j$ th antenna. Calibrators should be observed with enough frequency during a given run so that the time dependence of the complex gains of the antennas can be ascertained. The values obtained for the calibrators can then be interpolated across the observing run in order to obtain the approximate gains for the program object.

Spectral line observations with the VLA require additional voltage multipliers which are employed to calculate the correlation as a function of lag  $\tau$ , which is essentially a phase shift; i. e.,

$$V(u, v, \tau) = \int V(u, v, \nu) e^{2\pi i \tau \nu} d\nu. \quad (3.20)$$

The inversion of this Fourier transform gives, in terms of sampled data,

$$V(u, v, j\Delta\nu) = \sum_k V(u, v, k\Delta\tau) e^{-2\pi i j k \Delta\nu \Delta\tau}. \quad (3.21)$$

Therefore, to avoid loss of information in the sampling process, the frequency bandwidth must be less than the replication interval of  $1/\Delta\tau$ .

Finally, the modification of  $V_\nu(u, v, w)$  due to the response of the array must be considered. If the antenna reception pattern for the array is given by  $A(\sigma)$ , where  $A_0$  is the response at beam center, then the expression for the complex visibility of the source takes the form

$$V \equiv |V| e^{i\phi_V} = \int \frac{A(\vec{\sigma})}{A_0} I_\nu(\vec{\sigma}) e^{-2\pi i \vec{B} \cdot \vec{\sigma}/c} d\Omega \quad (3.22)$$

(Thompson, 1989).

### Mapping of VLA Data

Maps of the spatial distribution of the observed radiation field are constructed by Fourier inversion of the visibility data. This inversion is accomplished using Fast

Fourier Transform (FFT) techniques. Such techniques require that the data be weighted and gridded into a rectangular matrix. Following Sramek and Schwab (1989), these techniques are summarized below. There are two types of weighting: density weighting and tapering. Density weighting can be of two types, either natural or uniform. Natural density weighting implies that all visibilities are weighted equally; i. e., the weight is proportional to the number of visibility points in a given grid cell. Since the VLA gives a high concentration of points in the inner region of the *uv* plane natural weighting gives higher weight to lower spatial frequencies, thus giving the best signal to noise ratio if one wishes to observe weak sources. On the other hand, uniform weighting gives equal weight to each grid cell, effectively downweighting low spatial frequencies and thereby lessening the sidelobes caused by gaps in the *uv* coverage. For cases where uniform weighting is employed, the shape of the beam can be controlled by another type of weighting, the taper. Tapering involves multiplication of the weights of all points by a function which decreases with increasing distance from the center of the *uv* plane, thus giving higher weight to lower spatial frequencies. Even though tapering acts to suppress small scale sidelobes by reducing the importance of low density points in the outer part of the *uv* plane, it also increases the beamwidth. Thus, whenever a taper is employed one must weigh carefully the benefits of increasing sensitivity at the expense of spatial resolution of the observations. If a taper is deemed necessary, then a gaussian taper is usually chosen.

Gridding of the data is accomplished by convolving the weighted, sampled distribution with a specified function, and then sampling the results of this convolution at the center of each cell of the grid. The FFT can then be computed from the resulting matrix of values. The convolving function should be chosen in such a way that its Fourier

transform is flat over a small region, beyond which it falls off rapidly. Otherwise, parts of the sky brightness that lie outside the region over which the image is computed may be aliased back into the image. Furthermore, any authentic feature in the image will produce sidelobes that will extend outside of the image, and these sidelobes may also be folded back into the image thus raising the background noise. Therefore, in the maps constructed herein, a truncated, spheroidal convolving function is chosen in order to minimize the effects of aliasing.

One also must choose an appropriate cell size  $\Delta u$  for the gridding. This cell size is related to the cellsize of the desired maps  $\Delta x$  (in radians) by  $\Delta u \Delta x = 1/m$ , where  $m$  is number of cells on one side of the gridded matrix. For adequate sampling, the half power width of the synthesized beam in the final VLA maps should span at least two map cells.

By following the procedure describe above, one ends up with an image in the map plane, which will be referred to as the "dirty" image, as well as a "dirty" beam, Equations (3.5) and (3.6). These maps will most likely be contaminated by the sidelobes of the dirty beam. If no sidelobes are apparent, then the next step is unnecessary. Sidelobes occur as a result of the finite extent of and gaps in the  $uv$  coverage. The FFT assigns a zero-brightness to all empty cells in the  $uv$  plane, providing an unrealistic estimate of the source brightness at unsampled spatial frequencies. As mentioned earlier, the effects of the sidelobes can be removed by employing an appropriate deconvolution algorithm: such as the CLEAN algorithm.

Essentially, the CLEAN algorithm attempts to interpolate missing samples in the  $uv$  plane. CLEAN works iteratively, seeking the brightest point in the map, subtracting some fraction of that peak times the entire map of the dirty beam from that point in the map, and repeating until the remaining emission has reached the specified noise level of the map. The flux subtracted at the position of the peak is stored as a "CLEAN

component". It is usually best to restrict the range of data in which CLEAN looks for peaks by defining regions containing the emission with rectangular boxes. A variation of this algorithm, the form developed by B. G. Clark (1980), is employed at the VLA in the Astronomical Image Processing Software (AIPS).

In the AIPS version, the CLEAN components are found by cleaning the brightest points in the residual map with a small area of the dirty beam, rather than the entire beam. Then, more exact cleaning is effected by taking the transform of the CLEAN components, multiplying this by the transform of the dirty beam, and then transforming the product back to the map plane. The result is then subtracted from the dirty map. Finally, a cleaned map is constructed from the accumulated clean components by convolving of this set of discrete intensity spikes with a "synthesized beam". The "synthesized beam" is simply an elliptical gaussian function fit to the innermost portions of the dirty beam. The resolution of the final map is given by the half power beamwidth of the synthesized beam. In the following sections, such CLEAN maps will form the basis for the analysis of the neutral hydrogen distribution in NGC 2685 and NGC 660.

---

#### NGC 2685 and its Dwarf Companion, MCG+10-13-030

---

#### Literature Review on the Galaxy NGC 2685

In the photograph of NGC 2685 given in Figure 3.1, three components of this unusual system can be distinguished: an elongated central body, a filamentary structure that appears to be wrapped around the central body, and a diffuse outer ring aligned roughly with the long axis of the central body. Rotation curves derived from stellar absorption spectra taken along the apparent major axis of the central galaxy show a

Figure 3.1: The “spindle” galaxy NGC 2685, from a print in the Atlas of Peculiar Galaxies. North is at the top, West is to the left of North, and East is to the right. The image was obtained by A. R. Sandage with the 200" telescope on Palomar mountain from a 30 minute exposure using a 103a-O emulsion. © 1966, Atlas of Peculiar Galaxies.



linear rise in rotation velocity to about  $115 \text{ km s}^{-1}$  at  $10''$  from the nucleus (Schechter and Gunn, 1978). Beyond this point there is a clear departure from solid body rotation, with the rotation curve turning over and continuing, as nearly level, out to  $34''$  from the nucleus (Whitmore, Lucas, McElroy, Steiman-Cameron, Sackett, and Olling, 1990). From these observations, Whitmore et al. (1990) derive a maximum rotational velocity for the rotation curve of roughly  $120 \text{ km s}^{-1}$ . This maximum rotation velocity is twice the central stellar velocity dispersion of  $60 \text{ km s}^{-1}$ , a result that is consistent with the interpretation that the central stellar component is a rotationally supported disk (Whitmore et al., 1990). Moreover, stellar spectra taken along the minor axis of the central galaxy indicate some small, but non-negligible rotation about the minor axis of the central galaxy (Schechter and Gunn, 1978).

Emission line observations along the minor axis of the central galaxy indicate rotation of gas in the inner filamentary structure wrapped around the long axis of the central galaxy (Ulrich, 1975; Schechter and Gunn, 1978). Furthermore, these spectra indicate that the gas within  $10''$  of the nucleus is rotating in the same sense as the filamentary structure (Ulrich, 1975). The observed emission lines seem to be direct evidence for gas being fed into the galactic nucleus.

A luminosity profile, derived from photometric observations of the central galaxy shows an inner bulge and an extended exponential region, results that are consistent with the interpretation that this is a disk system (Whitmore et al., 1990). While the main body of the central galaxy is relatively constant in color, profiles for the polar ring and filamentary material indicate that these components are bluer than the central galaxy by about 0.2 magnitudes (Whitmore et al., 1990).

Shane (1980) obtained 21-cm observations of NGC 2685 with the Westerbork Radio Synthesis Telescope (WRST). These observations have an r.m.s. sensitivity of 4.2

mJy/Beam, a synthesized HPBW of  $49'' \times 57''$ , and a spectral resolution of  $27 \text{ km s}^{-1}$ . HI maps derived from the data reveal that roughly 75% of the HI in the galaxy is associated with the outer ring structure, and that the rotation of the ring is in the same sense as the central galaxy. The orbital plane of the outer ring appears to be inclined ( $15^\circ$ – $30^\circ$ ) to the fundamental plane of the stellar disk. The remaining gas appears to be associated with the filamentary component and indicates rotation around the projected major axis of the central galaxy. Aside from the gas in the structures about the central galaxy, no gas appears to be associated with the central galaxy.

Toomre (1977) suggested that the simultaneous presence of two independent gas systems in addition to the central stellar mass concentration may be the result of two separate accretion events involving the capture of intergalactic gas clouds of gas rich dwarfs. In this scenario, the inner filamentary structure could result from infall along

Table 3.1: Optical characteristics of the galaxy NGC 2685.

Optical Characteristics of NGC 2685	
Right Ascension <sup>a</sup>	$08^{\text{h}} 51^{\text{m}}.67$
Declination <sup>a</sup>	$58^\circ 55.5$
Type <sup>b</sup>	SOB P
Diameter at 25 mag arcsec <sup>-2</sup> blue isophote [arcmin] <sup>c</sup>	5.1
Axial ratio <sup>b</sup>	0.55
Inclination <sup>b</sup>	$62^\circ$
$m_B$ <sup>b</sup>	11.75
$V_{\text{Helio}}$ [ $\text{km s}^{-1}$ ] <sup>b</sup>	877
$V_0$ adjusted for $300 \text{ km s}^{-1}$ toward $(l, b)=(90^\circ, 0^\circ)$ <sup>b</sup>	965
$M_B$ <sup>b</sup>	-19.30

<sup>a</sup> (de Vaucouleurs, de Vaucouleurs, and Corwin, 1976)

<sup>b</sup> (Tully, 1988)

<sup>c</sup> (Nilson, 1973)

the rotation axis of the central galaxy. Observations with higher spatial and spectral resolution, like those presented here for neutral hydrogen, may serve to improve our understanding of the peculiar morphology of this galaxy. Table 3.1 summarizes some of the important optical characteristics of NGC 2685.

In the HI observations discussed below, emission was detected from at least one, and maybe two or three nearby dwarf companion galaxies. The brightest of these in HI is MCG+10-13-030; however, there does not appear to be much information available on this galaxy, other than its position. There appears to be a weak detection of emission from the galaxy UGC 4683, as well as from another, yet unidentified, system.

### VLA HI Observations

#### The observing runs for NGC 2685

NGC 2685 was observed with the mixed B/C Array configuration on July 29, 1989 and the D Array configuration on January 20, 1990. Twenty-six antennae were employed at one time during the eight hour observing run with the D array configuration, while 27 antennae were employed for the eight hour run with the B/C array configuration. The autocorrelation normalization option (AUT) was taken for the B/C array observations, while the bandpass normalization option (B) was taken for the D array observations. Both sets of observations were made using a total bandwidth of 6.25 MHz centered on 1416.313 MHz. The observations were conducted in the 2AD mode (right and left polarization) which employs two intermediate frequencies (IF) with 64 channels per IF. To avoid the drop in sensitivity at the edge of the bandpass, only the central 32 channels were retained for mapping. Channel centers are separated by 97.656 kHz and the spectral

Table 3.2: VLA observing parameters for NGC 2685.

Parameters	NGC 2685	
Array	B/C	D
Total Number of Antennas	27	26
Observing dates	89 Jul 29	90 Jan 20
Duration of Observations [hr]	8	8
Velocity of band center, heliocentric [km s <sup>-1</sup> ]	870	870
Observing Mode	2AD	2AD
On-line Hanning Smoothing	no	no
Full Width Half Power of primary beam [']	32	32
Flux of Primary Calibrator 3C286 [Jy]	14.75	
Flux of Secondary Calibrator 0831+557 [Jy]	8.347	8.058
Phase Calibrator	0831+557	
Min. projected spacing [kλ]	.138	
Max. projected spacing [kλ]	17.594	
Field Center RA [1950]	08 <sup>h</sup> 51 <sup>m</sup> 41 <sup>s</sup> .2	
Field Center DEC [1950]	58° 55' 30.00"	
Total Observing Bandwidth [MHz]	6.25	
Bandcenter [MHz]	1416.31	
Number of velocity channels	31	
Channel Separation [km s <sup>-1</sup> ]	20.73	
Channel Separation [kHz]	97.656	
Channel velocity Resolution [km s <sup>-1</sup> ]	24.876	
Total Visibilities in Combined Data Set	245608	

resolution of the observations is given by the frequency half width of the synthesized sinc function (1.2 times the channel separation) (Rots, 1988). The actual time spent observing NGC 2685 with the B/C array was 5.98 hours. For the D array observations, 6.33 hours were actually spent on NGC 2685. Thus, the combined array observations give a total of 11.98 hours of data on the galaxy. Since the HI emission is assumed to be unpolarized, the visibilities obtained for both R and L polarizations were averaged following calibration of the observed visibilities, effectively reducing the expected noise in the maps by a factor of  $\frac{1}{\sqrt{2}}$ . The observational parameters for this run are summarized in Table 3.2.

#### Calibration and editing of the visibilities

The visibilities for each IF were calibrated and edited separately. The flux and bandpass calibrators were 3C286 and 0831+557, while the phase calibrator was 0831+557. The flux and phase calibrator 0831+557 was observed for four minutes following each 40 minute scan of NGC 2685. The calibrator 3C286 (1328+307), a VLA standard, was observed once for seven minutes in the middle of the D array run, and for a total of twelve minutes from two scans in the C array run. The time dependent amplitudes and phases were calibrated using data from channel zero, which is formed from the central 75% of the 6.25 MHz bandpass.

A least squares, antenna-based solution for the complex gains of each antenna was obtained from the average of the calibrator visibilities over each scan. A few baselines in each data set had visibilities that deviated from the antenna-based solution by more than 5% in amplitude or 5° in phase. These were flagged and new antenna-based solutions were found for the complex gains.

The flux of 0831+557, obtained by bootstrapping to 3C286, was 8.058 Jy and 8.347 Jy, from the D and B/C observations, respectively. Fluxes were then computed for the entire dataset using two-hour box car averaging of the amplitude and phase gains of the individual antennae between consecutive antenna solutions. The bandpass calibrator 3C286, was assumed to have a flat spectrum over the total spectral-line bandwidth. For each base line, the spectra were individually normalized by channel zero and vector averaged over the calibrator. The visibilities in the data-base were then corrected by dividing by the values computed above. Following calibration, the source visibilities were examined for time dependent errors and the bad data were flagged. The IF's for each data-set were averaged prior to combining the datasets. In the combined UV data set of 245,608 visibilities, the minimum and maximum projected baselines are 0.138 k $\lambda$  and 17.594 k $\lambda$ , respectively.

#### Distribution of HI in NGC 2685 and MCG+10-13-030

Since the best estimate of the total HI mass in NGC 2685 is desired, and since natural weighting provides the highest signal to noise ratio, thirty-one naturally weighted 512  $\times$  512 channel maps with 9"  $\times$  9" cells were derived from the visibilities. The HPBW of the synthesized beam, for the naturally weighted maps is 34".33  $\times$  33".63, and the beam position angle is 82°.95.

The highest possible resolution is also desired in order to study the distribution of gas in the inner polar ring component of NGC 2685. Therefore, thirty-one 256  $\times$  256 channel maps with 5"  $\times$  5" cells were produced using uniform weighting of the visibilities and a 17 k $\lambda$  taper. The resolution of the uniformly weighted maps is 11".46  $\times$  9".99, and the position angle of the synthesized beam is 52°.33. Table 3.3 summarizes

Table 3.3: HI map parameters for NGC 2685.

Final Maps	NGC 2685
HPBW of Synthesized Beam for Maps with Uniform Weighting ["]	11.46 × 9.99
Beam Position Angle [°]	52.33
Visibility Taper [ $k\lambda$ ]	17
Map Dimensions [cells]	256 × 256
Pixel Dimensions ["]	5 × 5
RMS Noise in Channel Maps [mJy/Beam]	0.56
Equivalent $T_B$ [°K]	2.98
HPBW of Synthesized Beam for Maps with Natural Weighting ["]	34.33 × 33.63
Beam Position Angle [°]	82.95
Map Dimensions [cells]	512 × 512
Pixel Dimensions ["]	9 × 9
RMS Noise in Channel Maps [mJy/Beam]	0.32
Equivalent $T_B$ [°K]	1.70

the principal map parameters for the maps made with uniform weighting, as well as those made with natural weighting of the visibilities.

Each map was examined for line-emission and ten line-free channels, 1-5 and 27-31, were averaged to form both natural and uniformly weighted continuum maps. Each continuum map was subtracted from the respectively weighted channel maps to form continuum-free maps of the HI emission. The expected r.m.s. noise level ( $\sigma$ ) on the uniformly weighted maps can be expressed as follows:

$$\sigma = \frac{620}{\sqrt{n(n-1)\tau p \Delta\nu}}, \quad (3.23)$$

where  $n$  is the number of antennae involved,  $\tau$  the integration time (in hours), and  $\Delta\nu$  the bandwidth (in kHz) (Rots, 1988). If one wishes to average independent measurements made at opposite polarizations then  $p=2$ , otherwise  $p=1$ . Using the channel bandwidth of 97.656 kHz, an integration time of 11.98 hours, two polarizations, and 26

Table 3.4: Noise statistics on HI channel maps of NGC 2685.

Noise Statistics on Continuum Subtracted Line-Free Maps		
	Naturally Weighted Maps	Uniformly Weighted Maps
ch	r.m.s noise [mJy/Beam]	r.m.s noise [mJy/Beam]
1	0.33056	0.56749
2	0.31058	0.54949
3	0.31973	0.53743
4	0.31406	0.55104
5	0.30863	0.55441
27	0.33197	0.55994
28	0.30778	0.56912
29	0.32991	0.56208
30	0.32815	0.57411
31	0.33619	0.58014
Average	0.32176	0.560525

antennae, the expected r.m.s. noise is 0.50 mJy/Beam. This value is in good agreement with the average r.m.s. noise computed for the uniformly weighted channel maps of 0.56 mJy/Beam. The r.m.s. noise in the line free channels following the continuum subtraction, for both natural and uniformly weighted maps, is given in Table 3.4.

The continuum maps, as constructed above, were not suitable for the purpose of determining the presence of weak continuum emission associated with the galaxy. This was due to confusing sidelobes produced by sources at the edge of the  $512 \times 512$  map. Thus, a very large naturally weighted continuum map ( $1024 \times 1024$  with  $9'' \times 9''$  cells) was made from a pseudo continuum channel computed by averaging the visibilities in channels 1–5 and 27–31 using the AIPS task avspc. The r.m.s. noise ( $\sigma$ ) on this map, in regions free of sidelobes, is 0.37 mJy/Beam. The sidelobes were removed from the maps by cleaning down to the 0.86 mJy/Beam level of the map, using the deconvolution algorithm, CLEAN.

Table 3.5: Continuum sources in the NGC 2685 maps.

Source	Continuum Sources in the NGC 2685 Field			
	Right Ascension (1950.0)	Declination (1950)	Peak Intensity [mJy/Bm]	Integral Intensity [mJy]
1	08 49 35.188	59 05 58.80	7.460	9.323
2	08 49 41.397	59 00 31.76	5.445	7.996
3	08 50 14.354	58 57 21.37	2.669	3.531
4	08 50 32.761	58 52 18.27	3.773	4.200
5	08 50 38.003	59 08 1.01	2.197	4.623
6	08 51 42.273	59 07 14.90	2.117	2.765
7	08 52 15.668	58 59 16.39	3.138	6.872
8	08 52 36.047	59 07 13.92	9.982	13.863
9	08 53 06.171	58 47 01.55	6.840	7.715
10	08 53 07.751	58 55 29.09	2.222	3.383
11	08 53 14.523	59 12 34.14	16.135	21.516
12	08 53 38.849	58 38 56.53	12.157	15.248
13	08 53 42.056	58 59 1.81	13.828	19.503
14	08 54 48.212	58 53 47.42	2.807	5.765

No extended continuum emission from the galaxy is present above the  $3\sigma$  level of the map. Furthermore, none of the continuum sources appear to be directly associated with any of the HI emission features. Table 3.5 gives the positions, peak intensity and integrated-intensity for the 14 continuum sources in the central  $512 \times 512$  region of the map as derived from gaussian fits to each source.

The continuum free line maps were then corrected for confusing sidelobes by CLEAN. The naturally weighted maps were cleaned down to the 0.86 mJy level, while the uniformly weighted maps were cleaned down to the 1.2 mJy level. The flux limit for CLEAN in both cases corresponds to approximately the  $2\sigma$  level of the maps. The clean components of the naturally weighted maps were restored using a synthesized beam of HPBW  $34''.33 \times 33''.63$ , with a beam position angle of  $82^\circ.95$ . Those for the uniformly

weighted maps were restored with a synthesized beam of HPBW  $11''.46 \times 9.''99$ , and a corresponding beam position angle of  $52.33^\circ$ .

Emission from the outer ring of the galaxy NGC 2685 is present in sixteen of the observed channels, while that from the inner ring is present in fourteen. The observations are centered on an optical heliocentric velocity of  $870.0 \text{ km s}^{-1}$ . The lowest channel in which emission is detected is that centered on  $725.0 \text{ km s}^{-1}$ , while the highest is centered on  $1035.9 \text{ km s}^{-1}$ . Each channel map containing emission from NGC 2685 is given in Figure 3.2 (a-p), in order of decreasing velocity. The velocity at the center of each channel is printed near the top of each map.

In the channel map of Figure 3.2 (a), centered on  $1035.9 \text{ km s}^{-1}$ , the emission in the NE is associated entirely with the outer ring. Figure 3.2 (b) shows both the emission associated with the inner polar ring component just SE of the center of the galaxy, and strong emission from the outer ring in the NE. Emission from both the inner and outer ring components is apparent in Figures 3.2 (c) and 3.2 (d), but the components cannot be cleanly separated. In Figures 3.2 (e) and 3.2 (f) the contours near the center of the galaxy seem to indicate the presence of the inner polar ring component. The southernmost closed contour in Figure 3.2 (e) at the  $2.5\sigma$  level is probably not a real feature, but one due to noise. Emission from the inner component can not be clearly distinguished from that due to the outer ring in Figures 3.2 (f) to 3.2 (i). Figures 3.2 (j) to 3.2 (n) show a contribution from the inner polar ring component just NW of the galactic center, but this emission is blended with that from the outer ring. In Figure 3.2 (o) emission from the inner polar ring component is seen as distinct from the outer ring component. The central peaks of the inner ring component in Figures 3.2 (b) and 3.2 (o) are clearly resolved, being separated by roughly 1.3 arcminutes. Also note that in Figures 3.2 (b) and 3.2 (c), the lowest level contours for the outer ring component in

Figure 3.2: (a-p) Naturally weighted, clean channel maps showing the distribution of HI in NGC 2685. The mean line of sight, heliocentric velocity for each map is printed at the top. Contour levels are multiples of the approximate r.m.s noise of 0.32 mJy/Beam:  $\sigma \times [-5, -2.5, 2.5, 5, 10, 20, 30, 40, 50, 60]$ . The spatial resolution of the maps is  $34''.34 \times 33''.64$  and the beam position angle is  $82^\circ.94$ . The channels centers are separated by  $20.73 \text{ km s}^{-1}$ . The pointing center for the observations,  $(\alpha, \delta)_{1950} = (08^h 51^m 41^s.2, 58^\circ 55' 30'')$ , is marked with a large “+”, while positions of stars in the optical image are marked with the smaller “+” signs. Minor tick marks are at 30 arcsecond intervals and major tick marks are labeled every two arcminutes from pointing center. North is at the top and West is to the right in these maps.

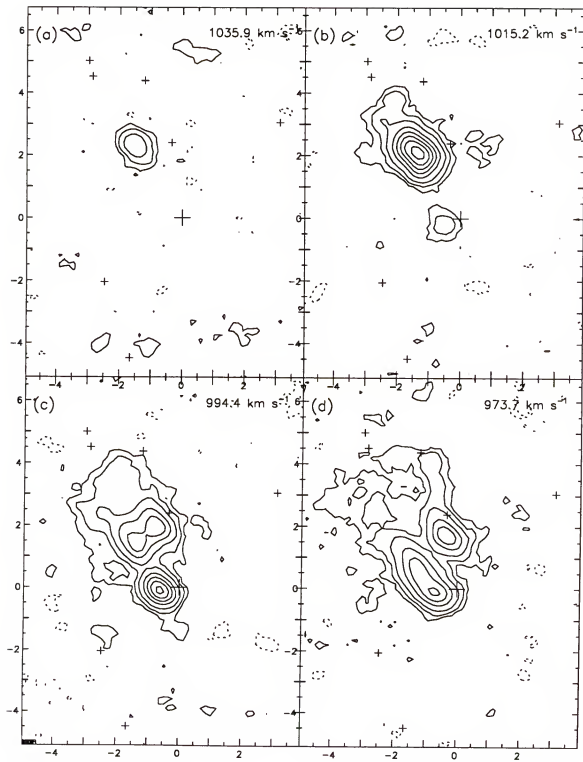


Figure 3.2: -- continued

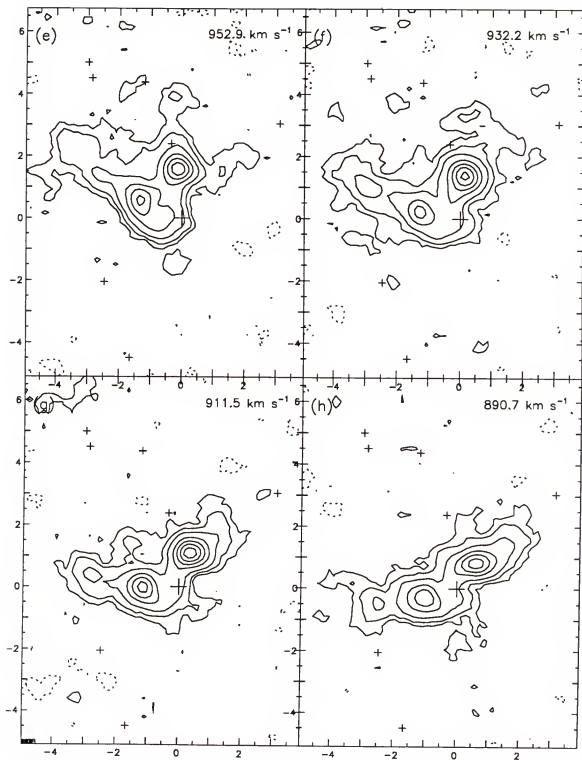


Figure 3.2: -- continued

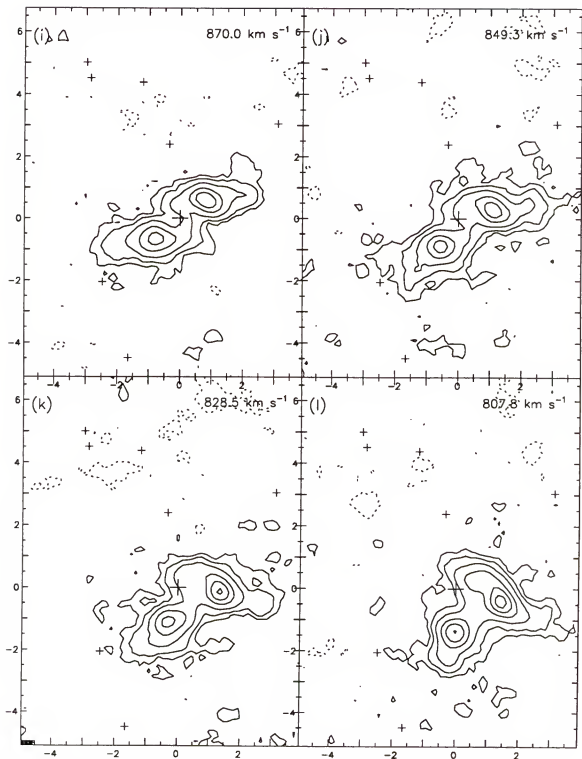


Figure 3.2: -- continued

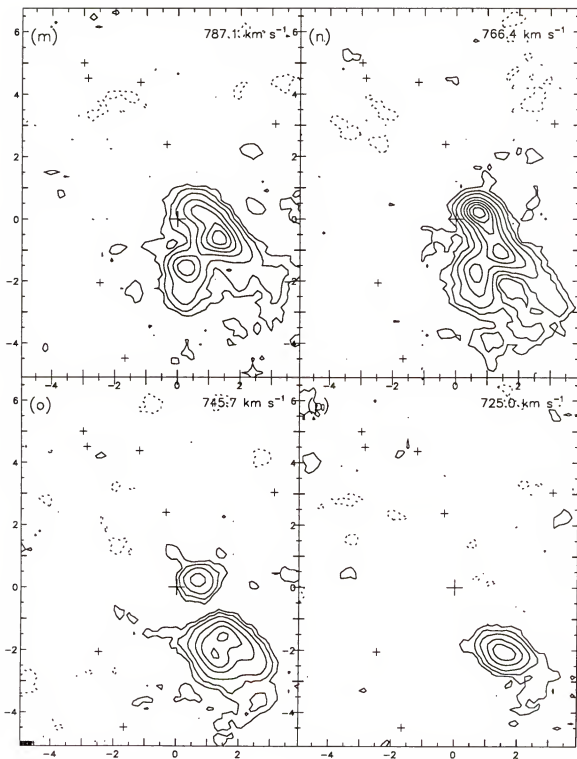


Figure 3.2: -- continued

the NE hook slightly to the NW, while in Figures 3.2 (n) to 3.2 (p), the corresponding region in the SW hooks slightly to the SE.

Figures 3.2 (b) and 3.2 (o) reveal that the distribution of HI in the inner ring component is symmetric with respect to the center of the galaxy. An axis drawn through the emission peaks of the inner ring component and the center of the galaxy in these two channels gives a position angle for the inner ring of  $110^\circ \pm 5^\circ$ , where the position angle is measured from North in the direction East to the first intersection with the axis. Similarly, a position angle of  $35^\circ \pm 5^\circ$  is obtained for the outer ring from an axis drawn through the emission peaks in the channel maps shown in Figures 3.2 (a) and 3.2 (p).

The naturally weighted channel maps therefore reveal the presence of two distinct components of the gas distribution that are inclined to one another. Both systems are very symmetric with respect to the galactic center, with the outer ring appearing slightly warped at its extremities. The outer ring component extends approximately 4.7 arcminutes from the center of the galaxy to the NE and SW. The blending of the two components due to the low resolution of these maps makes it difficult to ascertain the maximum extent of the inner ring. However, in Figure 3.2 (o), the inner polar ring is distinct from the outer ring and extends  $1.7 \pm 0.4$  arcminutes from the center of the galaxy at the  $2.5\sigma$  contour level. The mean velocity of the detected emission,  $\langle v_{gas} \rangle$ , as derived from the maps made with natural weighting, is  $880 \text{ km s}^{-1} \pm 7 \text{ km s}^{-1}$ . Relative to  $\langle v_{gas} \rangle$ , the maximum line of sight velocity for the outer ring is  $156 \text{ km s}^{-1} \pm 12 \text{ km s}^{-1}$  at a maximum distance of  $4.7 \pm 0.4$  arcminutes from the galactic center. Similarly, the maximum line of sight velocity of the gas associated with the inner polar ring is  $135 \text{ km s}^{-1} \pm 12 \text{ km s}^{-1}$  at a maximum distance of  $1.7 \pm 0.4$  arcminutes from the center of the galaxy.

The maps made with uniform weighting of the visibilities have a synthesized HPBW that is roughly one third that of the naturally weighted maps. However, the r.m.s. sensitivity of the uniformly weighted maps, 0.56 mJy/Beam, is only about sixty percent that of the naturally weighted maps. The signal strength in the uniformly weighted maps is quite low for all but the brightest regions. These maps are shown in Figure 3.3. Emission from NGC 2685 is present in 15 of the channel maps, over a velocity range of  $290 \text{ km s}^{-1}$ . The emission peaks due to the inner polar ring component, shown in Figures 3.3 (c) and 3.3 (o), are clearly resolved with a separation of  $1.4 \pm 0.1 \text{ arcminutes}$ . These emission peaks are roughly equidistant from the optical center of the galaxy. The channel separation between the peaks corresponds to a velocity width for the inner, polar ring component of  $249 \text{ km s}^{-1} \pm 12 \text{ km s}^{-1}$ , or a velocity half width of  $124 \text{ km s}^{-1}$ . The position angle of the major axis of the inner, polar ring in these high resolution maps is  $110^\circ \pm 5^\circ$ , as measured from North towards East, consistent with that determined from the naturally weighted maps. Moreover, the position angle for the projected major axis of the outer ring, as derived from these high resolution maps, is  $35^\circ \pm 5^\circ$ , consistent with the value derived from the naturally weighted maps. Thus the inclination of the projected major axis of the inner polar ring to the projected minor axis of the outer ring is about  $15^\circ$ .

The uniformly weighted maps give a mean velocity for the gas of  $870 \text{ km s}^{-1} \pm 7 \text{ km s}^{-1}$ . The apparent discrepancy between the mean systemic velocity of  $870 \text{ km s}^{-1}$  derived here, and that of  $880 \text{ km s}^{-1}$  derived from the naturally weighted channel maps is due to the greater sensitivity of the naturally weighted maps. Note that in the latter maps emission from the outer ring is detected at  $1036 \text{ km s}^{-1}$ , while emission from the inner ring is detected at  $1015 \text{ km s}^{-1}$ . Emission from each of these respective

components is not detected in the corresponding maps made with uniform weighting; i.e., Figures 3.3 (a) and 3.3 (p).

Since the low signal to noise ratio for the maps made with uniform weighting prevented the detection of a significant amount of the emission from regions of interest in this galaxy, the uniformly weighted maps were convolved down to a HPBW of  $14''.00 \times 14''.00$  to increase the sensitivity to low level emission. Below, Figures 3.4 and 3.5 give velocity profiles along the major axis of the outer HI ring, for PA =  $35^\circ$ , as derived from the smoothed, uniformly weighted maps and the naturally weighted maps, respectively. The horizontal dotted line across each profile corresponds to the mean velocity of the HI gas,  $880 \text{ km s}^{-1}$ . Profiles along the position angle of the major axis of the inner, "polar" ring at PA =  $110^\circ$  are shown in Figures 3.6 and 3.7. These profiles can be used to obtain an approximate rotation curve for each of the rings in the galaxy simply by following the intensity contours just inside the high and low velocity extremes of the profile, and determining the line of sight velocity as a function of position along the projected major axis of the ring.

Approximately 17.3 arcminutes NW of NGC 2685, emission from the dwarf galaxy MCG+10-13-030 appears in the naturally weighted channel maps. The mean velocity of the gas is  $1015 \text{ km s}^{-1} \pm 7 \text{ km s}^{-1}$  and the velocity width is  $83 \text{ km s}^{-1} \pm 14 \text{ km s}^{-1}$ . The peak emission from this galaxy,  $3.8 \text{ mJy/Beam}$ , occurs in the channel centered on  $1056.7 \text{ km s}^{-1}$  and is located at  $(\alpha, \delta) = (08^h 50^m 25^s, 59^\circ 09' 52''.6)$ . In the channel centered on  $973.7 \text{ km s}^{-1}$ , the emission peak of  $3.4 \text{ mJy Beam}^{-1}$  is located at  $(\alpha, \delta)_{1950} = (08^h 50^m 29.^s832, 59^\circ 08' 49''.78)$ . The position and velocity of this galaxy is consistent with the position of the dwarf galaxy MCG+10-13-030 given by Dixon and Sonneborn (1980). Figures 3.8 (a) to 3.8 (e) contain the naturally weighted channel maps for this galaxy.

Figure 3.3: (a-p) Uniformly weighted, clean channel maps showing the distribution of HI in NGC 2685. The mean line of sight, heliocentric velocity for each map is printed at the top. Contour levels are multiples of the approximate r.m.s noise of 0.56 mJy/Beam:  $\sigma \times (-5, -3, 3, 5, 7)$ . The spatial resolution of the maps is  $11''.46 \times 9''.99$  and the beam position angle is  $52^\circ.33$ . Channel separations are  $20.73 \text{ km s}^{-1}$ . The pointing center for the observations,  $(\alpha, \delta)_{1950} = (08^h 51^m 41^s.2, 58^\circ 55' 30'')$ , is marked with a large “+”, while positions of stars in the optical image are marked with the smaller “+” signs. Minor tick marks are at 15 arcsecond intervals and major tick marks are labeled every two arcminutes from pointing center. North is at the top and West is to the right.

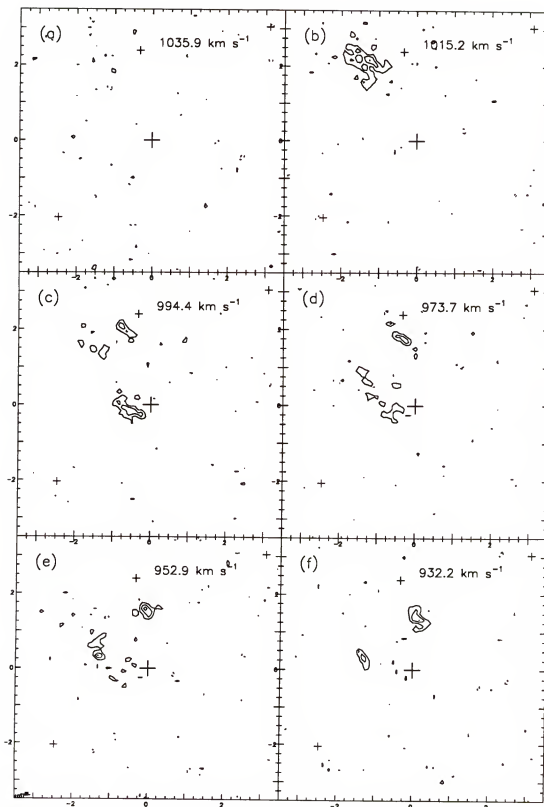


Figure 3.3: -- continued

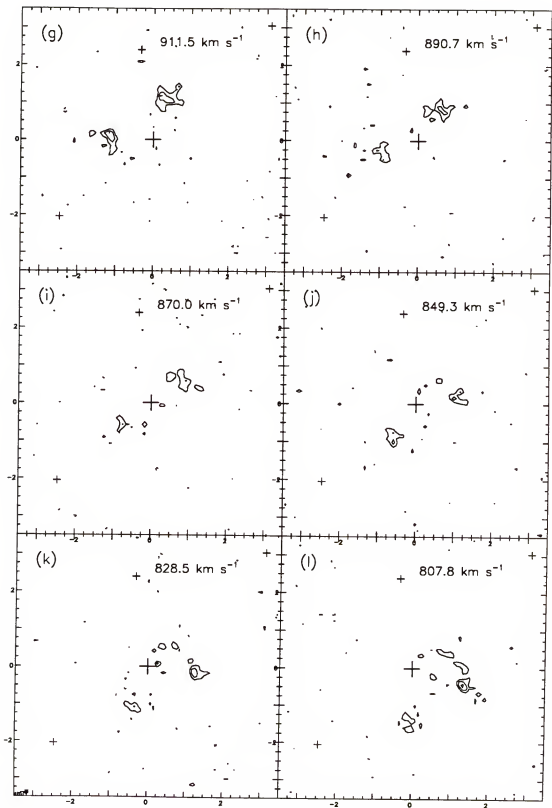


Figure 3.3: -- continued

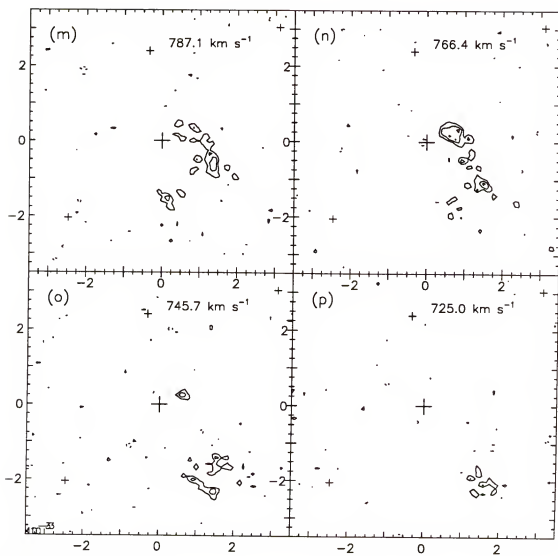


Figure 3.3: -- continued

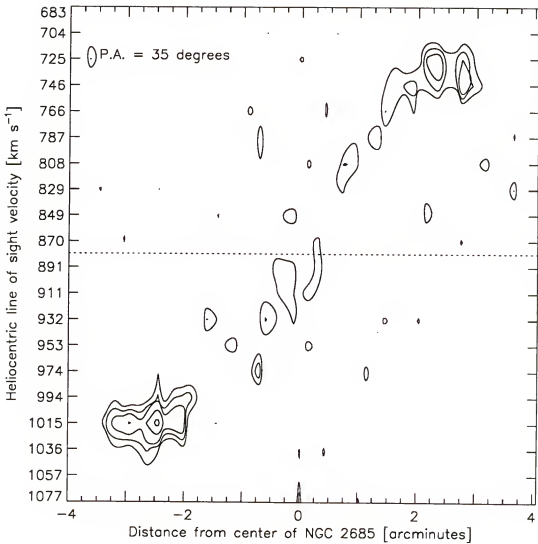


Figure 3.4: High resolution axis-velocity profile along the major axis of the outer HI ring of NGC 2685 at P.A. = 35°, derived from the smoothed uniformly weighted map cube. The spatial resolution is 14".00 × 14".00 and the velocity resolution is 24.876 km s<sup>-1</sup>. Channel separations are 20.73 km s<sup>-1</sup>. Contour levels are multiples of the r.m.s. map noise of 0.56 mJy/Beam:  $\sigma \times [2, 3, 4, 6, 8, 10]$ . Moving from left to right on the x-axis of the plot corresponds to moving from NE to SW along the projected major axis of the outer HI ring.

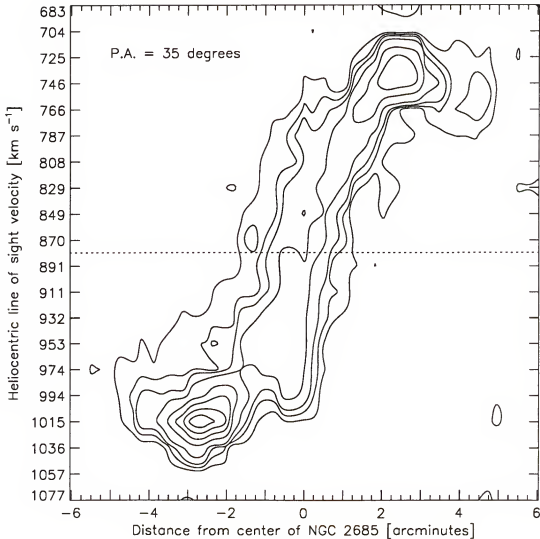


Figure 3.5: High sensitivity velocity profile along the major axis of the outer HI ring of NGC 2685 at P.A. = 35°, derived from the naturally weighted map cube. The spatial resolution is 34".34 × 33".64 and the velocity resolution is 24.876 km s<sup>-1</sup>. Channel separations are 20.73 km s<sup>-1</sup>. Contour levels are multiples of the r.m.s. map noise of 0.34 mJy/Beam:  $\sigma \times [2, 4, 6, 10, 20, 30, 40, 50]$ . Moving from left to right on the x-axis of the plot corresponds to moving from NE to SW along the projected major axis of the outer HI ring.

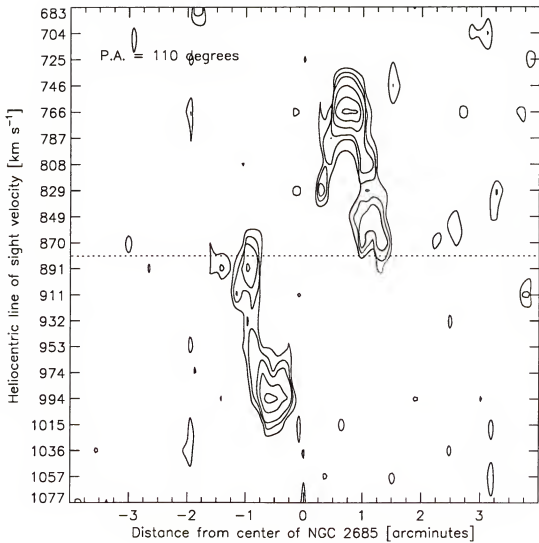


Figure 3.6: High resolution velocity profile along the major axis of the inner, “polar” ring of NGC 2685 at P.A. = 110°, derived from the smoothed uniformly weighted map cube. The spatial resolution is 14".00 × 14".00 and the velocity resolution is 24.876 km s<sup>-1</sup>. Channel separations are 20.73 km s<sup>-1</sup>. Contour levels are multiples of the r.m.s. map noise of 0.56 mJy/Beam:  $\sigma \times [2, 3, 4, 6, 8, 10]$ . Moving from left to right on the x-axis of the plot corresponds to moving from SE to NW along the projected major axis of the inner HI ring.

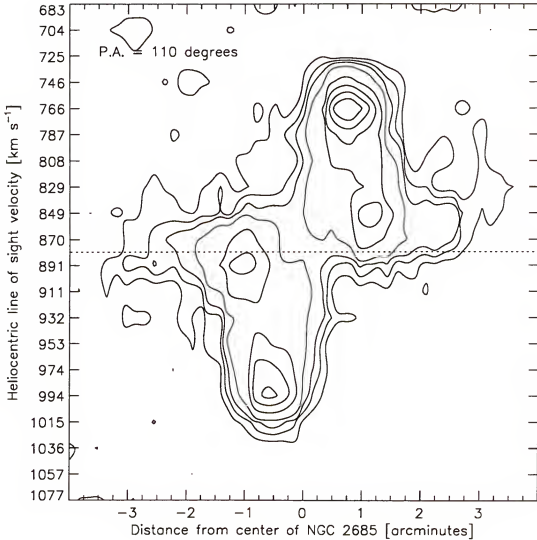


Figure 3.7: High sensitivity velocity profile along the major axis of the inner, “polar” ring of NGC 2685 at P.A. = 110°, derived from the naturally weighted map cube. The spatial resolution is 34''.34 × 33''.64 and the velocity resolution is 24.876 km s<sup>-1</sup>. Channel separations are 20.73 km s<sup>-1</sup>. Contour levels are multiples of the r.m.s. noise of 0.34 mJy/Beam:  $\sigma \times [2, 4, 6, 10, 20, 30, 40, 50]$ . Moving from left to right on the x-axis of the plot corresponds to moving from SE to NW along the projected major axis of the inner, polar ring of NGC 2685.

At 17 arcminutes from pointing center, the response of the primary beam causes the amplitude of the observed signal to be reduced considerably from the maximum response at pointing center. A correction for the response of the primary beam, as given by the AIPS imaging software, is computed as follows:

$$F = a_0 + a_1x + a_2x^2 + a_3x^3 + a_4x^4, \quad (3.24)$$

where  $x$  is given by (distance from pointing center [arcmin]  $\times$  observing frequency[GHz])<sup>2</sup> and

$$\begin{aligned} a_0 &= 0.9920378 \\ a_1 &= 0.9956885 \times 10^{-3} \\ a_2 &= 0.3814573 \times 10^{-5} \\ a_3 &= -0.5311595 \times 10^{-8} \\ a_4 &= 0.3980963 \times 10^{-11}. \end{aligned} \quad (3.25)$$

For an object at distance  $x$  from pointing center, the observed signal is given by  $1/F$  times that at pointing center. Thus, the response to the signal from MCG+10-13-030 is about 43 percent of that which would be obtained if this galaxy was at the pointing center of the observations.

The naturally weighted maps also contain line emission roughly 25 arcminutes NE of NGC 2685, at the high velocity edge of the bandpass. The peak of 1.97 mJy/Beam, about  $6\sigma_{rms}$ , is located at  $(\alpha, \delta)_{1950} = (08^{\text{h}} 53^{\text{m}} 51^{\text{s}}.38, 59^{\circ} 13' 43''.96)$ . Though this feature could be an artifact, it seems to be real. As shown in Figures 3.9 (a) and 3.9 (b), the emission appears to be extended but is very weak and doesn't move noticeably between  $1181 \text{ km s}^{-1}$  and  $1161 \text{ km s}^{-1}$ . In channel one, at  $1181 \text{ km s}^{-1}$ , the emission is approximately two arcminutes in extent. The intensity contours appear to be compressed at the SE edge, with the emission extending, at a lower level, to the NW. Emission is also

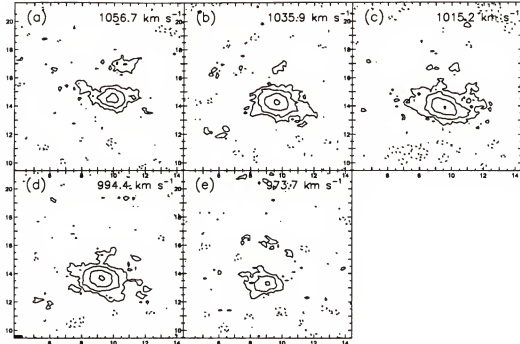


Figure 3.8: Naturally weighted, clean HI channel maps of MCG +10-13-030. The mean line of sight, heliocentric velocity is printed at the top of each map. Contour levels are multiples of the approximate r.m.s noise of 0.32 mJy/Beam:  $\sigma \times [-5, -2.5, 2.5, 5, 10, 20, 30, 40, 50, 60]$ . These maps have a spatial resolution of  $34''.34 \times 33''.64$ , a beam position angle of  $82^\circ.94$ , and channel separations of  $20.73 \text{ km s}^{-1}$ . Distance labels on x and y axes are in arcminutes W and N of NGC 2685, respectively. Minor tick marks are at 30 arcsecond intervals and major tick marks correspond to the distance in arcminutes from pointing center. North is at the top and West is to the right in these maps.

present, though marginally, in the maps at  $932$  and  $912 \text{ km s}^{-1}$ , about 27 arcminutes NE of NGC 2685. This emission may be associated with the galaxy UGC 4683 as discussed below (also see Table 3.6). Note that attenuation due to the response of the primary beam is severe at this distance from pointing center, with the signal strength only about 14 percent of what it would be if the object were at pointing center.

The position and velocity of the just detectable emission at  $932 \text{ km s}^{-1}$  and  $912 \text{ km s}^{-1}$  is consistent with the published value for UGC 4683. However, The General Catalogue of HI Observations (Huchtmeier and Richter, 1989) gives an HI velocity width (at the 20 percent level) for UGC 4683 of about  $76 \text{ km s}^{-1}$ . Therefore, it is not clear if the

stronger emission observed at  $1161 \text{ km s}^{-1}$  and  $1181 \text{ km s}^{-1}$  is associated with UGC 4683, or with a yet unidentified galaxy. Table 3.6 lists the positions and velocities of the observed emission, as well as catalogued positions and velocities of galaxies that may be associated with this emission. Redshift information is needed for three of the galaxies in the list if one wishes to establish any definite connection between one of these objects and the HI emission detected NE of NGC 2685.

Since the maps made with natural weighting of the visibilities have a higher signal to noise ratio than those made with uniform weighting, the former maps are better for the computation of global HI profiles and total detected mass of HI. In order to obtain the best estimate of the detected HI emission, a correction for primary beam attenuation must be made. If this correction is applied to the maps as is, a gradient in the noise level will be imposed upon the map, with the noise increasing with distance from pointing center. This gradient in noise is not desirable if one later wishes to isolate emission regions by eliminating regions below a given flux cutoff. Thus, in order to correct for primary beam attenuation, the following approach is taken. First, another complete set of maps is constructed, by spatially smoothing the maps *via* convolution with a circular gaussian to a final HPBW of  $54''$ . Second, the smoothed maps are Hanning smoothed in velocity, using a triangular function with a width of three channels between first nulls. Each of these smoothed maps is examined for the presence of line emission. Pixels in regions not containing emission from the galaxy above a given cutoff in flux are blanked out on the smoothed maps. The appropriate value of the flux cutoff is determined by trying several different cutoffs and examining the emission regions in the resulting maps. A cutoff of  $1.19 \text{ mJy/Beam}$ , corresponding to 3.5 times the r.m.s. noise of the unsmoothed maps is applied to the smoothed maps to form the mask, which in turn is applied to the unsmoothed map cube. The correction for primary beam attenuation is then applied to

the unsmoothed, masked maps. Finally, global profiles for each galaxy are computed by summing over the emission in each of the masked, original maps which have been corrected for primary beam attenuation. The global profile for NGC 2685 is given in Figure 3.10, while that for MCG+10-13-030 is given in Figure 3.11.

Table 3.6: Dwarf galaxies near NGC 2685.

Object	Type	Position ( $\alpha, \delta$ ) <sub>1950</sub>		V [km s <sup>-1</sup> ] (Heliocentric)	$\Delta V$	Source
Catalogue Objects						
UGC 4683	Im	08 54 00	59 16 00	927.0	76	GCHO <sup>a</sup>
DwIr						
MAI 037	Dw	08 53 41	59 17			MLNO <sup>b</sup>
Sph						
MCG+10-13-046		08 54	59 16			MLNO <sup>b</sup>
MCG+10-13-030		08 50 30	59 08			MLNO <sup>b</sup>
VLA HI Detections						
Emission peaks in NE		08 53 57	59 16 26	911.5		
		08 53 59	59 16 26	932.2		
		08 53 51	59 13 52	1160.5		
		08 53 51	59 15 14	1181.3		
MCG+10-13-030		08 50 26	59 09 26	1015.2	83	

a) A General Catalogue of HI Observations of Galaxies (Huchtmeier and Richter, 1989)

b) A Master List of Nonstellar Optical Astronomical Objects (Dixon and Sonneborn, 1980)

The total mass of hydrogen can be computed from the brightness temperature as derived from the observed intensity of radiation, if the emitting gas can be assumed to be optically thin. However, if the gas is optically thick, this approximation breaks down and the brightness temperature will approach the spin temperature of the gas which is typically about 100 °K. Thus, for optically thin gas, the column density of HI (atoms cm<sup>-2</sup>) is related to the observed brightness temperature at any point by the following relation

$$N_H(x, y) = 1.8226 \times 10^{18} \int_{-\infty}^{\infty} T_B(x, y) dv, \quad (3.26)$$

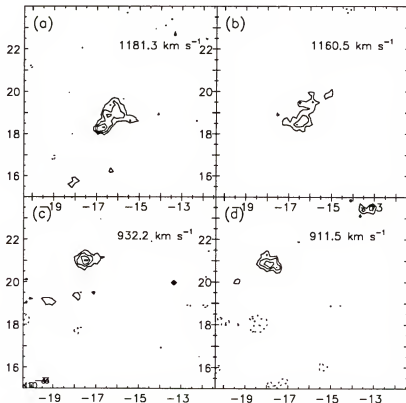


Figure 3.9: HI emission detected NE of NGC 2685. Contour intervals are in multiples of the r.m.s. noise of 0.32 mJy/Beam:  $\sigma \times (-5, -4, -3, 3, 4, 5, 6)$ , with negative contours as broken lines. The spatial resolution is  $34''.34 \times 33''.64$  with a beam position angle of  $82^\circ.94$ , and channel separations of  $20.73 \text{ km s}^{-1}$ . Distance labels on the x and y axes are in arcminutes from NGC 2685, measured positive to the N and negative to the E. Minor tick marks are at 30 arcsecond intervals. North is to the top and West to the left.

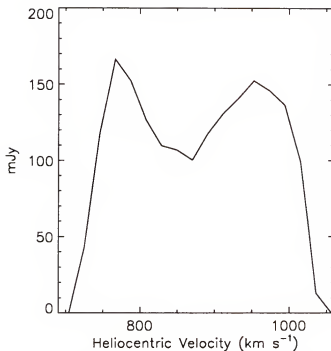


Figure 3.10: Global HI profile for NGC 2685 computed from masked and primary beam corrected, naturally weighted channel maps.

where the velocity  $v$  is in  $\text{km s}^{-1}$  and  $T_B$  in  $^{\circ}\text{K}$  (Mihalas and Binney, 1981). The brightness temperature at a given point is related to the measured flux density of the source by

$$T_B(x, y, \nu) = \frac{1222.09}{\nu^2 \theta_1 \theta_2} S(x, y, \nu), \quad (3.27)$$

where  $\theta_1$  and  $\theta_2$  are the full widths at half maximum of the synthesized, elliptical gaussian beam in arcseconds,  $S$  is in mJy/Beam and  $\nu$  is in GHz.

The moments of the radiation field are computed from the map cube that has been masked and corrected for primary beam attenuation. Integration of the masked map cube over velocity gives the zeroth moment of the radiation field which is the integrated-intensity; i. e.,

$$I(x, y) = \Delta v \sum_{k=1}^{nch} I_k(x, y), \quad (3.28)$$

where  $I$  is in mJy/Beam and  $nch$  is the number of channels containing emission from the galaxy. The intensity-weighted mean velocity, or first moment of the radiation field, is given by

$$\langle v(x, y) \rangle = \frac{\sum_{k=1}^{nch} v_k \times I_k(x, y)}{I(x, y)}, \quad (3.29)$$

where each  $v_k$  corresponds to the velocity at the center of the  $k$ th channel.

A cutoff of 1.19 mJy/Beam, corresponding to 3.5 times the r.m.s. noise of the unsmoothed maps is applied to the smoothed maps to form the mask which, in turn, is applied to the unsmoothed map cube. Figures 3.12 and 3.13 give the resulting integrated-intensity field of HI and the intensity-weighted velocity field, respectively.

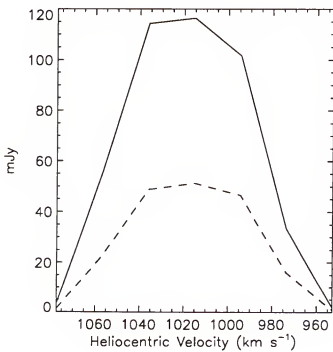


Figure 3.11: Global HI profile for MCG+10-13-030. The solid line gives the profile derived following the correction for primary beam attenuation. The dashed line gives the profile derived from the original, naturally weighted map cube.

In the integrated-intensity map the gas extends up 4.7 arcminutes from the center of the galaxy. At the lowest contour levels the gas in the North (top) appears to hook towards the West (to the right), while the gas in the South appears to hook towards the East. The higher level contours appear to be very symmetric about the center of the galaxy. Near the center, the high intensity peaks are due to the superposition of the inner and outer HI rings along the line of sight. Note that the lowest density regions in the inner regions of the integrated-intensity map are no lower than 25% of the map maximum of  $1.53 \times 10^3$  Jy/Beam × m/s, which corresponds to a column density of  $1.47 \times 10^{21}$  atoms cm<sup>-2</sup>.

In the inner regions of the velocity map there are “tongues” in the contours due to the superposition of the velocity components from both the inner and outer ring along the line of sight. In other words, the spectra in this region are doubly peaked. Recall that in the naturally weighted channel maps, a clear separation of these components is only possible in the channels centered on 745 km s<sup>-1</sup> and 1015 km s<sup>-1</sup>. Even though both components are quite evident in a number of channels centered on velocities closer to the systemic velocity of the galaxy, they can not be separated from one another in a simple way.

To obtain the total HI mass detected for the galaxy, the flux is integrated over the emission region in the integrated-intensity map. If the corrected recessional velocity of NGC 2685, is 965 km s<sup>-1</sup> (see Table 3.1), integration over the source gives a total HI mass of  $8.5 \times 10^8 \times h^{-2}$  solar masses ( $M_\odot$ ), where  $h \equiv H_0/100$ . Choosing  $h = 0.5$ , a total HI mass of  $3.4 \times 10^9 M_\odot$  is obtained, compared to the  $2.1 \times 10^9 M_\odot$  detected by Shane (1980) using the Westerbork Radio Synthesis Telescope.

Figure 3.14 shows the integrated-intensity field as derived from the high resolution maps; i. e., those made with uniform weighting of the visibilities. The masks used

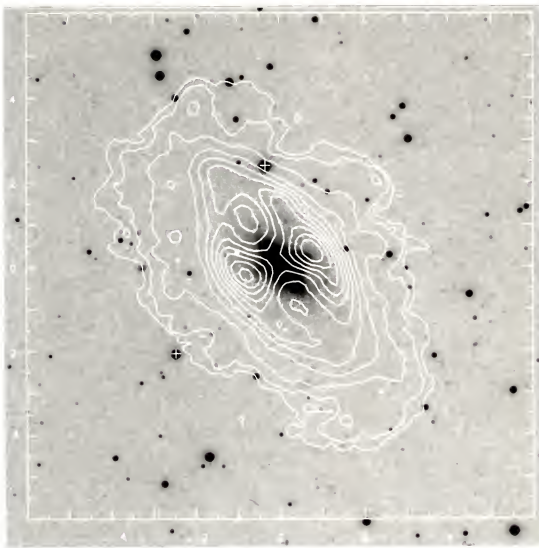


Figure 3.12: Integrated-intensity of HI for NGC 2685 derived from maps made with natural weighting of the visibilities. The contours are shown over an optical (blue) image of the galaxy obtained from a Palomar Sky Survey print. Contour intervals are in fractions of the map maximum of  $1.53 \times 10^3$  Jy/Beam  $\times$  m/s  $\times$  [0.03, 0.05, 0.1, 0.2, 0.3, 0.4, 0.5, 0.6, 0.7, 0.8, 0.9, 1.0]. The map maximum corresponds to an HI column density of  $1.47 \times 10^{21}$  atoms cm $^{-2}$ . North is at the top and East to the left. Stars in the field are marked with small +'s. The spatial resolution, as given by the HPBW of the synthesized beam, is  $34''.34 \times 33''.64$  with a beam position angle of  $82^\circ.95$ .



Figure 3.13: Intensity-weighted mean velocity field of NGC 2685 derived from maps made with natural weighting of the visibilities. The contours are shown over an optical (blue) image of the galaxy obtained from a Palomar Sky Survey print. Contour intervals are in  $\text{km s}^{-1}$ , for values at the center of each channel. The observations are centered on  $870 \text{ km s}^{-1}$ . Stars in the field are marked with small +'s. The spatial resolution of the map is  $34''.34 \times 33''.64$  with a beam position angle of  $82^\circ.95$ , and the velocity resolution of the observations is  $24.876 \text{ km s}^{-1}$ .

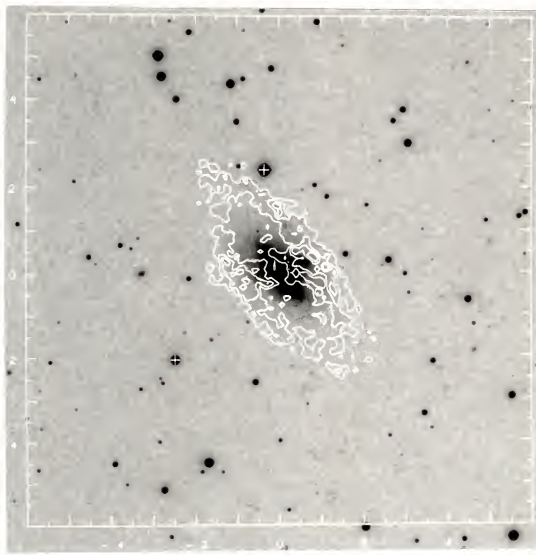


Figure 3.14: Integrated-intensity of HI for NGC 2685 derived from maps made with uniform weighting of the visibilities. The contours are shown over an optical (blue) image of the galaxy obtained from a Palomar Sky Survey print. Contour intervals are in fractions of the map maximum of  $288 \text{ Jy/Beam} \times \text{m/s} \times [0.2, 0.4, 0.6, 0.8, 1.0]$ . The map maximum corresponds to a column density of  $2.8 \times 10^{21} \text{ atoms cm}^{-2}$ . North is at the top and East is to the left. Stars in the field are marked with small +'s. The spatial resolution, as given by the HPBW of the synthesized beam, is  $11''.46 \times 9''.99$  with a beam position angle of  $52^\circ.33$ .

to isolate the emission regions on these maps were constructed by convolving the uniformly weighted cube with an elliptical gaussian down to a HPBW of  $20'' \times 20''$ ; Hanning smoothing in velocity, using a triangular function with a width of three channels between first nulls; and finally, applying a flux cutoff of 1.4 mJy/Beam to the smoothed map cube.

In order to facilitate comparison between the lower resolution, naturally weighted, moment maps and the uniformly weighted, integrated-intensity map, Figure 3.14 is drawn at the same scale as the maps shown in Figures 3.12 and 3.13. Note that the emission in Figure 3.14 clearly delineates regions of high column density in the outer and inner rings of NGC 2685. Low level emission, which is present in the inner and outermost regions of the galaxy, does not show up in this map however. Along the perimeter of the outer ring component in Figure 3.14, there are regions of enhanced brightness due to the superposition of the inner and outer rings along the line of sight. The density enhancement in the East sweeps to the north, while the one in the West sweeps to the South.

The high resolution map of Figure 3.14 reveals a bright spot in the NW part of the outer ring. On the lower resolution map of Figure 3.12, this feature produces an asymmetry in the contours at the fifty and sixty percent level. While this feature cannot be distinguished on the naturally weighted channel maps it appears to be associated with the emission in the NW of the maps shown in Figures 3.3 (e) and 3.3 (f), corresponding to the channels centered on  $952.9 \text{ km s}^{-1}$  and  $932.2 \text{ km s}^{-1}$ . To check this, an axis velocity profile was made from the smoothed, uniformly weighted maps, running from South to North through the center of the galaxy. This corresponds to a position angle of zero degrees which cuts right through the feature seen in Figure 3.14. This profile is shown in Figure 3.15. At a distance of 1.5 arcminutes North of the center of the

galaxy, the spectrum does not appear to be doubly peaked; however, the column density is clearly higher in the North than in the South. Therefore, the feature is most likely due to an uneven distribution of gas in the ring. Due to the low sensitivity of the uniformly weighted maps the intensity-weighted mean velocity map has a very patchy appearance and does not provide anything new in the way of information about the galaxy; hence, it is not presented here.

Table 3.7 summarizes the characteristics of the HI in NGC 2685 as derived from these observations, while the characteristics of the HI in MCG+10-13-30 are given in Table 3.8.

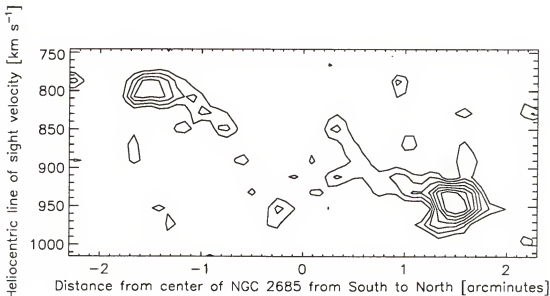


Figure 3.15: Velocity profile of NGC 2685 taken along a position angle of zero degrees. This profile was derived from the smoothed uniformly weighted map cube. The spatial resolution is  $14''.00 \times 14''.00$  and the velocity resolution is  $24.876 \text{ km s}^{-1}$ . Channel separations are  $20.73 \text{ km s}^{-1}$ . Contour levels are multiples of the r.m.s. map noise of  $0.56 \text{ mJy/Beam}$ :  $\sigma \times [2, 3, 4, 6, 8, 10]$ . Moving from left to right on the x-axis of the plot corresponds moving from S to N through the center of the galaxy.

Table 3.7: HI characteristics of NGC 2685.

NGC 2685	Inner Ring	Outer Ring
Major Axis Position angle [degrees] <sup>a</sup>	$110 \pm 5$	$35 \pm 5$
Maximum Radius [arcminutes]	$1.7 \pm 0.4$	$4.7 \pm 0.4$
Velocity half width [ $\text{km s}^{-1}$ ]	$135 \pm 14$	$156 \pm 14$
Total HI mass [ $M_{\odot}$ ] <sup>b</sup>	$8.5 \times 10^8 \times h^{-2}$	
Assumed Distance [Mpc]	$9.65 \times h^{-1}$	
Mean systemic velocity of HI gas [ $\text{km s}^{-1}$ ]	$880 \pm 7$	

<sup>a</sup> Measured from North to East to the side of the projected major axis with positive line of sight velocity.

<sup>b</sup> Computed for  $H_0=100 \text{ km s}^{-1} \text{ Mpc}^{-1}$ , where  $0.5 \leq h \leq 1.0$ .

Maps of the integrated-intensity and intensity-weighted mean velocity for the dwarf galaxy MCG+10–13–030 are given in Figure 3.16 and Figure 3.17. These maps were constructed from the naturally weighted channel maps using a mask created by spatially smoothing down to a HPBW of  $54'' \times 54''$ , and employing a flux cutoff on the smoothed maps of 2.5 times the r.m.s. noise of the unsmoothed maps. A correction for primary beam attenuation was made on the masked, unsmoothed cube before calculating the moments. If MCG+10–13–030 is taken to be at the same distance as NGC 2685, then the total HI mass for MCG+10–13–030 is  $2.0 \times h^{-2} \times 10^8 M_{\odot}$ .

If one considers the proximity of MCG+10–13–030 to NGC 2685, the question of whether the dwarf galaxy is a satellite of NGC 2685 naturally arises. An estimate of the total mass required for MGC 10–13–030 to be in a bound orbit can be obtained from

conservation of energy; i. e.,

$$v_{esc}^2 = G(M + m) \left( \frac{2}{r} - \frac{1}{a} \right), \quad (3.30)$$

where  $v$  is the escape velocity of the satellite,  $M$  is the mass of NGC 2685,  $m$  is the mass of MCG+10-13-030,  $a$  is the semi-major axis of the orbit and  $r$  is the distance of MCG+10-13-030 from NGC 2685. For a parabolic orbit  $a = \infty$  while for a circular orbit  $r = a$ . The expression for the binding mass of the system is thus given by

$$M_B = \frac{rv_{esc}^2}{2G}. \quad (3.31)$$

Given the radial velocity separation ( $\Delta v_r$ ) of the two galaxies, if the satellite orbit is circular, then the escape velocity can be obtained from  $v_{esc} = \Delta v_r \times \csc I$ , where  $I$  is the unknown inclination of the satellite orbit. For NGC 2685 and MCG+10-13-030,

Table 3.8: HI characteristics of MCG+10-13-030.

MCG 10 - 13 - 030	
Diameter [arcminutes]	$5.0 \pm 0.4$
Mean heliocentric velocity of HI gas ( $v_{sys}$ ) [km s <sup>-1</sup> ]	$1015 \pm 7$
Velocity full width [km s <sup>-1</sup> ]	$83 \pm 14$
Total HI mass [ $M_\odot$ ] <sup>a</sup>	$2.0 \times 10^8 \times h^{-2}$
Distance [Mpc] <sup>b</sup>	$9.65 \times h^{-1}$

<sup>a</sup> Computed for  $H_0 = 100$  km s<sup>-1</sup> Mpc<sup>-1</sup>, where  $0.5 \leq h \leq 1.0$ .

<sup>b</sup> Assumed to be at distance of NGC 2685

$\Delta v_r = 145 \text{ km s}^{-1}$ . Therefore, if the unknown inclination and eccentricity of the satellite orbit are neglected, and if the angular distance between NGC 2685 and MCG+10-13-030 of 17.3 arcminutes corresponds to a linear distance of  $48.6 \text{ h}^{-1} \text{ kpc}$ , then a lower limit estimate of the total mass needed to bind MCG+10-13-030 to NGC 2685 is about  $1.2 \times 10^{11} \text{ h}^{-1} M_\odot$ . A Keplerian estimate for the mass of NGC 2685 at the maximum extent of the HI gives  $9.5 \times 10^{10} \text{ h}^{-1} M_\odot$  for an inclination of the galaxy of  $62^\circ$ , a distance

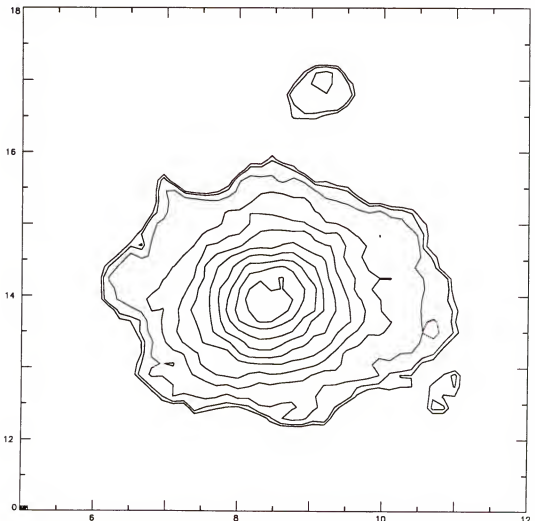


Figure 3.16: Integrated-intensity of HI for MCG+10-13-030 derived from maps made with natural weighting of the visibilities. Contour intervals are in fractions of the map maximum of  $851.2 \text{ Jy/Beam} \times \text{m/s} \times [0.03, 0.05, 0.1, 0.2, 0.3, 0.4, 0.5, 0.6, 0.7, 0.8, 0.9, 1.0]$ . The map maximum corresponds to an HI column density of  $8.18 \times 10^{20} \text{ atoms cm}^{-2}$ . The North is at the top and East to the left. The spatial resolution is given by the HPBW of the synthesized beam,  $34''.34 \times 33''.64$ . Axes are labeled in terms of arcminutes from the center of NGC 2685.

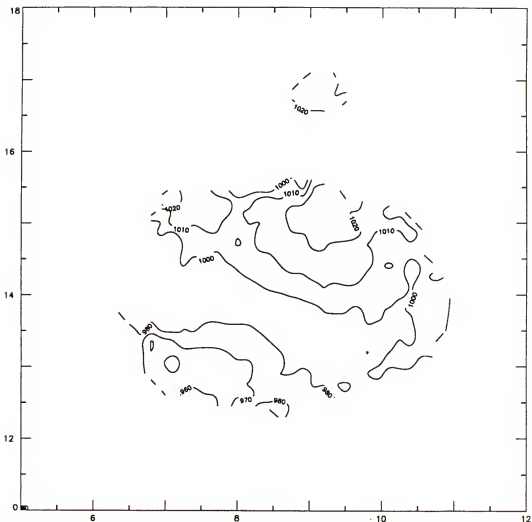


Figure 3.17: Intensity-weighted mean velocity field of HI for MCG+10-13-030 derived from maps made with natural weighting of the visibilities. North is at the top and East to the left. Contour intervals are in units of  $\text{km s}^{-1}$ . The spatial resolution is given by the HPBW of the synthesized beam,  $34''.34 \times 33''.64$ . The velocity resolution of the observations is  $24.878 \text{ km s}^{-1}$ , and the channel separation is  $20.73 \text{ km s}^{-1}$ . Axes are labeled in terms of arcminutes from the center NGC 2685.

of  $9.65 \text{ h}^{-1} \text{ Mpc}$ , and a projected HI rotational velocity of  $156 \text{ km s}^{-1}$  at a radius of  $4.7 \text{ arcminutes}$ , or  $13.2 \text{ h}^{-1} \text{ kpc}$ . Similarly, the Keplerian mass of MCG+10-13-30 is estimated to be  $1.1 \times 10^{10} \text{ h}^{-1} M_{\odot}$ , given an assumed distance of  $9.65 \text{ h}^{-1} \text{ Mpc}$ , an arbitrary choice for the inclination of the galaxy of  $30^\circ$ , and a projected HI rotational velocity component of  $42 \text{ km s}^{-1}$  at a radius of  $7.1 \text{ h}^{-1} \text{ kpc}$ . Thus the total Keplerian mass for both MCG+10-13-30 and NGC 2685 is  $1.1 \times 10^{11} \text{ h}^{-1} M_{\odot}$ . This rudimentary

calculation seems to indicate that the Keplerian mass indicated by the HI observations is slightly less than that required for MCG+10-13-030 to be a bound satellite. However, given the uncertainties in the problem, and the fact that the disagreement is quite small, it is not unlikely that MCG+10-13-030 is a bound satellite of NGC 2685.

#### NGC 660 and its Dwarf Companion, UGC 1195

##### Review of Published Observations of NGC 660

The galaxy NGC 660 has is described by Benvenuti, Cappacioli, and D'Odorico (1976) as an SBa P, with a blue apparent magnitude of 11.97. Its diameter, measured out to the 25 mag arcsec<sup>-2</sup> isophote on the Palomar Sky Survey plates, is 10'.0 × 4'.5 (Nilson, 1973). The Nearby Galaxies Catalogue (Tully, 1988) lists NGC 660's optical heliocentric velocity at 855 km s<sup>-1</sup>. The photograph of NGC 660 in Figure 3.18 shows a central bar-like structure crossed by two systems of absorption, as well as an outer ring or disk inclined about 50° with respect to the major axis of the central body. Spectra taken along the apparent equatorial dust lane (P.A. 30° - 33.5°), in H<sub>α</sub> and N II, reveal a fairly symmetric linear rotation curve up to 30'' from the center (Benvenuti et al., 1976). While no H<sub>α</sub> emission was detected beyond 30.5'' in the SW direction, in the NE direction, the velocity curve appears to flatten out and extends up to 73'' from the center (Benvenuti et al., 1976). Spectra taken along other position angles reveal that the kinematics of the galaxy can not be described simply in terms of circular motion. The radial velocity difference between extremes of the rotation curve is approximately 300 km s<sup>-1</sup> (Benvenuti et al., 1976).

Figure 3.18: The galaxy NGC 660. The image was obtained from an exposure using a plate with a III-aJ emulsion. North is at the top and East is to the left of North.  
Reproduced with permission from the Royal Observatory in Edinburgh, Scotland.



Table 3.9: Optical characteristics of NGC 660 and UGC 1195.

Optical Characteristics of NGC 660 and UGC 1195		
	NGC 660	UGC 1195
Right Ascension	<sup>b</sup> 01 <sup>h</sup> 40 <sup>m</sup> .3	01 <sup>h</sup> 39 <sup>m</sup> .7
Declination	13° 23'	13° 43'
Type	<sup>a</sup> SBa P	<sup>c</sup> Im P
Dimensions on PSS plate	<sup>c</sup> 10'.0 × 4'.5	<sup>c</sup> 3'.5 × 1'.1
Axial Ratio	<sup>a</sup> 0.46	<sup>b</sup> 0.36
Inclination [degrees]	<sup>a</sup> 63	<sup>b</sup> 75
$m_B$ [mag] <sup>d</sup>	<sup>a</sup> 11.97	<sup>b</sup> 12.5
$M_B$ [mag]	<sup>a</sup> -18.43	
$V_{\text{Helio}}$	<sup>b</sup> 856	<sup>b</sup> 767
$V_0$	<sup>b</sup> 982	<sup>b</sup> 895
Distance ( $H_0=75 \text{ km s}^{-1} \text{ Mpc}^{-1}$ )	13	12

<sup>a</sup> (Benvenuti et. al., 1976)<sup>b</sup> Catalogue of Nearby Galaxies (Tully, 1988)<sup>c</sup> Uppsala General Catalogue of Galaxies (Nilson, 1973)<sup>d</sup> The magnitude is not corrected for absorption.

<sup>e</sup> Adjusted for motion of 300 km s<sup>-1</sup> toward ( $l,b$ )=(90°, 0°); i. e.,  $V_0$  is with respect to the velocity centroid of the local group of galaxies

Radio continuum observations of the central 8" of the nucleus at 6-cm show three central peaks within an elongated, low surface brightness component that extends along P.A. 47°, over the entire length of the visible source (Condon, Condon, Gisler, and Puschell 1982). Spectral indices of  $\alpha(2380,4885 \text{ MHz})=0.68$  (Condon 1980) and  $\alpha(1413,4885 \text{ MHz})=0.6$  indicate the presence of both thermal and synchrotron emission, with the latter being the dominant component (Condon et al., 1982).

NGC 660 has the infrared signature of a starburst. Its integrated infrared flux densities, derived from IRAS observations, are  $S_{12\mu}=4.08 \text{ Jy}$ ,  $S_{25\mu}=9.14 \text{ Jy}$ , and  $S_{60\mu}=80.9$

Jy (Young, Xie, Kenney, and Rice 1989). The existence of polar rings, the nuclear structure, and the disturbed nature of this galaxy lends credence to the hypothesis that this is a post-merger system.

In the VLA HI observations of NGC 660 described below, a Dwarf galaxy, UGC 1195 was also detected about 22 arcminutes NW of NGC 660. Some important optical characteristics of both of these galaxies are listed in Table 3.9.

### VLA HI Observations

#### The observing runs for NGC 660

Observations of HI emission in the galaxy NGC 660 were made with the C and D array configurations of the VLA on December 11, 1986 and March 6, 1987, respectively. Each observing run was eight hours in duration and employed a maximum of 25 antennae at any given time. The quasar, 3C48 was used for band-pass, amplitude and phase calibration. Scans four to five minutes in duration were made of 3C48 at the beginning of each observing run, between each 40–60 minute scan of NGC 660, and at the end of each observing run. A bandwidth code of 4A, with on-line Hanning smoothing was specified for both observing runs. This corresponds to a total IF bandwidth of 3.125 MHz, four IF's with 32 channels per IF, and a channel separation of 97.656 kHz. Visibilities were averaged on-line every 30 seconds. Following each observing run, the data were filled into the DEC-10 data-base using a filler integration time of 60 seconds. The visibilities were edited and calibrated on the DEC-10 computer system. Further editing of the source data set to remove interference was done using the astronomical

Table 3.10: VLA observing parameters for NGC 660.

Parameters	NGC 660	
Array	C	D
Total Number of Antennas	25	25
Observing dates	86 Dec 11	87 Mar 6
Duration of Observations (hr)	8	8
Velocity of band center, heliocentric (km s <sup>-1</sup> )	855	855
Observing Mode	4A	4A
On-line Hanning Smoothing	yes	yes
Full Width Half Power of primary beam (')	32	32
Flux Calibrator 3C48 (Jy)	16.180	16.185
Phase Calibrator	0831+557	
Min. projected spacing (kλ)	0.12904	
Max. projected spacing (kλ)	15.993	
Field Center RA (1950)	01 <sup>h</sup> 40 <sup>m</sup> 20 <sup>s</sup> .8	
Field Center DEC (1950)	13° 23' 30".00	
Total Observing Bandwidth (MHz)	3.125	
Bandcenter (MHz)	1416.26	
Number of velocity channels	31	
Channel Separation (km s <sup>-1</sup> )	20.73	
Channel Separation (kHz)	97.656	
Channel velocity Resolution (km s <sup>-1</sup> )	24.876	
Total Visibilities in Combined Data sets used for mapping	226,608	

image processing software package, AIPS. The observational parameters for each observing run are summarized in Table 3.10.

#### Calibration and editing of the visibilities

The primary flux calibrator for both observing runs was 3C48, a VLA standard flux calibrator. The flux of 3C48, for the 20-cm band, was set at 16.180 Jy and 16.185 Jy for the C and D array observations, respectively. The time dependent amplitudes and phases were calibrated using data from channel zero which is an average of the central 75% of the 3.125 MHz passband. A least-squares antenna-based solution for the complex gains of each antenna was obtained from the average of the calibrator visibilities over each scan. A few baselines in each data set had visibilities associated with individual baselines that deviated from the antenna-based solution by more than 7% in amplitude or 5° in phase. These data were flagged and new antenna-based solutions were found for the complex gains. Fluxes were computed for the entire dataset via a boxcar interpolation in time, of the amplitude and phase gains of the individual antennae between consecutive antenna solutions. In order to calibrate the bandpass, the bandpass calibrator 3C48 was assumed to have a flat spectrum over the total spectral-line bandwidth. For each base line, the spectra were individually normalized by channel zero and vector averaged over the calibrator. The visibilities in the data-base were then corrected by dividing by the values computed above. Following calibration, the source visibilities were examined for time dependent errors and bad data were flagged.

It should be noted that the data from the D array run were significantly degraded by low level interference, presumably due to the sun. This interference manifested as ripples across maps constructed from the visibilities. Careful examination of the

Table 3.11: UV clip parameters.

UV CLIP PARAMETERS	
U-V Range [kλ]	Flux Cut-Off [Jy]
0 - 1	1.6
1 - 2	1.3
2 - 3	1.2

visibilities revealed a significant number of interference spikes for the shorter projected spacings. However, this interference could not be associated with any specific time, antenna, or baseline. Therefore, these data were clipped by setting flux limits for specific ranges in the  $uv$  plane. The  $uv$  limits and the associated flux cutoffs, above which value the data were clipped, are listed in Table 3.11.

#### Distribution of HI in NGC 660 and UGC 1195

The strong signal from NGC 660 made it possible to obtain high resolution maps of good quality. The visibilities from each observing run were combined prior to mapping. Maps were constructed using uniform weighting of the visibilities and no taper. A set of  $31, 512 \times 512$  channel maps with  $6'' \times 6''$  cells was produced by Fourier inversion using an FFT algorithm. Table 3.12 summarizes the principal map parameters.

In order to examine the line emission, continuum emission present in the 20-cm band must be subtracted from the maps. A pseudo continuum channel was constructed from an average of the channel maps on both sides of the observing band that appeared to be free of emission. Two channels at the edge of the observing band, 30 and 31, were very noisy and so were not used in the estimate of the continuum emission. The average continuum was subtracted from all of the maps and the resulting maps were examined for evidence of improper continuum subtraction.

Table 3.12: VLA, HI map parameters for NGC 660.

Final Maps	NGC 660
HPBW of Synthesized Beam for Maps with Uniform Weighting ["]	$14.43 \times 12.25$
Beam Position Angle [ $^{\circ}$ ]	-72.59
Visibility Taper [ $k\lambda$ ]	none
Map Dimensions [cells]	$512 \times 512$
Pixel Dimensions ["]	$6 \times 6$
RMS Noise in Channel Maps [mJy/Beam]	0.81
Equivalent $T_B$ [ $^{\circ}$ K]	2.8

The first attempt at continuum subtraction, with a continuum given by the average of channels 2–7 and 26–29, revealed the presence of line emission and absorption in channels 7, and absorption in channel 26. Thus, these two channels were excluded from the next estimate of the continuum.

Channels 2 and 31 also evidenced absorption and emission near map center. However, this is due to improper continuum subtraction, which results if the bandpass correction is not good at the edges of the band. To check the accuracy of the bandpass correction, spectra were produced through the pixels of the bright continuum sources assumed to have flat spectra over the band. The spectra revealed a marked drop in flux for the end channels, especially at the low velocity end of the spectrum. Hence, the features in channels 2 and 31 are probably a result of errors in the bandpass correction for the end channels. Even so, channel 2 was included in the estimate of the continuum since the absorption is only over two pixels, and it is of a low enough level that does not make a significant contribution to the continuum after averaging. Furthermore, since extended regions of emission in the galaxy are of primary interest here, the extra channel in the computation of the average continuum level over the map helps to reduce the noise level in the continuum subtracted maps.

Table 3.13: Noise statistics on VLA, HI channel maps of NGC 660.

Noise Statistics on Continuum Subtracted Line-Free Maps	
Uniformly Weighted Maps	
ch	r.m.s noise [mJy/Beam]
2	0.8507
3	0.8176
4	0.8179
5	0.8096
6	0.8298
27	0.7650
28	0.7517
29	0.8160
Average	0.8073

The continuum used for subtraction from the channel maps is the average of channels 2 to 6 and 27 to 29. Noise statistics for the line free maps following continuum subtraction are given below, in Table 3.13, with the average r.m.s. noise being 0.81 mJy/Beam. The total number of visibilities ultimately used for mapping corresponds to roughly 12.6 hours of time on NGC 660 which, by Equation (3.23), gives a theoretical noise limit for the uniformly weighted maps of roughly 0.72 mJy/Beam. Therefore, the r.m.s. map noise is just a little above that expected by the approximate theoretical estimate.

The continuum map as well as the line maps contain confusing sidelobes which are a result of the finite extent of and gaps in the *uv* coverage. These are removed by deconvolution using the CLEAN algorithm. The response of the combined arrays to a point source is given by the dirty beam produced for channel zero, where channel zero is an average of the response over the central 75% of the bandpass. The half-power dimensions of the synthesized beam, used to restore the clean components extracted by

CLEAN, are given by an elliptical gaussian fit to the central portion of the dirty beam. For the channel zero dirty beam, the fit gave a HPBW of  $14.^{\prime\prime}431 \times 12.^{\prime\prime}253$  and a major axis position angle of  $-72^{\circ}.59$ .

The continuum was cleaned down to the 1.8 mJy level after 618 iterations. On the clean continuum maps the r.m.s. noise level is 0.45 mJy/Beam. The main source of continuum in this map is the program galaxy NGC 660, which is displaced a little northeast of the pointing center of the observations. An elliptical gaussian fit to the innermost portions of the continuum emission gives a center for the emission peak of ( $01^{\text{h}} 40^{\text{m}} 21^{\text{s}}.6$ ,  $13^{\circ} 23' 43''$ ). This position agrees with the IR (Hawarden, 1992) and optical position of the galaxy to better than  $6''$ . As seen in Figure 3.19, the region of continuum emission is roughly elliptical in shape and extends along the projected major axis for nearly two arcminutes. Along the minor axis direction, it extends for about one arcminute. The position angle of the projected major axis of the continuum emission is  $45^{\circ} \pm 5^{\circ}$ , measured from North in the direction East.

Positions of the five continuum sources, other than NGC 660, detected in the 20 cm band are given in Table 3.14. One of these extends over about one arcminute, and two emission peaks are just resolved by these observations. It is located in the southwest at  $(\alpha, \delta) = (01^{\text{h}} 39^{\text{m}} 37^{\text{s}}.658, 13^{\circ} 12' 42''.77)$ , and is shown in Figure 3.20. The western peak of this source has a flux of 85.2 mJy/Beam.

The channel maps containing HI line emission were cleaned down to the  $2\sigma$  level or after 1200 iterations. In all cases where CLEAN was terminated by the iteration limit, the maximum residuals were less than  $3\sigma$ . Examination of these maps and their clean components indicated that no further cleaning was necessary.

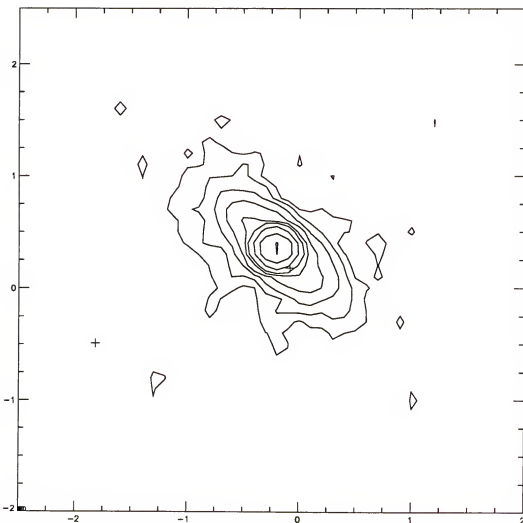


Figure 3.19: Continuum Emission at 20 cm from NGC 660 derived from maps made with uniform weighting of the visibilities. Contour levels are multiples of the r.m.s. noise level of the map,  $0.45 \text{ mJy/Beam}$ ; i. e.,  $\sigma \times [2, 5, 10, 20, 40, 60, 100, 200, 400]$ . The map maximum is  $185.72 \text{ mJy/Beam}$ . The spatial resolution of the maps is  $14''.43 \times 12''.25$ , with a beam position angle of  $-72^\circ.59$ . The "+" signs mark star positions for comparison with optical maps. Distances are in term of arcminutes from the pointing center of the observations. North is at the top of the map and East is to the left.

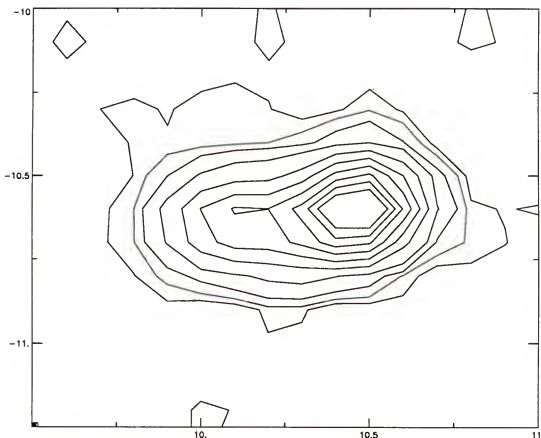


Figure 3.20: Continuum Emission at 20 cm from the double source in the SW part of the map of NGC 660. Contour levels are multiples of the r.m.s. noise level of the map, 0.45 mJy/Beam; i. e.,  $\sigma \times [2, 5, 10, 20, 40, 60, 100, 200, 400]$ . The peak of this source is 85.2 mJy/Beam. The spatial resolution of the maps is  $14''.43 \times 12''.25$ , with a beam position angle of  $-72^\circ.59$ . Distances are in terms of arcminutes from the pointing center. North is at the top of the map and East is to the left.

Table 3.14: Continuum sources in the VLA maps of NGC 660.

source	Positions and Fluxes of Detected Continuum Sources		Flux Density [mJy]
	$\alpha$	$\delta$	
	[h m s]	[ $^\circ$ ' "]	
NGC 660 (peak)	01 40 21.622	13 23 43.00	388.02
1	01 41 21.671	13 17 30.04	19.464
2	01 40 14.072	13 35 08.15	4.331
3	01 40 07.564	13 26 07.60	49.95
4	01 40 6.175	13 24 34.88	46.24
5	01 39 37.658	13 12 42.77	164.95

NGC 660 evidences HI emission for line of sight, heliocentric velocities ranging from  $689 \pm 10 \text{ km s}^{-1}$  to  $1042 \pm 10 \text{ km s}^{-1}$ . Absorption, present in the center of the galaxy, extends over an even greater velocity range: from  $648 \pm 10 \text{ km s}^{-1}$  to  $1042 \pm 10 \text{ km s}^{-1}$ . The absorption arises from a barely resolved region of HI clouds near the center of the galaxy which lies along the line of sight, and in front of the extended bright continuum emission of the galaxy (Figure 3.19). Each channel in which signal from NGC 660 was detected is shown in the contour maps in Figures 3.21 (a) to 3.21 (r). Broken lines in the contour maps indicate regions of absorption.

As can be seen in Figures 3.21 (a-r), NGC 660 evidences strong emission and deep absorption. The peak intensity in the HI channel maps is 19.77 mJy/Beam, which corresponds to a brightness temperature of 68.1 K. This peak occurs at a velocity of  $980 \pm 10 \text{ km s}^{-1}$  at a position of ( $01^{\text{h}} 40^{\text{m}} 21^{\text{s}}.21$ ,  $13^{\circ} 20' 49''$ ), as shown in Figure 3.21 (e). The peak absorption in the channel maps is  $-11.99 \text{ mJy/Bm}$ , which corresponds to a brightness temperature of  $-41.3 \text{ K}$ . As shown in Figure 3.21 (k), the absorption peak corresponds to the position of the peak in the continuum and occurs at a heliocentric velocity of  $855 \pm 10 \text{ km s}^{-1}$ .

Two kinematic components of the HI gas are evident in the channel maps. The first is an inner component which lies along a position angle of  $45^{\circ} \pm 5^{\circ}$ , measured from North in the direction East, to the side of the projected major axis with negative line of sight velocity, as obtained in a coordinate frame moving at the recessional velocity of the galaxy. This inner component has the same orientation as the major axis of the continuum emission, and roughly that of the equatorial dust band of the galaxy. The second component of the gas, which is associated with the outer, more polar ring of stars, has a projected major axis position angle of about  $-5^{\circ} \pm 5^{\circ}$ . Therefore, the projected major axis of the outer ring is inclined roughly  $50^{\circ}$  to the projected major axis of the

Figure 3.21: (a-r) Uniformly weighted, clean channel maps showing the distribution of HI in NGC 660. The mean line of sight, heliocentric velocity for each map is printed at the top. Contour levels are multiples of the approximate r.m.s noise of 0.81 mJy/Beam:  $\sigma \times [-25, -15, -10, -7, -5, -3, 3, 5, 7, 10, 15, 20, 25]$ . The spatial resolution of the maps is  $14''.43 \times 12''.25$  and the beam position angle is  $-72^\circ.59$ . The channel separation is  $20.73 \text{ km s}^{-1}$ , and the velocity resolution is  $24.876 \text{ km s}^{-1}$ . The pointing center for the observations,  $(\alpha, \delta)_{1950} = (01^h 40^m 20^s.8, 13^\circ 23' 30'')$ , corresponds to (0,0). Positions of stars in the optical image are marked with "+" signs. Minor tick marks are at 15 arcsecond intervals and major tick marks are labeled every two arcminutes from pointing center. North is at the top and West is to the right.

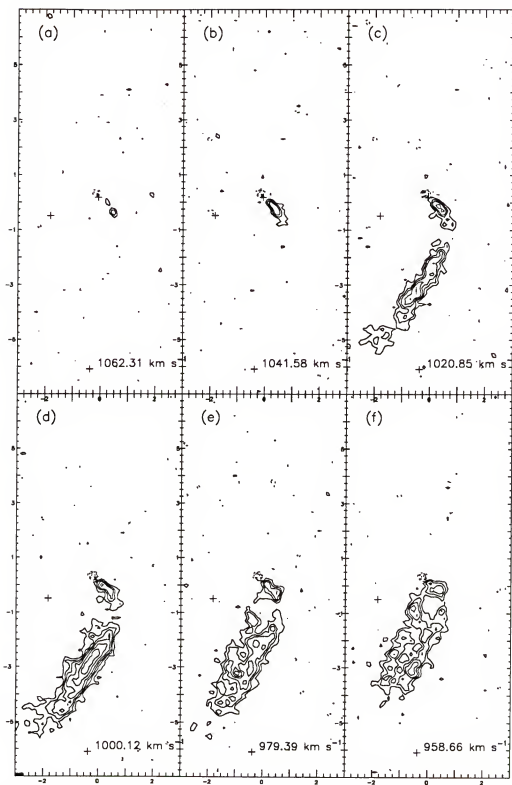


Figure 3.21: -- continued

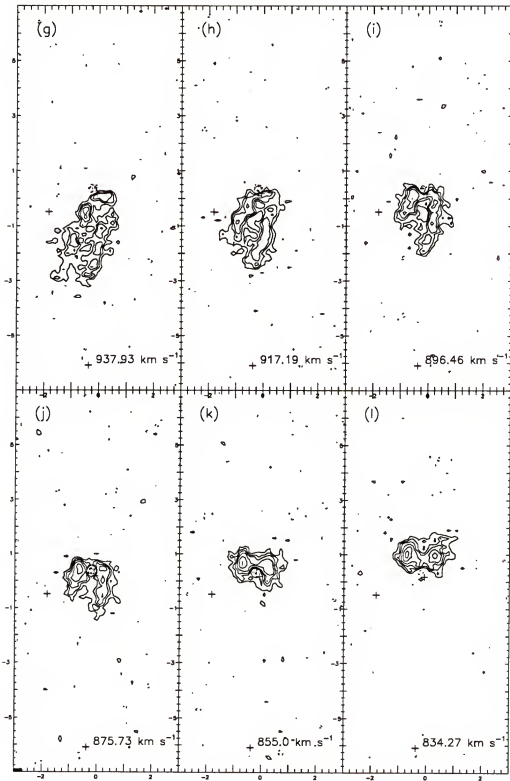


Figure 3.21: -- continued

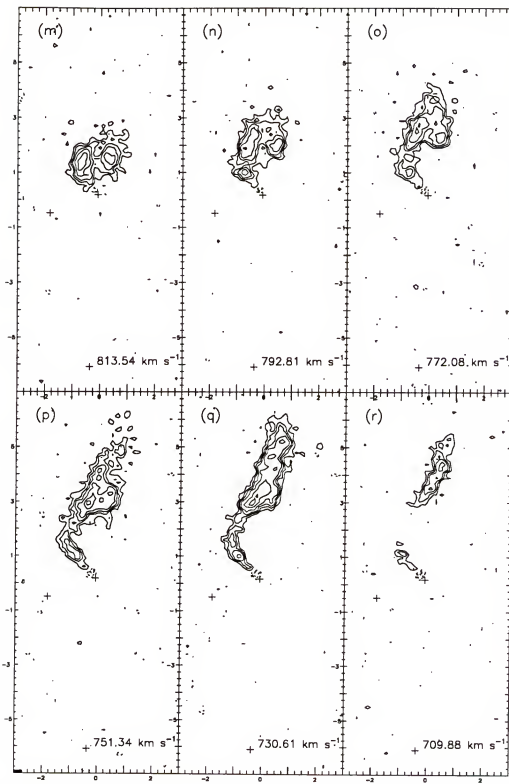


Figure 3.21: -- continued

inner ring, or  $40^\circ$  from a projected “polar” orientation. Though the gas appears to be clumpy, there is remarkable reflection symmetry of both the inner and outer rings about the center of the galaxy.

The global profile for NGC 660 is computed from a set of uniformly weighted maps that have been masked and corrected for primary beam attenuation in the same manner as discussed in Section 3. The masks were created by convolving the uniformly weighted map cube with an elliptical gaussian, giving a final HPBW of  $30'' \times 30''$ , and then Hanning smoothing in velocity using a triangular function with a width of three channels between first nulls. A flux cutoff of  $2.5\sigma$ , or 0.22 mJy/Beam, was applied to the pixels in the smoothed map cube, which was then used as a mask for the original map cube. The masked maps were then corrected for primary beam attenuation. The global profile for NGC 660 is given in Figure 3.22.

Moments of the radiation field for NGC 660 were computed from the same masked and primary beam corrected maps that were used to compute the global profile. Also, since the region of absorption is of interest, two sets of zeroth moments were computed: one for positive pixel values (emission) and the other for negative pixel values (absorption). Using  $982 \text{ km s}^{-1}$  as the corrected recessional velocity of the galaxy, the positive emission gives a total of  $3.74 \times 10^9 \times h^{-2} M_\odot$  of HI. For  $h=0.75$ , this corresponds to  $6.6 \times 10^9 M_\odot$  of HI.

A rough estimate of the mass of the absorbing gas is obtained as follows. First, the pixels evidencing absorption are integrated over velocity. Second, an average spin temperature ( $\bar{T}_S = 125 \text{ K}$ ) and an average continuum temperature ( $\bar{T}_C$ ) are assumed to apply over the absorbing region. The continuum map of NGC 660 indicates that  $155 \leq T_C \leq 640$  over the absorbing region. Third, given the assumption that the optical depth is small, the column density of the absorbing gas is proportional

to  $(\bar{T}_S/\bar{T}_C) \times N'_H(x, y)$ , where  $N'_H(x, y)$  is given by Equation 3.26. Given that  $0.80 \geq (\bar{T}_S/\bar{T}_C) \geq 0.19$ , the mass of the absorbing gas is obtained by integration over the absorbing region. In this manner the mass of the absorbing gas is estimated to be between  $7 \times 10^7 M_\odot \leq M_{HI(abs)} \leq 3 \times 10^8 M_\odot$ .

Maps of the integrated HI intensity and intensity-weighted mean velocity field of NGC 660 are given in Figures 3.23 and Figure 3.24. In Figure 3.23 there is an intense feature located along a position angle of  $45^\circ \pm 5^\circ$  measured, from North to East. This feature is associated with the narrow equatorial dust lane of the galaxy and will be referred to as the “inner” ring. The outer, more “polar” ring intersects the inner ring in the NE, along the line of sight where the peak observed brightness temperature is 68 K. At the outermost reaches of the galaxy there is a definite warp in the plane of the gas. Though the gas distribution appears to be a bit patchy, it is quite symmetric about the center of the galaxy. Furthermore, as shown in Figure 3.24, the velocity pattern of

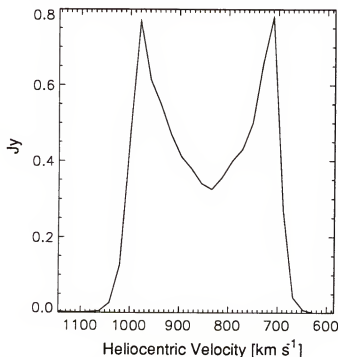


Figure 3.22: Global HI profile for NGC 660.

the gas, though complex in the innermost regions where the spectra are doubly peaked, is also quite symmetric and regular. Though rotation dominates, the velocity field is clearly not what one would expect for gas clouds executing purely circular orbits in a flat disk. A kinematic fit to the line of nodes gives a mean systemic velocity for the gas of  $842 \text{ km s}^{-1}$  and a major axis position angle for the inner component of  $46^\circ \pm 3^\circ$  (Gottesman and Mahon, 1990). Similarly a position angle of  $-7^\circ \pm 5^\circ$  is obtained for the major axis position angle of the outer ring; however, this position angle is not as well determined due to the warped nature of this component.

An axis velocity profile taken along the projected major axis of the inner ring, at a position angle of  $45^\circ$ , is shown in Figure 3.25. This figure clearly shows multiple peaks in the HI emission spectra, as well as the broad deep absorption of the strong continuum source at the galactic center. Another velocity profile taken along the apparent major axis of the outer ring, at a position angle of  $-5^\circ$ , is given in Figure 3.26. The absorption seen in both figures is deep ( $-41 \text{ K}$ ) and occurs over a broad range in velocity ( $394 \pm 14 \text{ km s}^{-1}$ ), exceeding the maximum velocity width of the HI seen in emission. Even though the absorption is just barely resolved spatially, the large velocity width of this component seems to indicate the presence of a rotating nuclear ring or disk.

The companion galaxy to NGC 660, UGC 1195, is located about 22.4 arcminutes NW of NGC 660. UGC 1195 is described in the Uppsala General Catalogue of Galaxies (Nilson, 1973) as an irregular, distorted, slightly arc-shaped galaxy that exhibits no spiral structure. As shown in Figures 3.27 (a-g), HI emission from UGC 1195 is evident in the channel maps between  $709.9 \text{ km s}^{-1}$  and  $834.3 \text{ km s}^{-1}$ . The gas at the high velocity end is in the SW and moves towards the NE for decreasing line of sight velocity. Due to attenuation by the response of the primary beam, the signal strength is about 22 percent of what it would be if the galaxy was located at the pointing center. These maps indicate

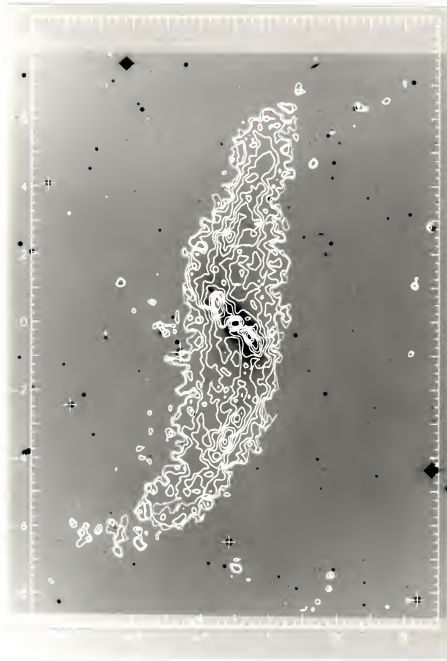


Figure 3.23: Integrated-intensity of HI in NGC 660 derived from uniformly weighted channel maps with a spatial resolution of  $14''.43 \times 12''.25$  and a velocity resolution of  $24.88 \text{ km s}^{-1}$ . Contours are shown over an optical (blue) image of the galaxy. North is at the top and East to the left. The small crosses indicate star positions. The maps are centered on the peak of the continuum emission, and axis labels are in units of arcminutes from the peak, which corresponds to the center of the galaxy. Owing to the presence of central absorption, there is a hole at the center of the map. Contour intervals are in fractions of the map maximum of  $1.56 \times 10^3 \text{ Jy/Beam} \times \text{m/s} \times [0.03, 0.05, 0.1, 0.2, 0.3, 0.4, 0.5, 0.6, 0.7, 0.8, 0.9, 1.0]$ . The map maximum corresponds to an HI column density of  $9.8 \times 10^{21} \text{ atoms cm}^{-2}$ .

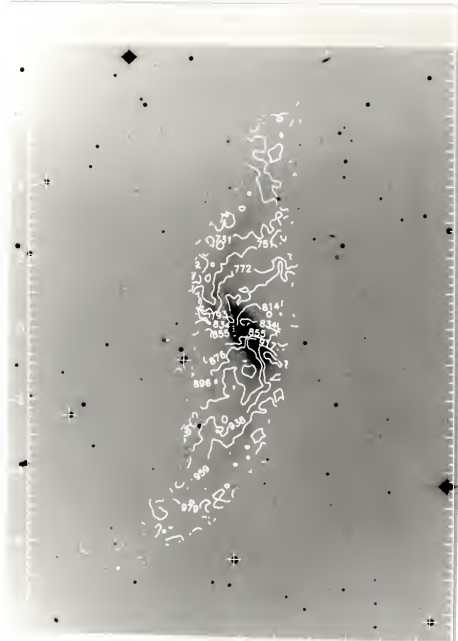


Figure 3.24: Intensity-weighted mean velocity of HI in NGC 660 derived from uniformly weighted channel maps with a spatial resolution of  $14''.43 \times 12''.25$  and a velocity resolution of  $24.88 \text{ km s}^{-1}$ . Contours are shown over an optical (blue) image of the galaxy. North is at the top and East to the left. The small crosses indicate star positions. The maps are centered on the peak of the continuum emission, and axis labels are in units of arcminutes from the peak, which corresponds to the center of the galaxy. Owing to the presence of central absorption, there is a hole at the center of the map. Contour labels are for mean heliocentric line of sight velocity in units of  $\text{km s}^{-1}$ .

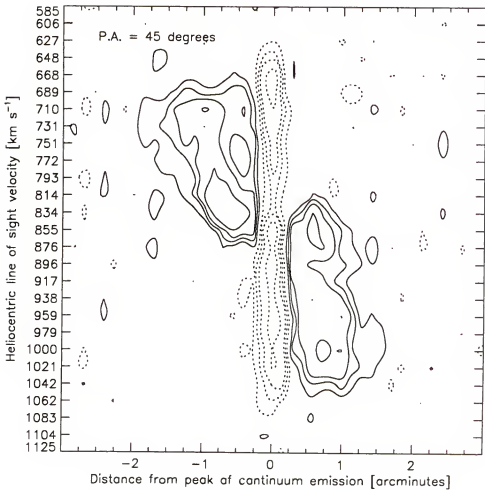


Figure 3.25: Velocity profile along the major axis of the inner ring, or equatorial dust lane, of NGC 660, for P.A. = 45°. The profile is derived from the uniformly weighted channel maps which have a spatial resolution of 14''.43 × 12''.25 and a velocity resolution of 24.88 km s<sup>-1</sup>. Contour levels are multiples of the r.m.s. map noise of 0.81 mJy/Beam:  $\sigma \times [-200, -150, -100, -50, -40, -30, -20, -10, -6, -4, -2, 2, 4, 6, 8, 10, 20, 30, 40, 50, 100, 150, 200]$ . Moving from left to right on the x-axis of the plot corresponds to moving from NE to SW along the projected major axis of the inner HI ring. The map is centered on the peak of the continuum emission. The position axis is labeled in arcminutes from the center of the galaxy and the velocity axis is for heliocentric line of sight velocity in km s<sup>-1</sup>.

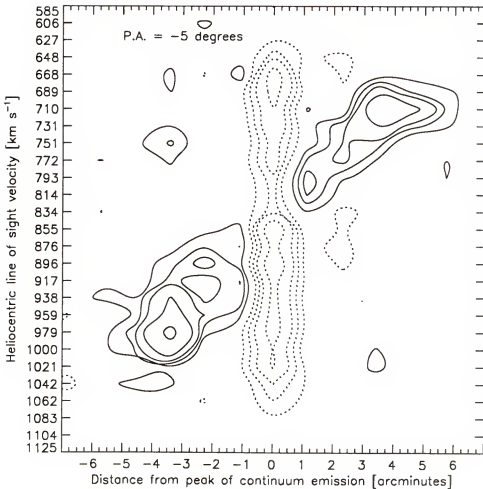


Figure 3.26: Velocity profile along the major axis of the outer, more polar ring of NGC 660, for P.A. =  $-5^\circ$ . The profile is derived from the uniformly weighted channel maps which have a spatial resolution of  $14''.43 \times 12''.25$  and a velocity resolution of  $24.88 \text{ km s}^{-1}$ . Contour levels are multiples of the r.m.s. map noise of  $0.81 \text{ mJy/Beam}$ :  $\sigma \times [-200, -150, -100, -50, -40, -30, -20, -10, -6, -4, -2, 2, 4, 6, 8, 10, 20, 30, 40, 50, 100, 150, 200]$ . Moving from left to right on the x-axis of the plot corresponds to moving from NW to SE, roughly along the projected major axis of the warped outer HI ring. The map is centered on the peak of the continuum emission. The position axis is labeled in arcminutes from the center of the galaxy and the velocity axis is for heliocentric line of sight velocity in  $\text{km s}^{-1}$ .

a total velocity width of  $124 \pm 14 \text{ km s}^{-1}$  and a mean systemic velocity of  $772 \pm 7 \text{ km s}^{-1}$ , corresponding to an observed radial velocity difference of  $70 \text{ km s}^{-1}$  between NGC 660 and UGC 1195.

In order to compute the global profile for UGC 1195, the masking maps were spatially smoothed to a resolution of  $20'' \times 20''$ , and then Hanning smoothed using

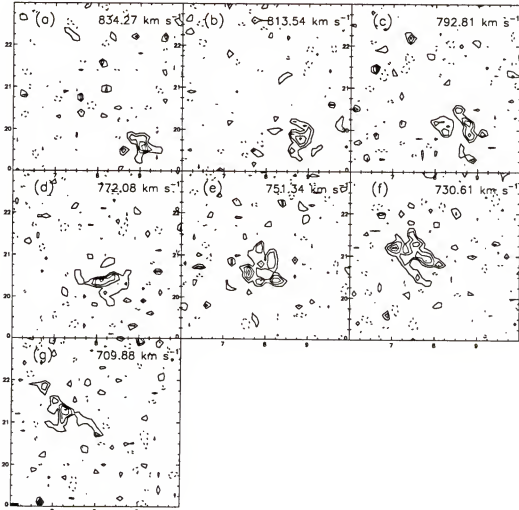


Figure 3.27: (a-g) Uniformly weighted, clean channel maps showing the distribution of HI in UGC 1195. The mean line of sight, heliocentric velocity for each map is printed at the top. Contour levels are multiples of the approximate r.m.s noise of  $0.81 \text{ mJy/Beam}$ :  $\sigma \times [-2, 2, 3, 4, 5, 6, 7, 8, 9]$ . The spatial resolution of the maps is  $14''.43 \times 12''.25$  and the beam position angle is  $-72^\circ.59$ . The channel separation is  $20.73 \text{ km s}^{-1}$ , and the velocity resolution is  $24.876 \text{ km s}^{-1}$ . The pointing center for the observations,  $(\alpha, \delta)_{1950} = (01^\mathrm{h} 40^\mathrm{m} 20^\mathrm{s}.8, 13^\circ 23' 30'')$ , corresponds to  $(0,0)$ . Minor tick marks are at 15 arcsecond intervals and major tick marks are labeled every two arcminutes from pointing center. North is at the top and West is to the right.

a triangular function with a width of three channels between first nulls. The masks were applied to the original map cube and a correction was made for primary beam attenuation. Figure 3.28 gives the global profile for UGC 1195.

The zeroth and first moments of the radiation field for UGC 1195 are given in Figure 3.29 (a-b). As shown in 3.29 (a), the HI appears to be unevenly distributed, and rather clumpy. The rotation of the galaxy is clearly visible in the velocity map shown in 3.29 (b).

The total amount of HI detected in UGC 1195 is determined by integration of the zeroth moment over the source. Assuming that UGC 1195 is at the same distance as NGC 660 ( $9.82 \times h^{-1}$  Mpc) a total HI mass for UGC 1195 of  $5.73 \times 10^8 \times h^{-2} M_{\odot}$  is obtained.

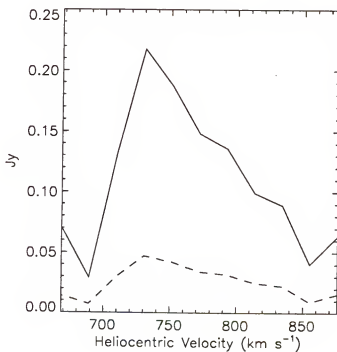


Figure 3.28: Global HI profile for UGC 1195. The solid line gives the profile obtained from maps corrected for primary beam attenuation, while the dotted line gives the profile from maps that were not corrected for attenuation by the primary beam.

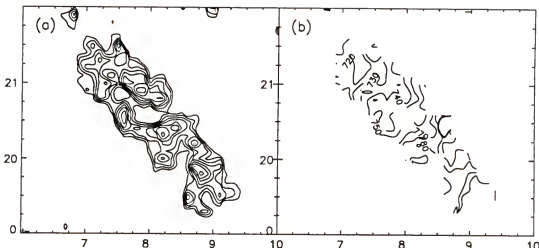


Figure 3.29: Moment maps of UGC 1195 derived from uniformly weighted channel maps with a spatial resolution of  $14''.43 \times 12''.25$  and a velocity resolution of  $24.88 \text{ km s}^{-1}$ . North is at the top and East to the left. Axis labels are in units of arcminutes from pointing center. (a) Integrated-intensity of HI for UGC 1195. Contour intervals are in fractions of the map maximum of  $0.99 \text{ Jy Beam}^{-1} \text{ km s}^{-1} \times [.2, .3, .4, .5, .6, .7, .8, .9, 1.0]$ . (b) Intensity-weighted mean velocity field of UGC 1195. Contour labels are for mean heliocentric line of sight velocities in units of  $\text{km s}^{-1}$ .

A summary of the HI characteristics of NGC 660 is given in Table 3.15, while Table 3.16 gives a similar summary for UGC 1195.

Table 3.15: HI characteristics of NGC 660.

NGC 660	Inner Ring	Outer Ring
Major Axis Position angle [degrees] <sup>a,c</sup>	$46 \pm 3$	$-7 \pm 5$
Approximate Radius [arcminutes]	1.8	6.5-7.0
Observed HI velocity width [ $\text{km s}^{-1}$ ]		$352 \pm 14$
Total mass of HI (emission only) [ $M_{\odot}$ ] <sup>b</sup>		$3.74 \times 10^9 \times h^{-2}$
Systemic velocity of HI gas [ $\text{km s}^{-1}$ ] <sup>c</sup>		$842 \pm 6$

<sup>a</sup> Measured from North to East to the side of the projected major axis that has negative line of sight velocity in a frame receding with the galaxy.

<sup>b</sup> Assumed distance of  $9.82 \times h^{-1} \text{ Mpc}$

<sup>c</sup> Kinematically determined

Table 3.16: HI characteristics of UGC 1195

UGC 1195	
Diameter [arcminutes]	$4.0 \pm 0.1$
Mean systemic velocity of HI gas $\langle v_{sys} \rangle$ [km s <sup>-1</sup> ]	$772 \pm 7$
HI velocity width [km s <sup>-1</sup> ]	$124 \pm 14$
Total HI mass [ $M_\odot$ ]	$5.73 \times 10^8 \times h^{-2}$
Distance <sup>a</sup> [Mpc]	$9.82 \times h^{-1}$

<sup>a</sup> Assumed to be at the same distance as NGC 660

A lower limit estimate of the mass of NGC 660 required to bind UGC 1195 can be obtained from Equation (3.31) if unknown projection effects are ignored. Thus, the escape velocity can be taken as the radial velocity separation of the galaxies, which is about 87 km s<sup>-1</sup>. At a distance of  $9.8 \times h^{-1}$  Mpc, the 22.4 arcminute separation of the galaxies corresponds to a linear separation of  $64 \times h^{-1}$  kpc. Given these quantities and ignoring projection effects, Equation (3.31), indicates a binding mass for the system of  $5.6 \times 10^{10} \times h^{-1} M_\odot$ . This is significantly less than the Keplerian estimate for the mass of NGC 660 of  $1.4 \times 10^{11} \times h^{-1} M_\odot$ , obtained by taking the inclination of NGC 660 to be 63° at a radius of 6.5 arcminutes or 18 × h<sup>-1</sup> kpc, and by taking the component of the circular velocity along the line of sight at this radius to be 160 km s<sup>-1</sup>. Likewise, the Keplerian mass for UGC 1195 is  $5.5 \times 10^9 \times h^{-1} M_\odot$ , given an assumed distance of  $9.82 \times h^{-1}$  Mpc, an inclination of 75°, and a line of sight circular velocity component equal to 62 km s<sup>-1</sup> at a radius of  $5.7 \times h^{-1}$  kpc. Since the mass of NGC 660 is in excess of the mass required to bind the system, UGC 1195 is probably a bound satellite of NGC 660.

## CHAPTER 4 MODELS

### Construction of Model Density and Velocity Fields

As discussed in Chapter 3, VLA maps of neutral hydrogen gas in the galaxies NGC 660 and NGC 2685 show that a significant portion of the gas is orbiting at high inclination ( $i > 50^\circ$ ) with respect to the central stellar disk of each galaxy. Moreover, gas in the inclined rings of these galaxies is observed to be rotating in the same sense as the stars (Benvenuti, Capaccioli, and D'Odorico, 1976; Schechter and Gunn, 1978; Shane, 1980; Gottesman and Mahon, 1990; and Whitmore, Lucas, McElroy, Steiman-Cameron, Sackett, and Olling, 1990). The principal aim of this research is to determine if the observed density and velocity fields of these galaxies, as derived from VLA observations of neutral hydrogen, can be modeled by a suitably weighted ensemble of stable, noncrossing periodic orbits in a rotating triaxial potential. This section describes the construction of an ensemble of orbits for a given model, projection of these orbits into an appropriate viewing orientation for comparison with VLA, HI observations, and weighting of the orbits by the observed surface density of HI.

In a triaxial potential rotating about its short axis, the stable anomalous family of inclined orbits is retrograde in the rotating frame of the potential, while in a triaxial potential rotating about its long axis, this family of orbits is prograde. Thus, for galaxies such as NGC 660 and NGC 2685, in which the stars or gas appear to rotate in the same

prograde sense, a potential rotating about its long axis, which gives prograde inclined orbits, is of particular interest. Hence, the focus of this chapter is on models constructed from orbits calculated in triaxial potentials that rotate about the long axis. Figure 4.1 (a-f), shows a set of orbits from the inclined anomalous family as seen from six different viewing orientations: down the intermediate axis (edge on), down the short axis, down the rotation axis, and for three other arbitrary orientations. Models generated from orbits in potentials rotating about their short axes could also be considered in the same way, as these may be of interest for cases of galaxies in which the gas is observed to be in retrograde rotation with respect to the stars.

The first step in the construction of an orbit model is to find the closed, periodic orbits in the corotating reference frame of a rotating triaxial potential for which the  $z$ -axis is the rotation axis, as well as the long axis of the potential. Consider a potential of the form given by Equation (2.1). For a given set of parameters  $V_c, R_c, q_a, q_b, q_c$ , and  $\Omega$ , the

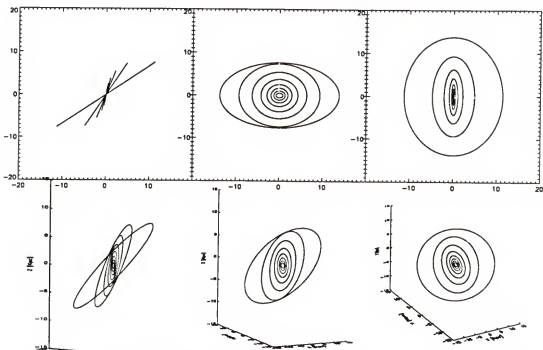


Figure 4.1: An ensemble of stable anomalous orbits as seen from various viewing orientations.

major families of stable periodic orbits in the bifurcation sequence containing the stable anomalous orbits are found, and their stability characteristics over a specified range in  $H$  are determined. If the potential is rotating about its short axis, the orbit families of interest are as follows: the z-axis family of radial orbits; the inclined family of retrograde, stable anomalous orbits; and the normal family of retrograde orbits in the plane perpendicular to the tumble axis of the potential (Heisler, Merritt, and Schwarzschild, 1982). On the other hand, if the long axis of the potential is the rotation axis, the families of interest are as follows: the z-axis family of radial orbits; the prograde family of elliptical orbits in the equatorial plane ( $E_p$ ); the inclined family of prograde, stable anomalous orbits; and the family of prograde elliptical orbits in the equatorial plane ( $E_{p-a}$ ).

The stability characteristics of the inclined family of stable anomalous orbits in rotating triaxial potentials are investigated extensively in Chapter 2. For the models considered here, where the rotation axis is the long axis of the potential, the stability of the main families of periodic orbits in the bifurcation sequence containing the inclined family of prograde, stable anomalous orbits is of particular interest. Such information is crucial if one is to construct an ensemble of orbits from which a model of the observed distribution and velocity of gas in a galaxy can be derived. Given this information, projected density and velocity fields can be constructed from an ensemble of initial conditions for stable periodic orbits over a selected range in  $H$ .

For a potential of given shape and rotation speed, orbits in each stable periodic family are computed and their stability and orbital characteristics are determined over a specified range in  $H$ . An ensemble of stable, closed periodic orbits is then constructed from the orbits in these families by assembling initial conditions over equal intervals in  $H$ . Since gas clouds in an equilibrium configuration will follow nonintersecting streamlines, none of orbits in a given ensemble of orbits are allowed to cross. Selections

from each family are made over specific energy ranges in such a way that each value of  $H$  corresponds uniquely to a single orbit. This constraint makes it possible to later weight the orbits using a weighting function that is a polynomial in  $H$ . The coefficients of this weighting function are determined by least squares fitting of the projected orbit density to the observed distribution of HI in the candidate galaxies. The construction of projected density and velocity fields for these orbits is discussed below.

First, given an ensemble of initial conditions for orbits belonging to a particular family, with each orbit corresponding to a unique value of  $H$ , but for arbitrary intervals in  $H$ , we derive a set of approximate initial conditions for this ensemble, at equal intervals in  $H$ , by cubic spline interpolation over the ensemble. In practice, if the original set of initial conditions is adequately sampled over the entire range of stability, the interpolated values of the initial conditions for orbits in that family in general will be very close to the true values for the periodic orbit. Improved values for the initial conditions, as well as the corresponding values of the stability parameters are then obtained from these approximate initial conditions.

Second, each orbit in the ensemble is integrated, with equal time steps, over exactly one orbital period. For every  $N$  time steps during the integration, where  $N$  is fixed for the ensemble, the corresponding position and velocity vectors for the orbit are transformed to an inertial coordinate frame, projected into an appropriate viewing orientation and binned in position and velocity. The projection, as discussed below, is effected through three rotations and a reflection. The reflection puts the coordinates into the left-handed reference frame of a hypothetical observer in which the positive  $X_o$ ,  $Y_o$  and  $Z_o$  axes point West, North, and along the observer's line of sight to the galaxy, respectively. Thus, positive radial velocities with respect to the central systemic velocity of the galaxy are to be interpreted as recessional, in keeping with the observer's convention.

Projection of the Model onto the Plane of the Sky

Orientation of the model with respect to a hypothetical observer involves rotations in three angles,  $\alpha$ ,  $\beta$ , and  $\gamma$ , and one reflection. For calculation of the projection equations consider the right-handed coordinate frame of the model for which the  $Z_m$ -axis is the figure rotation axis, and a right-handed coordinate frame for the sky in which the positive  $X_s$ ,  $Y_s$ , and  $Z_s$  axes point West, North and along the line of sight from the galaxy to the observer. All rotations are positive (counterclockwise) in a right-handed sense. In the following notation, coordinate axes are primed after each rotation. The transformation, for subsequent rotations on the  $Z_m$ ,  $X'_m$ , and  $Z''_m$  axes, respectively, is given by

$$\vec{X}_s = R_3(\gamma) R_1(\beta) R_3(\alpha) \vec{X}_m, \quad (4.1)$$

where

$$R_3(\alpha) = \begin{bmatrix} \cos \alpha & \sin \alpha & 0 \\ -\sin \alpha & \cos \alpha & 0 \\ 0 & 0 & 1 \end{bmatrix}, \quad (4.2)$$

$$R_1(\beta) = \begin{bmatrix} 1 & 0 & 0 \\ 0 & \cos \beta & \sin \beta \\ 0 & -\sin \beta & \cos \beta \end{bmatrix}, \quad (4.3)$$

and

$$R_3(\gamma) = \begin{bmatrix} \cos \gamma & \sin \gamma & 0 \\ -\sin \gamma & \cos \gamma & 0 \\ 0 & 0 & 1 \end{bmatrix}. \quad (4.4)$$

The rotation angles are as defined as follows: The angle  $\alpha$  is the angle from the  $X_m$  axis to the  $X'$  axis as measured in the  $X_m, Y_m$  plane; the inclination angle  $\beta$  is the angle between the  $Z'_m$  axis, which corresponds to the rotation axis of the potential, and the  $Z_s$  axis, which lies along the line of sight from the galaxy to the observer; and the third angle  $\gamma$  is a position angle which is measured in the plane of the sky from the  $X''_m$  axis to the positive  $X_s$  axis in the West. Note that the  $X''_m$  axis lies along the line of

intersection of the  $X_m, Y_m$  plane with the plane of the sky, corresponding to the “line of nodes” for a circular orbit in the equatorial plane of the potential.

Positions in the observer’s reference frame as derived from the transformation above are as follows:

$$\begin{aligned} X_s &= X_m(\cos \alpha \cos \gamma - \sin \alpha \cos \beta \sin \gamma) \\ &\quad + Y_m(\sin \alpha \cos \gamma + \cos \alpha \cos \beta \sin \gamma) \\ &\quad + Z_m \sin \beta \sin \gamma, \end{aligned} \tag{4.5}$$

$$\begin{aligned} Y_s &= -X_m(\cos \alpha \sin \gamma + \sin \alpha \cos \beta \cos \gamma) \\ &\quad + Y_m(\cos \alpha \cos \beta \cos \gamma - \sin \alpha \sin \gamma) \\ &\quad + Z_m \sin \beta \cos \gamma, \end{aligned} \tag{4.6}$$

and

$$\begin{aligned} Z_s &= X_m \sin \alpha \sin \beta - Y_m \cos \alpha \sin \beta \\ &\quad + Z_m \cos \beta. \end{aligned} \tag{4.7}$$

Velocities in the observer’s reference frame are similarly obtained. Finally, a reflection is required to convert from coordinates in the right-handed coordinate frame of the sky ( $\vec{X}_s$ ) to those in the left-handed coordinate frame of the observer,  $\vec{X}_o$ . This essentially corresponds to a change in the sign of all position and velocity components in the  $Z_s$  direction.

Observationally, one measures the Doppler shift of spectral line radiation emitted by gas clouds which have a component of their velocity directed along the observer’s line of sight. Traditionally, observed “radial” velocities are defined so that a positive observed “radial” velocity is directed away from the observer’s line of sight. Thus the “observed” velocity of a cloud in an orbit computed for a specific model is given by

$$\dot{Z}_o = -\dot{X}_m \sin \alpha \sin \beta + \dot{Y}_m \cos \alpha \sin \beta - \dot{Z}_m \cos \beta. \tag{4.8}$$

At the beginning of the modeling process, it is important to determine approximate values for the projection parameters. Thus, a simple method for deriving an approximate velocity field is described below. This method is used to determine good starting values for the projection angles, before attempting to quantitatively fit the model to the observations.

First, the positions and velocities over each orbit in the ensemble are calculated for equal time steps over exactly one orbital period. The positions and velocities are then projected into the observer's reference frame, the "observed" radial velocities ( $\dot{Z}_o$ ) are binned into map cells of a specified linear size, and all of the radial velocities in a particular cell are averaged. A map showing the isovelocity contours is then produced. Such velocity maps are produced for various values of the projection angles and compared to VLA velocity maps. The orientation of the observed galaxy, as well as gross features of the VLA velocity maps are used as criteria to restrict the acceptable range of the projection parameters for a particular model. For a given model, only the angles  $\alpha$  and  $\beta$  have any effect on the shape of the velocity contours, since  $\gamma$  is simply a position angle measured in the plane of the sky.

#### Weighting the Orbits with the Integrated-Intensity of HI

Once good approximate values for the projection parameters have been determined for a particular model one can proceed to the detailed fitting process which involves weighting of the orbits by the observed integrated-intensity of HI. To do this, it is assumed that the number of points in each cell from a given orbit is some function of the value of the Hamiltonian,  $H$ . For simplicity, this weighting function is assumed to

take the form of a polynomial. The coefficients of the weighting function are determined by a least squares fit to VLA maps of the integrated-intensity of HI as described below.

For a given set of projection parameters, each orbit in the ensemble is integrated for exactly one orbital period using equal time steps in the integration. This latter criterion is important, since the density of points computed along an orbit's path over a single orbital period is assumed to correspond to the density of stars or clouds distributed evenly along that orbit; i.e., regions where the orbits spend more time will be more densely populated. The positions and velocities are transformed to coordinates in the observer's reference frame. Each projected point is then binned into a cell in a three-dimensional array, or model map cube,  $M(X_o, Y_o, \dot{Z}_o)$ . Since this analysis entails a quantitative comparison of moment maps derived from  $M$ , to moments derived from a similar VLA map cube, the linear cell sizes and channel velocity widths for  $M$  are set by the angular cell size and velocity resolution of the VLA maps. During the projection and binning process, if any projected position or velocity falls outside of the range of the map cube as defined by the cube of observed maps, this orbit and all of its projected points are eliminated from the ensemble.

Therefore, if  $N_k$  is defined as the total number of points calculated for the  $k$ th orbit,  $n_{ijkl}$  as the number of points in the cell  $M(i, j, l)$  due to the  $k$ th orbit,  $w$  as the polynomial weighting function of order  $m$ , and  $N_{orb}$  as the total number of orbits in the ensemble, then the total number of points in each cell summed over all of the orbits in the ensemble,  $F_{ijl}$ , is given by

$$F_{ijl} = \sum_{k=1}^{N_{orb}} w_k \cdot \frac{n_{ijkl}}{N_k} \quad (4.9)$$

where  $w_k = a_0 + a_1 \cdot H_k + a_2 \cdot H_k^2 + \dots + a_m \cdot H_k^m$ . The coefficients of  $w$  are determined from a linear least squares fit of the basis functions from the matrix  $F$  to the zeroth

moment of the VLA cube (the integrated-intensity map), where

$$F_{ij} = \Delta v \sum_{l=1}^{nch} F_{ijl} \quad (4.10)$$

$nch$  is the number of model channel maps, and  $\Delta v$  is the velocity separation of the channels. The least squares solution employs the method of singular value decomposition as described by Press, Flannery, Teukolsky, and Vetterling (1986, Chapter 14). Given the coefficients of  $w$ , the weighted flux in each element in the model map cube is obtained from Equation (4.9). A weighting function derived for an ensemble of orbits is valid only over the range of  $H$  covered by the ensemble.

For a weighting function derived from such an analysis to be valid, it must not give negative weight to any orbit since that would imply a negative density. Therefore, every weighting function derived from these calculations must be carefully checked for validity. If a negative weighting results for the innermost orbits, these orbits can be eliminated from the ensemble and a new solution obtained for a model which will then have a higher value for the minimum  $H$ . Otherwise, the only consistent way to get around this problem, without disrupting the constraint that the initial conditions be for equal intervals in  $H$ , is through adjustment of parameters and recalculation of the weighting function until a physically viable result can be obtained.

#### Moments of the Model Radiation Field

Prior to calculating the moments of the model radiation field, the model maps in the weighted cube are corrected for the response of the VLA antenna beam. Therefore, each map in the cube is convolved with a synthesized elliptical gaussian “beam” derived from a least squares fit of an elliptical gaussian to the response of the VLA to a point source. The zeroth and first moments of the model radiation field,  $M0$  and  $M1$  are then

computed as defined below.

$$M0(i, j) = \Delta v \cdot \sum_{l=1}^{nch} M(i, j, l), \quad (4.11)$$

and

$$M1(i, j) = \frac{\sum_{l=1}^{nch} v_l \cdot M(i, j, l)}{\sum_{l=1}^{nch} M(i, j, l)}. \quad (4.12)$$

The zeroth moment gives a map of the integrated-intensity, while the first moment gives a map of the intensity-weighted mean velocity along the observer's line of sight. These maps can be subtracted from their observed counterparts for examination of the residuals to help determine which parameters (projection angles, shape parameters, or rotation speed) need to be adjusted to improve the model.

Only stable orbits in the SAO and  $E_p$ -a families are considered in the models discussed below. One reason for this restriction is that the resolution of the observations is too low to allow for appropriate weighting of the stable, low  $H$  orbits from the  $E_p$  family inside of a core radius. Thus, for an ensemble of orbits from the SAO and  $E_p$ -a families, the lower limit to  $H$  is set by the bifurcation of the SAO family of orbits from the  $E_p$  family inside the core radius. Another reason is that, for the particular models considered here for NGC 2685 and NGC 660, orbits in the  $E_p$  family do not appear to become stable again over the range of  $H$  of interest; however, a complete study of this family has yet to be done. The upper limit to  $H$  is set by either the constraint that no orbits in an ensemble can cross (here, this applies to the high  $H$  orbits of the  $E_p$ -a family), or by observationally imposed constraints (such as the maximum observed radial velocity). Since these orbits will later be weighted according to a polynomial in  $H$ , the ensemble must be further constrained so that there is only one orbit associated with each value of  $H$ . This constraint must be explicitly imposed whenever stable branches of both the  $E_p$ -a and SAO families exist over the same interval in  $H$ .

Models of NGC 660 and NGC 2685General Considerations

Before beginning quantitative modeling, it is important to determine an appropriate set of starting parameters. In particular, for a given set of model parameters ( $q_a$ ,  $q_b$ ,  $q_c$ ,  $\Omega$ ), one needs to know where the anomalous orbits join the equatorial plane, the maximum distance above the equatorial plane that can be achieved by any one of the orbits in the ensemble, and the run of the orbit axial ratios with increasing  $H$ . Furthermore, for the elliptical family of orbits in the equatorial plane  $E_p-a$ , one needs to know the maximum radial extent that can be achieved by these orbits before the orbits of higher energy start to cross those of lower energy. Since gas streamlines cannot be allowed to cross in an equilibrium configuration, this value sets the upper limit on the maximum radial extent possible for each model.

Consider Figure 4.2 in which stable anomalous orbits in potentials of two different shapes are considered for three different values of  $\Omega$ : 1.0, 2.0, and  $3.0 \text{ km s}^{-1} \text{ kpc}^{-1}$ . For these six sets of model parameters, the maximum height above the plane achieved by the stable anomalous orbits is plotted against the maximum radial extent of each orbit. Distances are given in kiloparsecs. The solid lines are for a potential with shape parameters  $(q_a, q_b, q_c) = (0.95, 0.92, 1.00)$ , and the dotted lines are for a potential with  $(q_a, q_b, q_c) = (0.90, 0.92, 1.00)$ . Each curve is labeled with the corresponding value of  $\Omega$ .

Now, for the same models consider the minor to major axis ratio of the orbits as a function of maximum radial extent. In Figure 4.3, as  $R$  increases from the left, the orbits, which are initially very elongated, approach a circular orbit, which corresponds to an axial ratio of one. To the left of this point the major axes of the anomalous orbits are

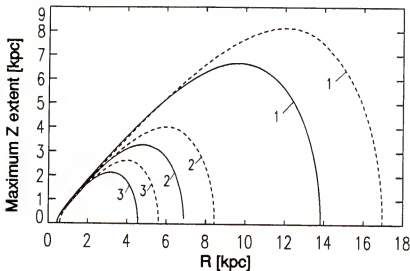


Figure 4.2: The maximum z-extent above the equatorial plane for orbits in the stable anomalous family as a function of the orbit's maximum radial extent. The solid lines are for orbits computed from the model with  $(q_a, q_b, q_c) = (0.95, 0.92, 1.00)$ , while the dotted lines correspond to the model with  $(q_a, q_b, q_c) = (0.90, 0.92, 1.00)$ . Each line is labeled with the corresponding value of  $\Omega$  for that potential.

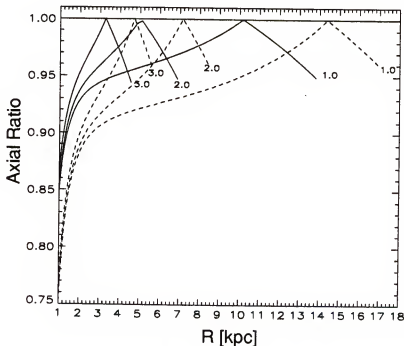


Figure 4.3: The minor to major axis ratio of orbits in the stable anomalous family as a function of the major axis length. The solid lines are for orbits computed from the model with  $(q_a, q_b, q_c) = (0.95, 0.92, 1.00)$ , while the dotted lines correspond to the model with  $(q_a, q_b, q_c) = (0.90, 0.92, 1.00)$ . Each line is labeled with the corresponding value of  $\Omega$  for that potential.

aligned with the intermediate axis of the potential. To the right of this point, the direction of elongation of the orbits changes, so that upon joining the  $E_p$ —a family in the equatorial plane, the major axes of the SAOs are aligned with the short axis of the potential.

In order to compare models to the observations a linear scale needs to be determined for the VLA maps. This requires that one assume a distance to the galaxy under consideration. For distant galaxies such as NGC 2685 and NGC 660, the distance, to within a factor of two, must be determined using Hubble's law. Hubble's law gives the distance to the galaxy as a function of its recessional velocity due to the overall expansion of the universe; i.e.,  $v_0 = H_0 r$ , where  $v_0$  is the recessional velocity of the galaxy and  $H_0$  is Hubble's constant. The value of Hubble's constant is not very well determined and ranges in the literature between values of 50 and 100  $\text{km s}^{-1}\text{Mpc}^{-1}$ . For the models discussed below, an intermediate value of  $75 \text{ km s}^{-1} \text{ Mpc}^{-1}$  is assumed. The recessional velocities quoted below for NGC 2685 and NGC 660 are relative to the velocity centroid of the Local Group of galaxies and are derived from the heliocentric recessional velocity of each galaxy by correcting for solar motion of  $300 \text{ km s}^{-1}$  towards galactic coordinates  $(l, b) = (90^\circ, 0^\circ)$  (see de Vaucouleurs, de Vaucouleurs, and Corwin 1976, p. 49).

### Models of NGC 2685

The corrected recessional velocity for NGC 2685 is  $965 \text{ km s}^{-1}$ , which corresponds to distance of  $12.9 \text{ Mpc}$ . This gives a linear scale of  $0.56 \text{ kpc}$  over  $9''$ , the width of a single cell on the naturally weighted HI maps. If the galaxy is at a greater distance than this, then models with slightly lower rotation rates would be in order. Thus, the value obtained for the rotation rate of the potential based on fits to the observed density and

velocity structure of the gas, depends critically on how well the distance to the galaxy is known, since this controls the linear scale of the problem. As long as the rotation rates for a model are far away from the critical values where qualitative changes occur in the system, one can obtain a set of initial conditions for a new model simply by changing the value of  $\Omega$  by a small amount and computing a new set of initial conditions, using the initial conditions from the old set as starting values.

In order to choose a good starting model for this galaxy consider the curves of Figure 4.2 and the observed extent of the inner HI rings of NGC 2685 given in Table 3.7. For an adopted distance of 12.9 Mpc the maximum extent for the inner ring is 6.4 kpc. As shown in Figure 4.2, a maximum  $z$ -extent within this range can be obtained with a model with shape and rotation somewhere between  $(q_a, q_b, q_c, \Omega) = (0.95, 0.92, 1.00, 1.00)$  and  $(q_a, q_b, q_c, \Omega) = (0.90, 0.92, 1.00, 1.00)$ , with the former appearing to be the better choice because the orbits join the equatorial plane with a lower maximum radial extent.

Given the set of initial conditions corresponding to the model for which  $(q_a, q_b, q_c, \Omega) = (0.95, 0.92, 1.00, 1.00)$ , the next step is to determine a good set of projection parameters. The observations indicate a position angle for the outer ring of about  $35^\circ$ , measured from North in the direction East. Table 3.1 gives an inclination for the stellar disk of the galaxy of  $62^\circ$ . If the outermost ring of HI is elliptical and lies in the equatorial plane defined by the stellar disk, then the only unknown angle here is the angle that gives the orientation of the major axis of the elliptical disk to the observer. This latter angle corresponds to the projection angle  $\alpha$  in the notation of Equation (4.1). Thus, adopting the values of  $62^\circ$  and  $-125^\circ$  for  $\beta$  and  $\gamma$ , a set of unweighted projected density and velocity maps is produced for various values of  $\alpha$ .

Figure 4.4 shows the projected density and velocity structure for  $\alpha = 40^\circ, 60^\circ$ , and  $80^\circ$ , respectively. In these diagrams notice the central density enhancement which is

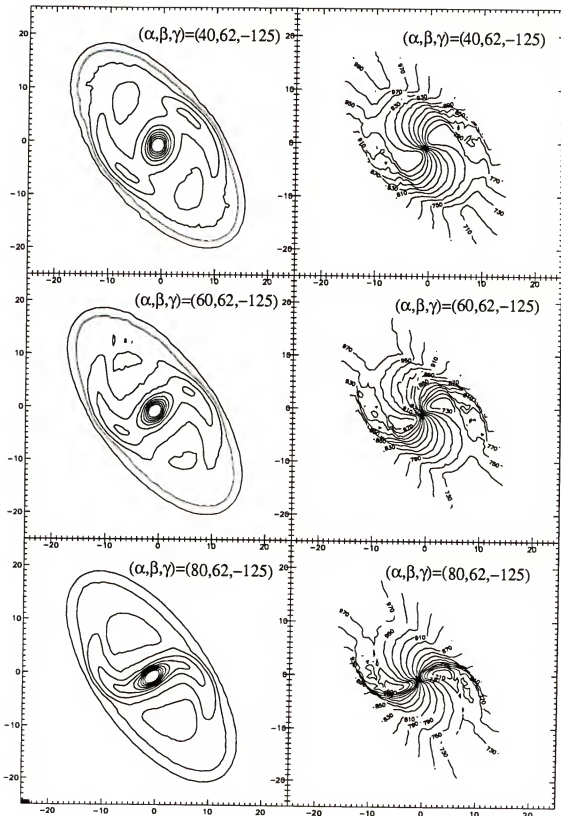


Figure 4.4: Unweighted, projected density and velocity fields for the model with shape parameters  $(q_a, q_b, q_c, \Omega) = (0.95, 0.92, 1.00, 1.00)$ . The surface density maps are on the left while the velocity maps are on the right. The projection parameters  $(\alpha, \beta, \gamma)$  are listed at the top of each figure.

not observed in HI; however, note that proper weights for the orbits have not yet been determined. This problem does not persist once the coefficients of the orbit weighting function have been determined from a least squares fit to the observed integrated-intensity of HI. Also, in the unweighted maps, there is a high concentration of orbits in the inner regions with low line of sight velocities. This tends to lower the average value of the line of sight velocity in pixels near the map center thereby producing the low velocity "tongues" in the velocity contour maps. Even though the innermost velocity contours in the unweighted maps do not quantitatively match the observed contours, the set of projection parameters  $(\alpha, \beta, \gamma) = (40, 62, -125)$  appears to be the best choice to begin with. The primary reasons for this choice are as follows: first, the inner velocity tongues qualitatively resemble those in the observed velocity map; and second, the outer velocity contours at  $970 \text{ km s}^{-1}$ ,  $950 \text{ km s}^{-1}$  and  $930 \text{ km s}^{-1}$  closely resemble those in the observed velocity map.

For  $(\alpha, \beta, \gamma) = (40, 62, -125)$ , the coefficients of the weighting function for the orbits are computed and contour maps are constructed (see Figure 4.5). At first glance the weighted maps shown in Figure 4.5 appear to resemble the observations even less than the unweighted maps. However, the significant difference here is that the scale of the model is very important when pixel by pixel comparisons are made with the observations. One can rescale the model in order to fit particular features in the observed map by adjusting the rotation speed of the model. That a model with a higher rotation speed is needed for NGC 2685 can be seen by comparison of the velocity maps in Figure 4.5 (c) and 4.5 (d). The curves of Figure 4.2 show that a higher tumble rate will serve to decrease the radius at which the SAOs join the equatorial plane, thus making it easier to match the density enhancement along the outer edge of the inner component of the observed HI (see Figure 4.5 (a)).

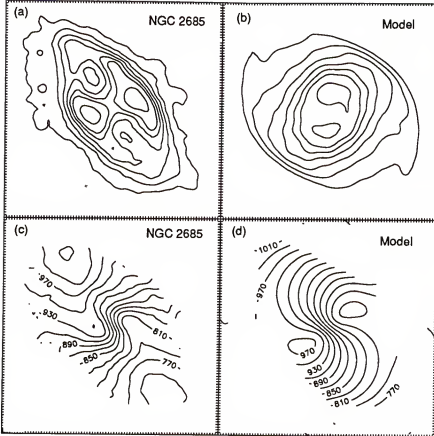


Figure 4.5: Comparison of the observations and the first weighted model of NGC 2685. For this model  $(q_a, q_b, q_c, \Omega) = (0.95, 0.92, 1.00, 1.00)$  and  $(\alpha, \beta, \gamma) = (40, 62, -125)$ . The observed surface density is given in (a), while the surface density from weighted orbits in this model is in (b). The corresponding velocity fields are given in (c) and (d).

Figure 4.6 (a) shows a selected sample of projected orbits for this model. The projected axes of the triaxial gravitational potential are also shown. In Figure 4.6 (b) only those portions of the orbits in front of the galaxy, above the plane of the sky towards the observer, are shown. Compare this diagram with the optical photograph of NGC 2685 in order to see how this model can account for the peculiar dust lanes crossing the body of the galaxy.

The results obtained from a model with  $(q_a, q_b, q_c, \Omega) = (0.95, 0.92, 1.00, 2.00)$  and  $(\alpha, \beta, \gamma) = (40, 62, -125)$  are shown in Figure 4.7. The model maps are quite remarkable in the sense that they quantitatively reproduce the observed velocity map.

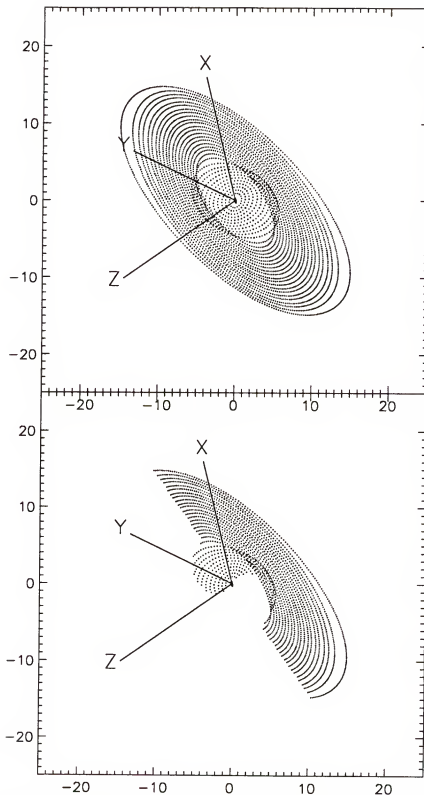


Figure 4.6: A selected set of projected orbits produced from the model with  $(q_a, q_b, q_c, \Omega) = (0.95, 0.92, 1.00, 2.00)$  and projection parameters  $(\alpha, \beta, \gamma) = (40, 62, -125)$

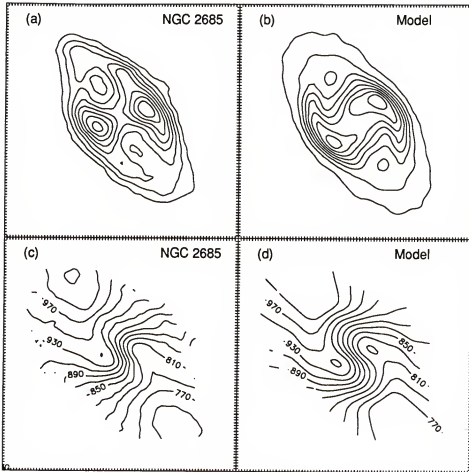


Figure 4.7: Comparison of the observations and the weighted model of NGC 2685. For this model  $(q_a, q_b, q_c, \Omega) = (0.95, 0.92, 1.00, 2.00)$  and  $(\alpha, \beta, \gamma) = (40, 62, -125)$ . The observed surface density is given in (a), while the surface density from weighted orbits in this model is in (b). The corresponding velocity fields are given in (c) and (d). Note the excellent agreement between the velocity contours of (c) and (d).

Synthetic channel maps constructed from this model are shown in Figure 4.8. These maps can be compared to the observed channel maps in Figure 3.2. The weighting function for this solution is of fifth order, and is plotted as a function of  $H$  in Figure 4.9 (a). Figure 4.9 (b) plots the maximum radial extent of each orbit as a function of  $H$ . Table 4.1 gives the values of the coefficients for the polynomial in  $H$  obtained from the least squares solution and their errors. The value of  $H$  used to compute the

weighting function is actually a normalized value, where  $H' = H/H_{min}$  and  $H_{min}$  is the minimum value of  $H$  for the ensemble. Therefore, the weighting function is actually a polynomial in  $H'$ .

However, for the plot of Figure 4.9, the weighting function is computed as a function of  $H'$  and then actual values of  $H$  are printed on the axis instead of the normalized values.

One way that the goodness of fit can be assessed is through calculation of the merit function, or maximum likelihood estimate of the model parameters, called “chi-square”. Given a value for the standard deviation of the measurement errors  $\sigma$  and letting  $y_i^o$  represent each observed data point and  $y_i^m$  each data point computed from the model, then

$$\chi^2 = \sum_{i=1}^N \left( \frac{y_i^o - y_i^m}{\sigma} \right)^2, \quad (4.13)$$

where  $N$  is the number of equations (see Press et al., 1986, Chapter 14). If the number of degrees of freedom  $\nu$  is given by  $\nu = N - M$ , where  $M$  is the number of independent variables, then a moderately good fit should give  $\chi^2 \approx \nu$ . Given an estimate for  $\sigma$  in the integrated intensity map of 106 mJy/Beam  $\times$  km s $^{-1}$ , the fit obtained for the model of NGC 2685 shown in Figure 4.7 gives  $\chi^2 = 4574$  for  $\nu = 6555$ . The true value of  $\sigma$  is difficult to ascertain due to the way the integrated intensity maps are constructed (see Chapter 3). The value used here is conservative and probably overestimates the noise in the integrated intensity map. However, the fact that the values for  $\chi^2$  and  $\nu$  are of the same order seems to indicate that the solution provides a reasonable fit to the data.

Synthetic channel maps constructed from the weighted models are shown in Figure 4.8. These maps should be compared to the observed channel maps in Figure 3.2; however, keep in mind that the observations were centered on a heliocentric velocity

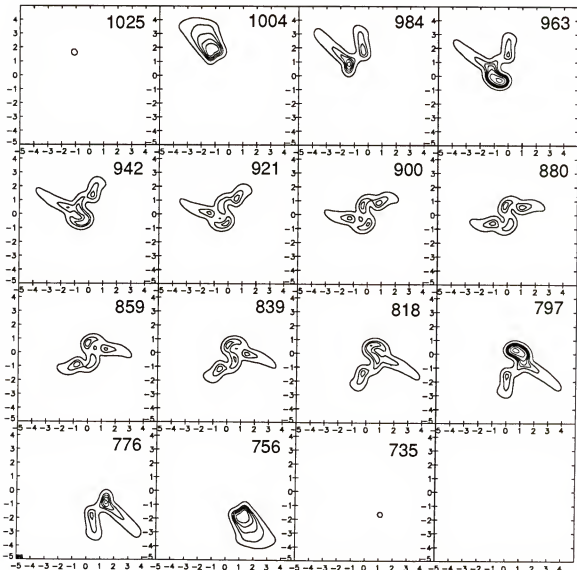


Figure 4.8: Model channel maps of NGC 2685 for  $(q_a, q_b, q_c, \Omega) = (0.95, 0.92, 1.00, 2.00)$  and  $(\alpha, \beta, \gamma) = (40, 62, -125)$ . The central velocity of the galaxy in these maps is given as  $880 \text{ km s}^{-1}$ .

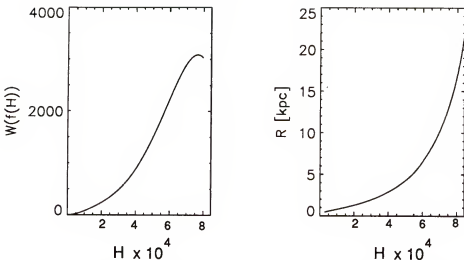


Figure 4.9: (a) Polynomial weighting function for the orbits from which the model in Figure 4.7 (b) and 4.7 (d) is obtained. This function is positive over the entire range of  $H$  for this model. (b) The maximum radial extent of each orbit as a function of  $H$  for this model.

Table 4.1: Coefficients and errors for the polynomial weighting function  $w(f(H'))$  shown in Figure 4.9, where  $H' = H/H_{min}$ .

Coefficient	Numerical Value	Error (+/-)
$a_0$	+0.83998	0.996727
$a_1$	+1.36944	0.991275
$a_2$	+8.17954	0.601967
$a_3$	-0.877713	0.111971
$a_4$	+0.058827	0.006445
$a_5$	-0.0011782	0.000116

of  $870 \text{ km s}^{-1}$ , while the systemic velocity of the gas appears to be about  $880 \text{ km s}^{-1}$ . Hence, the central velocity for each of the model channel maps is about  $10 \text{ km s}^{-1}$  less than in the observed channel maps. In the model channel maps, just as in the observed channel maps, emission from the outer ring first appears near  $1025 \text{ km s}^{-1}$ . However, while weak emission from the inner component is present in the observed channel map centered on  $1015 \text{ km s}^{-1}$ , its presence is not obvious in the model channel maps until  $984 \text{ km s}^{-1}$ . Despite this particular discrepancy the general structure of the model emission

regions over the entire velocity range of the channel maps is very similar to that seen in the observed channel maps of NGC 2685. There are some differences in the relative intensity levels of the channel maps, but these differences are not surprising if one considers that the weighting function is arbitrarily assumed to have a polynomial form, a necessary assumption if the problem is to be computationally tractable. Though there is no theoretical or physical basis for this assumption, such an assumption makes it possible to observationally constrain the model in a consistent and well defined manner. That this very simple model works so well suggests that more detailed modeling with more complicated, but realistic, potential forms may be in order.

If the underlying premise of this study holds true, that gas clouds in the rings of NGC 2685 are following streamlines defined by noncrossing prograde orbits in a rotating triaxial potential, then this model indicates that the overall distribution of matter in this galaxy is both mildly triaxial and slowly rotating. In order to obtain similar results for model potentials more prolate than this one, the rotation speed would have to be higher (see Figure 4.2). On the other hand a more spherical gravitational potential would require a lower rotation rate. Therefore, if the gravitational potential of this galaxy is constrained to rotate slowly, the shape of the triaxial potential must be nearly spherical if one wishes to successfully model the observed distribution of velocity of HI in terms of orbits.

#### Models of NGC 660

Here, following the same procedure described for NGC 2685, models for NGC 660 are constructed. First a linear scale is determined for the maps. The corrected recessional velocity of NGC 660 is  $982 \text{ km s}^{-1}$ , corresponding to a distance of 13 Mpc. This gives a linear scale of 0.38 kpc over 6", the width of a single cell on the VLA map. Thus, the

maximum radial extent of the inner and outer HI rings is 6.9 and 24.8 kpc, respectively. Consider the models of Figure 4.2. The maximum radial extent above the equatorial plane for the SAOs in the model with  $(q_a, q_b, q_c) = (0.95, 0.92, 1.00)$  and  $\Omega = 1.0$  is very close to the maximum radial extent of the HI observed in the inner ring (or disk). Therefore, this model seems to be the most reasonable choice for NGC 660.

Given the set of initial conditions corresponding to the model for which  $(q_a, q_b, q_c) = (0.95, 0.92, 1.00)$  and  $\Omega = 1.0$ , the next step is to determine a good set of projection parameters. The HI observations indicate a position angle for the outer ring of  $-7^\circ$ , measured from North in the direction East, while Table 3.9 gives an inclination for the stellar disk of the galaxy of  $63^\circ$ . If the outermost ring of HI is elliptical and lies near the equatorial plane of the potential then the only unknown angle is the angle that gives the orientation of the intermediate axis of the potential with respect to the observer. Thus, adopting the values of  $63^\circ$  and  $97^\circ$  for  $\beta$  and  $\gamma$ , a set of unweighted projected density and velocity maps is produced for three values of  $\alpha$ :  $20^\circ$ ,  $40^\circ$ , and  $60^\circ$ . Figure 4.10 shows the resulting projected density and velocity fields.

From comparison of the density and velocity contours in Figure 4.10 and Figure 4.4 to the integrated-intensity and intensity-weighted velocity maps of NGC 660, a good first approximation for the projection parameters in the weighted model of NGC 660 was determined to be  $(\alpha, \beta, \gamma) = (70^\circ, 63^\circ, 97^\circ)$ . The density and velocity fields that result from this choice of parameters are given in Figure 4.11 (b) and 4.11 (d).

From the appearance of the density map of Figure 4.11 (b), it is evident that the value for  $\alpha$  is not high enough. In order to determine a better choice of projection parameters, another series of unweighted surface density and velocity maps is produced for higher values of both  $\alpha$  and  $\beta$ . Thus, from these maps a new set of projection parameters,  $(\alpha, \beta, \gamma) = (100^\circ, 70^\circ, 97^\circ)$ , is selected and the orbit weights are determined. The

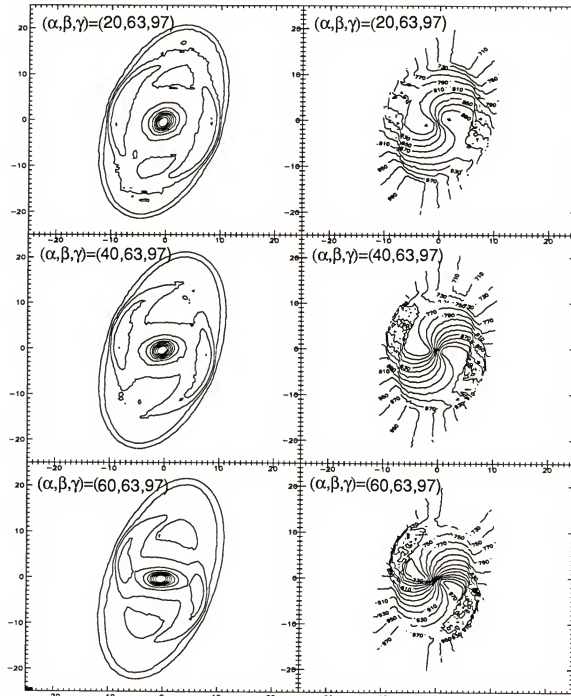


Figure 4.10: Unweighted, projected density and velocity fields for the model with shape parameters  $(q_a, q_b, q_c) = (0.95, 0.92, 1.00)$  and  $\Omega = 1.0$ . The surface density maps are on the left while the velocity maps are on the right. The projection parameters  $(\alpha, \beta, \gamma)$  are listed at the top of each figure, with  $\alpha$  increasing by  $20^\circ$  with each set.

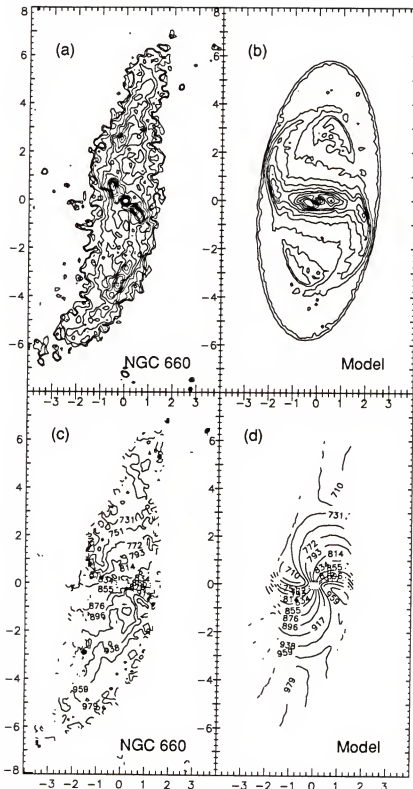


Figure 4.11: Comparison of the observations and the first weighted model of NGC 660. For this model  $(q_a, q_b, q_c, \Omega) = (0.95, 0.92, 1.00, 1.00)$  and  $(\alpha, \beta, \gamma) = (70, 63, 97)$ . The observed surface density is given in (a), while the surface density from weighted orbits in this model is in (b). The corresponding velocity fields are given in (c) and (d).

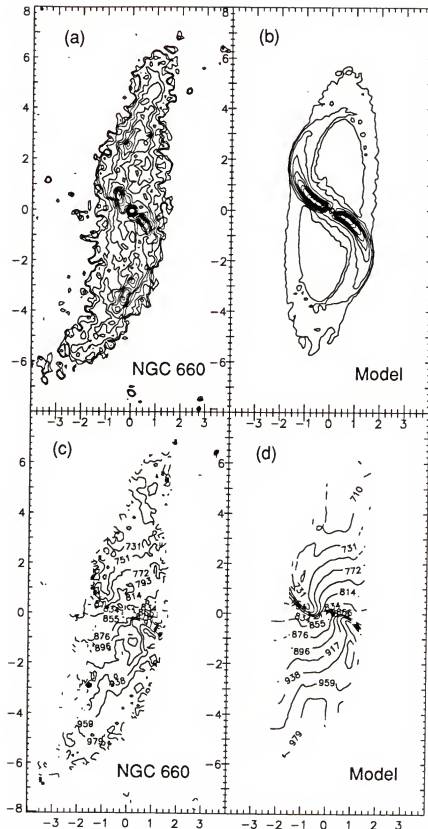


Figure 4.12: Comparison of the observations of NGC 660 and the model for which  $(q_a, q_b, q_c, \Omega) = (0.95, 0.92, 1.00, 1.00)$  and  $(\alpha, \beta, \gamma) = (100, 70, 97)$ . The observed surface density is given in (a), while the surface density from weighted orbits in this model is in (b). The corresponding velocity fields are given in (c) and (d).

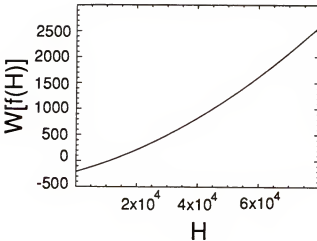


Figure 4.13: Weighting function for the orbits from which the model in Figure 4.12 (b) and 4.12 (d) is obtained. This function is positive over range of interest in  $H$  for this model.

Table 4.2: Coefficients and errors for the polynomial weighting function  $w(f(H'))$  of Figure 4.13, where  $H' = H/H_{\min}$ .

Coefficient	Numerical Value	Error (+/-)
$a_0$	-206.662	35.7866
$a_1$	+ 46.3119	21.1221
$a_2$	+ 1.80267	0.06230

weighted density and velocity fields derived from this model are shown in Figure 4.12 (b) and 4.12 (d), and the weighting function for the orbits is plotted in Figure 4.13. Due to the presence of blanked pixels in the center of the map where absorption is detected, the weighting function gives negative weight to most of the orbits inside the 1 kpc core radius. However, over the values of  $H$  that are of interest regarding the observed density and velocity fields, the solution is positive.

Table 4.2 gives the values and errors for the coefficients of the weighting function of Figure 4.13. For this solution, if the noise in the integrated intensity map is taken to be 265 mJy/Beam  $\times$  km s $^{-1}$  then  $\nu = 28,338$  and  $\chi^2 = 5185$ . The apparent discrepancy

of roughly a factor of five between these two values can be attributed to a conservative overestimate of the value for  $\sigma$  in the integrated intensity map of NGC 660. However, these values are in agreement to within an order of magnitude. Furthermore, the close resemblance of the model maps to the observed maps indicates that the fit is reasonable.

Figure 4.14 (a) shows a selected sample of projected orbits for a model with  $(q_a, q_b, q_c, \Omega) = (0.95, 0.92, 1.00, 2.00)$  and projection parameters  $(\alpha, \beta, \gamma) = (100^\circ, 70^\circ, 97^\circ)$ . Though this particular model rotates a little faster than the weighted model computed above for NGC 660, the shape parameters and projection angles are exactly the same; thus, the qualitative appearance of the orbits as seen in projection is the same as what would be expected from the model of Figure 4.12. The projected axes of the triaxial gravitational potential are also shown in Figure 4.14 (a) and (b). In Figure 4.14 (b) only those portions of the orbits in front of the galaxy (above the plane of the sky towards the observer), are shown. Note that the projection geometry of this model implies that the HI in the outermost ring lies in the equatorial plane of the potential with the gas clouds following trajectories defined by the  $E_p$ —a family of elliptical orbits. Furthermore, recall that the major axes of these orbits are aligned with the short axis of the gravitational potential. It is of interest to note that the geometry of this model implies that the central stellar component of the galaxy does not lie in the equatorial plane of the potential. Compare this diagram with the optical photograph of NGC 660 in order to see how this model can account for diagonal dust lane crossing the equatorial dust lane of the galaxy.

Figure 4.15 shows channel maps constructed from the model with  $(q_a, q_b, q_c, \Omega) = (0.95, 0.92, 1.00, 1.00)$  and  $(\alpha, \beta, \gamma) = (100, 70, 97)$ . The velocity printed on each map is the heliocentric line of sight velocity, with respect to the center of the galaxy. These model channel maps best represent the observations if the heliocentric systemic velocity

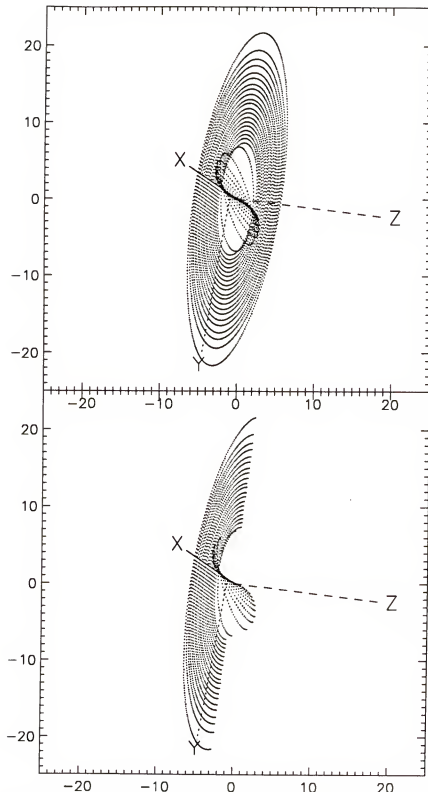


Figure 4.14: A selected set of projected orbits produced from a model with  $(q_a, q_b, q_c, \Omega) = (0.95, 0.92, 1.00, 2.00)$  and projection parameters  $(\alpha, \beta, \gamma) = (100^\circ, 70^\circ, 97^\circ)$

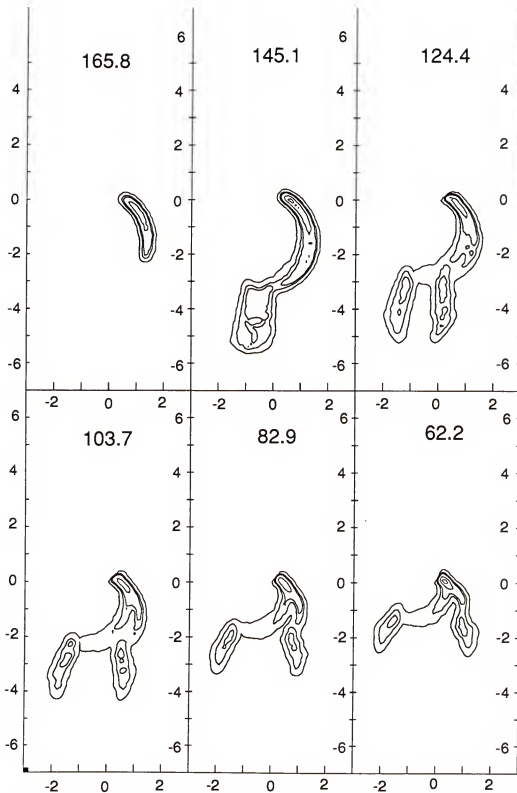


Figure 4.15: Synthetic channel maps constructed from the model with  $(q_a, q_b, q_c, \Omega) = (0.95, 0.92, 1.00, 1.00)$  and  $(\alpha, \beta, \gamma) = (100, 70, 97)$ .

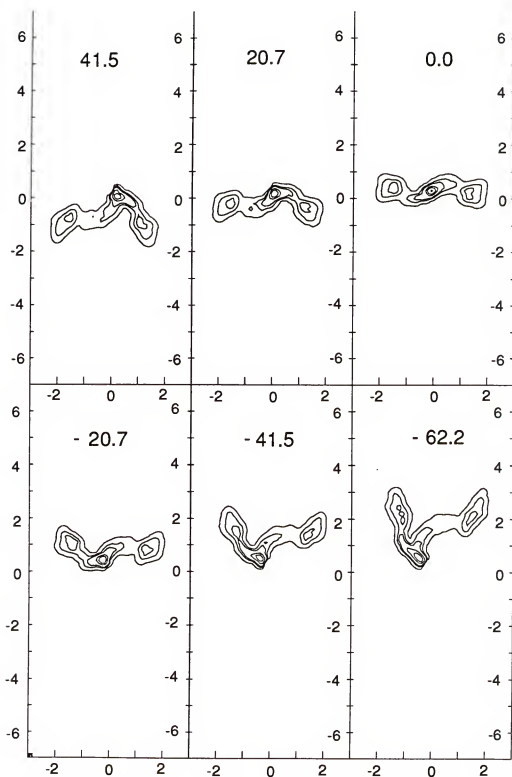


Figure 4.15: -- continued

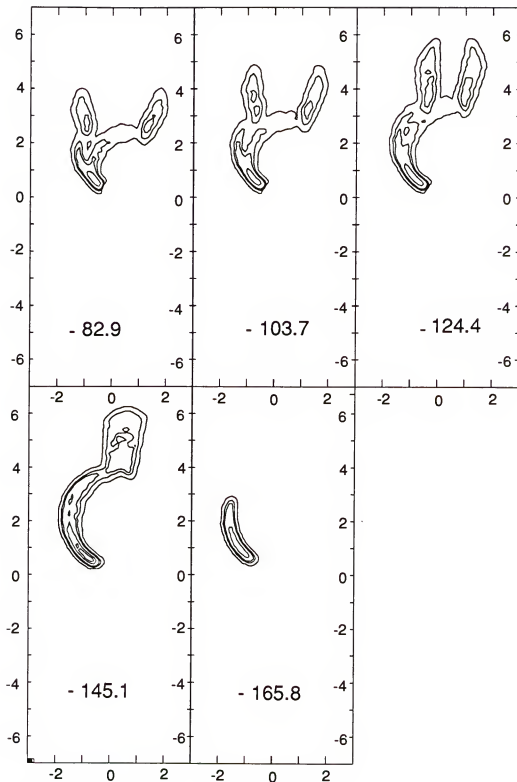


Figure 4.15: -- continued

of the gas is taken to be around  $865 \text{ km s}^{-1}$ , rather than  $842 \text{ km s}^{-1}$  as indicated by the kinematic fit to the line of nodes. The observed channel maps are given in Figure 3.21.

A comparison of the model maps to the observed maps reveals a difference in the appearance of the outermost contours. This may be due to an underestimate of the inclination angle for the model. Seen at a higher inclination, the outer "split wings" in the model maps would tend to blend together along the line of sight. In general, the channel maps capture the principal features of the observations; however, in the model maps, the contours are continuous between the inner and outer components, while in the observations there is a break in the contours. The maps in Figure 4.15 with velocities less than  $-82.9 \text{ km s}^{-1}$  are especially striking in that they capture the inner curvature of the contours in the observed maps of Figure 3.21 (n-r).

The maps constructed from the models discussed above indicate that the observed characteristics of the density and velocity field of HI in NGC 660 can be described quite well in terms of gas clouds occupying stable anomalous orbits if the gravitational potential of the galaxy is nearly spherical, but triaxial, and slowly rotating.

In conclusion, the models presented here for both NGC 2685 and NGC 660 show that the principal features of the observed surface density and velocity of neutral hydrogen gas can be reproduced from an appropriately weighted sample of orbits in a slowly rotating and nearly spherical, but triaxial potential. The fact that projected orbits from these simple models are able to account for the appearance of the peculiar dust lanes seen in optical photographs of these galaxies lends further credence to the basic underlying hypothesis of this research; i. e., clouds of neutral hydrogen in the rings of these galaxies follow trajectories that can be defined by an ensemble of stable, non-crossing orbits from both the inclined family of prograde anomalous orbits (SAO) and the prograde elliptical family of orbits ( $E_p-a$ ) in the equatorial plane of the potential.

## CHAPTER 5 CONCLUSION

The first topic of concern in this dissertation involves a study of inclined orbits in rotating triaxial gravitational potentials for which the long axis of the potential is taken to be the rotation axis. In particular, the main families of orbits in the bifurcation sequence containing the inclined family of prograde anomalous orbits are considered for potentials of two different shapes as a function of the rotation rate of the potential. In this final chapter these results are summarized and considered in the context of what they might imply about the dynamics of real galaxies that are long axis rotators, such as certain elliptical galaxies, or even some peculiar systems such as the polar ring systems NGC 660 and NGC 2685.

The second topic involves neutral hydrogen observations of the polar ring galaxies NGC 660 and NGC 2685 obtained with the Very Large Array Radio Telescope (VLA). Currently there is a tremendous amount of interest in the dynamics of these particular galaxies, primarily due to the fact that the inclined rings of these systems provide a natural probe of the gravitational potential outside the fundamental plane of their stellar disks. The rotation curves of normal spiral galaxies, including our galaxy, the Milky Way, unequivocally indicate the presence of a dark halo; however, galactic rotation curve data provide very little information about the overall shape of the dark halo. One way to probe the shape of a galaxy's gravitational potential is through modeling of the dynamics of stars and gas in orbits that are inclined to the plane of the stellar disk.

Observations of the inclined rings of the polar ring galaxies, especially spectral line observations like those presented here, can place powerful constraints on models of the gravitational potential of these systems. Aside from the models presented here, there are a number of theoretical models for polar ring galaxies present in the literature today that must be tested against these observations.

Over the last ten years or so, much work has been done regarding closed, stable periodic orbits in a tumbling triaxial potential (Binney, 1981; Heisler, Merritt and Schwarzschild, 1982; Magnenat, 1982; Martinet and Pfenniger, 1987; Martinet and de Zeeuw, 1988; and van Albada, Kotanyi, and Schwarzschild, 1982). Of the stable periodic orbit families that are closed in a coordinate frame rotating with the potential, the stable anomalous family has drawn particular attention, primarily due to the fact that these elliptical orbits are inclined relative to the equatorial plane of the tumbling potential. In general, studies of the stable anomalous orbits have focused on cases where the rotation, or tumble axis, is the short axis of the potential; however, this dissertation focuses on orbits in triaxial potentials that rotate about the long axis. To date, very little work has been done in this area, and the only complete studies of orbits in print, are for cases where the short axis of the potential is the rotation axis.

The principal results of this numerical study concern the form of the bifurcation sequence which contains the prograde anomalous family of orbits. This sequence is investigated as a function of the tumble rate of the potential. It is shown that, the main families of interest are the elliptical families in the equatorial plane ( $E_p$ ,  $E_p-a$ , and  $E_p-c$ ), the inclined family of prograde anomalous orbits (SAO and SAO-b), and the long axis family of radial orbits (z-axis family). The elliptical families  $E_p-a$  and  $E_p-c$  appear to correspond to the orbit families  $x_2$  and  $x_3$ , as discussed by Contopoulos and Grosbol (1988) in their study of planar bars; however, in the study presented here, these orbit

families are considered in terms of their connection, through the bifurcation sequence, to the inclined family of prograde anomalous orbits.

Above certain critical values of the rotation rate, collisions of bifurcations occur, marking the onset of changes in the bifurcation sequence. The value of  $\Omega$  at which these changes occur depends critically on the shape of the potential. From the study here, though limited to a few cases, it appears that the closer to spherical the potential is, the lower the critical values of  $\Omega$ .

For the case of a mildly triaxial potential with a finite core that is slowly rotating about its long axis, the main stable orbit families of interest are  $E_p$  (at small radii), the stable prograde anomalous orbits, and the family  $E_{p-a}$ . At small radii, the SAOs bifurcate from the family  $E_p$  in the plane. For larger radii, the inclination of the SAOs to the equatorial plane sharply increases to a maximum above the plane, and then decreases more gradually until the orbits terminate in the equatorial plane, at the bifurcation of a stable branch of the family  $E_{p-a}$ . Upon their bifurcation from  $E_p$ , orbits in the SAO family are elongated along the direction of the intermediate axis of the potential. This sense of elongation changes however, as the inclination of the orbits increases with larger radius, going through a circular orbit, and then becoming elongated in the direction of the short axis of the potential.

For the cases studied in detail, complex instability is present in the family of anomalous orbits; however, for low tumble rates, it does not manifest over a large enough energy range to be of much interest. For higher values of rotation, complex instability occurs over a much broader range of energy. Since the appearance of complex instability is associated with the onset of stochasticity in dynamical systems, a knowledge of where it occurs, as well as its extent, in both parameter and configuration space, is important for a broader understanding of long axis rotators. If orbits can be seen as providing the

underlying skeletal support of a galaxy, an understanding of the dynamics or orbits over a broad range of shapes and rotations is needed. Such information can perhaps help explain why certain types of configurations are more prevalent in nature than others, and also, why some configurations allow for gas to persist in a stable equilibrium configurations while others do not.

Also presented in this dissertation are high resolution neutral hydrogen observations of NGC 2685 and NGC 660 obtained with the Very Large Array Radio Telescope. These observations show that both NGC 2685 and NGC 660 contain a large amount of HI gas. Given assumed distances to the galaxies of 12.9 Mpc and 13.1 Mpc respectively, the amount of gas associated with NGC 2685 is  $1.5 \times 10^9$  solar masses, while that associated with NGC 660 is  $6.6 \times 10^9$  solar masses. Furthermore, dwarf satellite galaxies in the vicinity of these polar ring systems are present in the VLA maps. The maps show significant emission from MCG+10-13-030 and UGC 1195, corresponding to gas masses of  $3.6 \times 10^8 M_{\odot}$  and  $1.0 \times 10^9 M_{\odot}$ , respectively. In addition to these identified dwarf galaxies, there is a weak detection of signal from one, and perhaps two other galaxies in the HI maps of NGC 2685. The emission from these galaxies, which actually must be quite bright in the HI emission line, is severely attenuated by the response of the primary antenna beam at the distance of these galaxies from the pointing center of the observations. The weakest emission feature appears to be associated with the galaxy UGC 4683. The brighter emission feature cannot be identified with certainty to a particular galaxy until the redshifts of the optical candidates are known.

MCG+10-13-030 and UGC 1195 are very likely to be bound satellites, to NGC 2685 and NGC 660, respectively, though there are a number of unknown projection parameters that could alter this conclusion. From these observations, and  $H_0 = 75 \text{ km s}^{-1} \text{Mpc}^{-1}$ , a Keplerian mass of  $1.3 \times 10^{11} M_{\odot}$  is derived for NGC 2685, while a mass

of  $1.9 \times 10^{11} M_{\odot}$  is derived for NGC 660. The Keplerian mass derived for each of the dwarf galaxies MCG+10-13-030 and UGC 1195, which are assumed to be at the distance of NGC 2685 and NGC 660 respectively, is  $1.5 \times 10^{10} M_{\odot}$  and  $7.3 \times 10^9 M_{\odot}$ , respectively.

That NGC 2685 and NGC 660 exist in an environment where dwarf galaxies are present, seems to be consistent with the hypothesis that these galaxies obtained their gas by accretion, from or of, a dwarf galaxy. Though there is a possibility of capture of an intergalactic gas cloud, there is no observational evidence in support of the existence of such clouds at this epoch (Briggs, 1991).

The dynamical results presented in this dissertation are new and potentially important, not only for understanding stellar orbits in triaxial elliptical galaxies that exhibit evidence for slow rotation about the long axis of their mass distributions, but also for modeling the dynamics of the rings of particular polar ring galaxies, such as NGC 660 and NGC 2685. Models of the distribution and velocity of gas in these galaxies, in terms of a continuous sequence of stable prograde orbits in a rotating triaxial potential, appear to give reasonable results. The best results are obtained for nearly spherical configurations that rotate slowly about the long axis. Moreover, these results quantitatively reproduce the principal features of both the observed velocity field and the surface density of HI gas in these galaxies. This indication of a nearly spherical distribution of unseen matter is certainly not in conflict with the observational evidence and furthermore, some of the most successful models of normal spiral galaxies include a nearly spherical dark halo of about one disk mass. Furthermore, these models, which allow for stars and gas to move in the same prograde sense, are reasonable whether the rings of the galaxies formed primordially, or from some merger/accretion event.

Even though the orbit models of NGC 2685 and NGC 660 presented here are fairly successful at quantitatively reproducing the principal features of the observed HI surface density and velocity fields, it remains to be seen whether or not the orbit approach described here is a true representation of the underlying physics of these particular galaxies. Since the most recent observations of many polar ring galaxies (Whitmore et. al., 1990) show that there are significant differences in appearance between individual galaxies within the class itself, a simple model of the form considered here is perhaps not appropriate for all galaxies in the class. Recall that NGC 2685 and NGC 660 are a special subclass of the polar ring galaxies in that they exhibit two rings of stars and gas, one in a nearly polar orientation, and the other nearly in the plane of the stellar disk. If polar ring galaxies are the result of some sort of merger, as has been suggested by Toomre (1977) and others, then there are probably a number of different equilibrium forms, with and without net rotation, that the resulting potential could assume, forms which would depend explicitly on the details of an encounter. Thus, if polar ring galaxies constitute a class of post-merger systems, one would expect some differences in the underlying potential geometries and hence differences in the observed dynamics of inclined rings (or disks) of stars and gas in such systems.

Neutral hydrogen observations of polar ring galaxies, such as those presented here of NGC 2685 and NGC 660, can provide powerful constraints for models of the distribution of matter in these peculiar and rare systems. However, given a successful model of a polar ring system the question still remains open as to whether such results can be applied to more common types of galaxies. This question cannot be answered until the underlying physical and evolutionary processes that determine the structure of normal galaxies, such as spirals and ellipticals, are better understood. One approach towards

this understanding is through the study of orbit dynamics. Given that orbits provide the underlying skeletal support for non-axisymmetric stellar systems, then a study of orbits in such systems is crucial if one is to understand the various geometries observed for such systems. The introduction of slow rotation in non-axisymmetric systems serves to significantly modify the region of phase space occupied by orbits in the major families. Thus, an understanding of the behavior of the main orbit families, as a function of the axis and rate of rotation, may lead us to a broader understanding of the various structural geometries that are accessible to gravitating stellar systems. In particular, the work here applies to the case for triaxial potentials that rotate about the long axis. For the particular case of the polar ring galaxies NGC 660 and NGC 2685, it appears that the dynamics of the neutral hydrogen in these systems can be understood in terms of gas clouds following trajectories defined by stable, noncrossing prograde orbits in a nearly spherical, triaxial potential that tumbles slowly about its long axis. Therefore, it is hoped that the work described in this dissertation will ultimately lead us to a better understanding of the distribution of nonluminous matter around galaxies.

## BIBLIOGRAPHY

- Athanassoula, E. 1986, IN IAU Symp. 117, Dark Matter in the Universe, ed. J. Kormendy and G. R. Knapp (Dordrecht, Netherlands: Reidel), p. 133.
- Athanassoula, E. and Bosma, A. 1985, Ann. Rev. Astr. Ap., 23, 147.
- Athanassoula, E. and Sellwood, J. 1986, M. N. R. A. S., 221, 213.
- Avedisova, A. S. 1985, Sov. Astr. Lett., 11, 378.
- Bahcall, J. N. 1984a, Ap. J., 276, 156.
- Bahcall, J. N. 1984b, Ap. J., 276, 169.
- Bahcall, J. N. 1984c, Ap. J., 287, 926.
- Begeman, K. 1987, Ph. D. thesis, University of Groningen, Netherlands.
- Benvenuti, P., Capaccioli, M., and D'Odorico, S. 1976, Astr. Ap. 53, 141.
- Binney, J. 1978, M. N. R. A. S., 183, 779.
- Binney, J. 1981, M. N. R. A. S., 196, 455.
- Binney, J. and Tremaine, S. 1987, Galactic Dynamics (Princeton, N. J.: Princeton University Press), Chapter 3.
- Brand, J. 1986, Ph. D. dissertation, University of Leiden, Netherlands.
- Briggs, F. 1991 IN Warped Disks and Inclined Rings Around Galaxies, ed. S. Casertano, P. Sackett, and F. Briggs (Cambridge: Cambridge University Press), p. 1.
- Broucke, R. 1969, Am. Inst. Aeronaut. Astronaut. J. 7, 1003.
- Carignan, C. and Freeman, K. C. 1985, Ap. J., 294, 494.

- Christodoulou, D. M. 1990, IN Annals of the New York Academy of Sciences, Vol. 596, Galactic Models, ed. J. R. Buchler, S. T. Gottesman, and J. H. Hunter (New York: New York Academy of Sciences), p. 207.
- Clark, B. G. 1980, Astr. Ap., 89, 377.
- Clark, B. 1989, IN Synthesis Imaging in Radio Astronomy, ed. R. Perley, F. Schwab, and A. Bridle (Provo, Utah: Brigham Young University Print Services), Chapter 1.
- Condon, J. J. 1980, Ap. J., 242.
- Condon, J. J., Condon, M. A., Gisler, G., and Puschell, J. 1982, Ap. J., 252.
- Contopoulos, G. 1986a, Astr. Ap. 161, 244.
- Contopoulos, G. 1986b, Celest. Mech., 38, 1.
- Contopoulos, G. and Barbanis, B. 1985, Astr. Ap. 153, 44.
- Contopoulos, G. and Grosbol, P. 1988, Astr. Ap. 197, 83.
- Contopoulos, G. and Grosbol, P. 1989, Astr. Ap. Rev. 1, 261.
- Contopoulos, G. and Magnenat P. 1985, Celest. Mech., 37, 387.
- Contopoulos, G. and Papayannopoulos, T. 1980, Astr. Ap. 92, 33.
- Cornwell, T. and Braun R. 1989, IN Synthesis Imaging in Radio Astronomy, ed. R. Perley, F. Schwab, and A. Bridle (Provo: Brigham Young University Print Services), Chapter 8.
- Dekel, A. and Shlosman, I. 1983, IN IAU Symposium No. 100, Internal Kinematics and Dynamics of Galaxies, ed. E. Athanassoula (Dordrecht: Reidel), p. 187.
- de Vaucouleurs, G., de Vaucouleurs, A., and Corwin, H. 1976, Second Reference Catalogue of Bright Galaxies (Austin: University of Texas Press).
- de Zeeuw, P. T. and Merritt, D. 1983, Ap. J., 267, 571.

- Dixon, R. S. and Sonneborn, G. 1980, A Master List of Nonstellar Optical Astronomical Objects, (Columbus: Ohio State University Press), p. 334 & 336.
- Dobrovolskis, A. R. 1980, Icarus, 43, 222.
- Einasto, J., Kaasik, A., and Saar, E. 1974, Nature, 250, 309.
- Faber, S. M. and Gallagher, J. S. 1979, Ann. Rev. Astr. Ap., 17, 135.
- Freeman, K. C. 1970, Ap. J., 160, 811.
- Gagen-Torn, V. A., Popov, I. I., and Yakovleva, V. A. 1983, Astrofizika, 19, 599.
- Gilmore, G. F. 1989, IN The Milky Way as a Galaxy, ed. R. Buser and I. R. King (Mill Valley, California: University Science Books), Chapter 8.
- Goodman, J., Schwarzschild, M. 1981, Ap. J. 245, 1087.
- Gottesman, S. and Mahon, M. E. 1990, IN IAU Colloquium No. 124, Paired and Interacting Galaxies, ed. J. W. Sulentic and W. C. Keel (Washington, D. C.: NASA Conference Publication 3098), p. 209.
- Habe, A. and Ikeuchi, S. 1985, Ap. J. 289, 540.
- Habe, A. and Ikeuchi, S. 1988, Ap. J. 326, 84.
- Hadjidemetriou, J. D. 1975, Celest. Mech. 12, 255.
- Heggie, D. C. 1985, Celest. Mech. 35, 357.
- Heiligman, G. and Schwarzschild, M. 1979, Ap. J., 233, 872.
- Heisler, J., Merritt, D., and Schwarzschild, M. 1982, Ap. J., 258, 490.
- Hjellming, R. M. and Basart, J. P. 1982, IN An Introduction to the NRAO Very Large Array, April 1982 Edition, ed. R. M. Hjellming (Socorro, N. M.: National Radio Astronomy Observatory), p. 2-15.
- Hogbom, J. A. 1974, Astr. Ap. Suppl., 15, 417.

- Huchtmeier, W. K. and Richter, O.-G. 1989, A General Catalog of HI Observations of Galaxies, (New York: Springer-Verlag), p. 89.
- Hunter, C. and Toomre, A. 1969, Ap. J., 155, 747.
- Hunter, J. H., Ball, R., and Gottesman, S. T. 1984, M. N. R. A. S., 208, 1.
- Hunter, J. H. and Moore, E. M. 1992, Ap. J., submitted.
- Kalnajs, A. J. 1983, IN IAU Symposium No. 100, Internal Kinematics and Dynamics of Galaxies, ed. E. Athanassoula (Dordrecht, Netherlands: Reidel), p. 87.
- Kuijken, K. and Gilmore, G. 1989, M. N. R. A. S., 239, 651.
- Lewis, B. M. 1987, Ap. J. Suppl., 63, 515.
- Little, B. and Tremaine, S. 1987, Ap. J. 320, 493.
- Lynden-Bell, D. 1965, M. N. R. A. S., 129, 299.
- Magnenat, P. 1982, Astr. Ap., 108, 89.
- Martinet, L. and de Zeeuw, T. 1988, Astr. Ap., 206, 269.
- Martinet L. and Pfenniger, D. 1987, Astr. Ap., 173, 81.
- Merritt, D. and de Zeeuw, P. T. 1983, Ap. J. Lett., 267, 119.
- Mould, J. R., Balick, B., Bothun, G., and Aaronson, M. 1982, Ap. J. Lett., 260, 37.
- Nilson, P. 1973, Uppsala General Catalogue of Galaxies (Uppsala, Sweden: Uppsala Offset Center AB), pp. 35 & 377.
- Olszewski, E. W., Peterson, R. C., and Aaronson, M. 1986, Ap. J. Lett., 302, 45.
- Oort, J. 1932, Bull. Astron. Inst. Neth., 6, 249.
- Ostriker, J. P., Peebles, P. J. E., and Yahil, A. 1974, Ap. J. Lett., 193, 1.
- Patsis, P. A. and Zacharias, L. 1990, Astr. Ap. 227, 37.

- Peterson, R. C. 1985, Ap. J. 297, 309.
- Petrou, M. 1980, M. N. R. A. S., 191, 767.
- Pfenniger, D. 1985, Astr. Ap. 150, 112.
- Press, W. H., Flannery, B. P., Teukolsky, S. A., and Vetterling, W. T. 1986, Numerical Recipes, The Art of Scientific Computing, (Cambridge: Cambridge University Press), Chapters 14 & 15.
- Rogstad, D. H. and Shostak, G. S. 1972, Ap. J., 176, 315.
- Rots, A. 1988, A Short Guide for VLA Spectral Line Observers, Edition 7.0 (Socorro, N. M.: National Radio Astronomy Observatory).
- Rubin, V. C., Burstein, D., Ford, W. K., and Thonnard, N. 1985, Ap. J., 289, 81.
- Rubin, V. C., Ford, W. K., and Thonnard, N. 1980, Ap. J., 238, 471.
- Rubin, V. C., Ford, W. K., and Thonnard, N. 1982, Ap. J., 261, 439.
- Sackett, P. D. and Sparke, L. S. 1990, Ap. J., 361, 408.
- Schechter, P. L. and Gunn, J. E. 1978, A. J., 83, 1360.
- Schechter, P. L., Sancisi, R., van Woerden, H., and Lynds, C. R. 1984, M. N. R. A. S., 208, 111.
- Schweizer, F., Whitmore, B. C., and Rubin, V. C. 1983, A. J., 88, 909.
- Shane, W. 1980, Astr. Ap., 82, 314.
- Slipher, V. M. 1914, Lowell Obs. Bull., 62.
- Sparke, L. 1984, M. N. R. A. S., 211, 911.
- Sparke, L. 1986, M. N. R. A. S., 219, 657.
- Sparke, L. 1991, IN Warped Disks and Inclined Rings around Galaxies, ed. S. Casertano, P. Sackett, and F. Briggs (Cambridge: Cambridge University Press), p. 261.

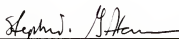
- Sparke, L. and Casterano, S. 1988, M. N. R. A. S., 234, 873.
- Sramek, R. and Schwab, F. 1989, IN Synthesis Imaging in Radio Astronomy, ed. R. Perley, F. Schwab, and A. Bridle (Provo, Utah: Brigham Young University Print Services), Chapter 6.
- Steiman-Cameron, T. Y. and Durisen, R. H. 1982, Ap. J. Lett. 263, 51.
- Steiman-Cameron, T. Y. and Durisen, R. H. 1984, A. J. 276, 101.
- Steiman-Cameron, T. Y. and Durisen, R. H. 1988, Ap. J. 325, 26.
- Steiman-Cameron, T. Y. and Durisen, R. H. 1990, Ap. J. 357, 62.
- Steiman-Cameron, T. Y., Kormendy, J. and Durisen, R. H. 1992, A. J., submitted.
- Thompson, R. 1989, IN Synthesis Imaging in Radio Astronomy, ed. R. Perley, F. Schwab, and A. Bridle (Provo, Utah: Brigham Young University Print Services), Chapter 2.
- Tohline, J. E. and Durisen, R. H. 1981, Los Alamos UR-81-2417.
- Tohline, J. E. and Durisen, R. H. 1982, Ap. J. 257, 94.
- Tohline, J. E., Simonson, G. F. and Caldwell, N. 1982, Ap. J. 252, 92.
- Toomre, A. 1977, IN The Evolution of Galaxies and Stellar Populations, Ed. B. M. Tinsley and R. B. Larsen, (New Haven, Conn.: Yale Univ. Obs.), p. 418.
- Tubbs, A. D. 1980, Ap. J. 214, 969.
- Tubbs, A. D. and Sanders, R. H. 1979, Ap. J. 230, 736.
- Tully, B. R. 1988, Nearby Galaxies Catalogue (Cambridge: Cambridge University Press)
- Ulrich, M. H. 1975, Astronomical Society of the Pacific 87, 965.
- van Albada, T. S., Bahcall, J. N., Begeman K., and Sancisi, R. 1985, Ap. J. 295, 305.

- van Albada, T. S., Kotanyi, C. G. and Schwarzschild, M. 1982, M. N. R. A. S., 198, 303.
- van Albada, T. S. and Sancisi, R. 1986, Phil. Trans. R. Soc. Lond., A320, 15.
- van Gorkom, J. 1992, presented at First Institute of Fundamental Theory Dark Matter Workshop, University of Florida, Gainesville.
- van Gorkom, J. H., Schechter, P. L., and Kristian, J. 1987, Ap. J. 314, 457.
- Wakamatsu, K. and Arp, H. C. 1983, Ap. J. 273, 167.
- Whitmore, B. C. 1984, A. J., 89, 618.
- Whitmore, B. C., Lucas, R. A., McElroy, D. B., Steiman-Cameron, T. Y., Sackett, P. D., and Olling, R. P. 1990, A. J., 100, 1489.
- Whitmore, B. C., McElroy, D. and Schweizer, F. 1987a, Ap. J. 314, 439.
- Whitmore, B. C., McElroy, D. and Schweizer, F. 1987b, IN IAU Symposium 127, Structure and Dynamics of Elliptical Galaxies, Ed. T. de Zeeuw (Dordrecht, Netherlands: Reidel), p. 413.
- Young, J. S., Xie, S., Kenney, J. D. P., and Rice, W. L. 1989, Ap. J. 70.

#### BIOGRAPHICAL SKETCH

Mary Elaine Mahon was born May 15, 1956, to Arthur Forrest and Mary Boley Camp, in Gainesville, Florida. She has two brothers, Samuel Forrest Camp and Arthur Thomas Camp. The first 12 years of her life were spent in Gainesville, Florida, followed by two years in Ormond Beach, Florida, and four years in Redington Beach, Florida. Following her graduation from Seminole High School in 1974, she spent two years in St. Petersburg Florida, two years in College Park, Georgia, and then moved back to her original home of Gainesville, Florida, where she now lives in equilibrium with her wonderful husband, John K. Mahon III, and five cats. After obtaining an A.A. degree from Santa Fe Community College in Gainesville, she began her study of astronomy at the University of Florida, obtaining her B. S. and M. S. degrees there. She looks forward to the night when she has finished writing her dissertation, and she and her one true love can lie in each other's arms beneath the stars and contemplate the vastness of space and the depth of their love.

I certify that I have read this study and that in my opinion it conforms to acceptable standards of scholarly presentation and is fully adequate, in scope and quality, as a dissertation for the degree of Doctor of Philosophy.



---

Stephen T. Gottesman, Chair  
Professor of Astronomy

I certify that I have read this study and that in my opinion it conforms to acceptable standards of scholarly presentation and is fully adequate, in scope and quality, as a dissertation for the degree of Doctor of Philosophy.



---

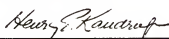
Neil Sullivan  
Professor of Physics

I certify that I have read this study and that in my opinion it conforms to acceptable standards of scholarly presentation and is fully adequate, in scope and quality, as a dissertation for the degree of Doctor of Philosophy.

---

George C. Contopoulos  
Graduate Research Professor of  
Astronomy

I certify that I have read this study and that in my opinion it conforms to acceptable standards of scholarly presentation and is fully adequate, in scope and quality, as a dissertation for the degree of Doctor of Philosophy.



---

Henry E. Kandrup  
Assistant Professor of Astronomy

I certify that I have read this study and that in my opinion it conforms to acceptable standards of scholarly presentation and is fully adequate, in scope and quality, as a dissertation for the degree of Doctor of Philosophy.

*James H. Hunter*  
\_\_\_\_\_  
James H. Hunter  
Professor of Astronomy

This dissertation was submitted to the Graduate Faculty of the Department of Astronomy in the College of Liberal Arts and Sciences, and to the Graduate School and was accepted as partial fulfillment of the requirements for the degree of Doctor of Philosophy.

May 1992

\_\_\_\_\_  
Dean, Graduate School